# Theoretical Study of the Electronic and Optical Properties of Low-dimensional Semiconductor Nanostructures with Complex Geometries

Yuanzhao Yao

March 2018

# Theoretical Study of the Electronic and Optical Properties of Low-dimensional Semiconductor Nanostructures with Complex Geometries

Yuanzhao Yao

Submitted to the Graduate School of
Pure and Applied Sciences
in Partial Fulfillment of the Requirements
for the Degree of Doctor of Philosophy in
Engineering

at the
University of Tsukuba

Graduate School of Pure and Applied Sciences

# Theoretical Study of the Electronic and Optical Properties of Low-dimensional Semiconductor Nanostructures with Complex Geometries

(複雑な形状の低次元半導体ナノ構造の電子的および光学的特性の理論的研究)

Yuanzhao Yao

Doctor of Philosophy in Engineering

## Abstract

### 1. Introduction

Semiconductor crystals of the nanometer size have been one of the most important research topics in electronics and solid state physics for decades [1, 2]. The conventional nanostructures such as quantum wells and quantum dots (QDs) have been systematically investigated and have played a central role in many practical applications including solar cells [3, 4], LEDs [5, 6], and medical imaging [7, 8]. The developing synthesis technologies have succeeded in fabricating new nanostructures with complex geometries [9, 10]. Because the shape of nanostructures has a critical influence on their electronic and optical properties, the investigations of new nanostructures with complex geometries are important for both fundamental and application research fields. Due to the nonuniformity of the size and shape of the nanostructures, the experimental spectroscopy of nanostructures always suffers from the large inhomogeneous broadening. Consequently, the feature of the electronic and excitonic structures may be hidden in the spectroscopy, and it is difficult to identify the optical transitions. To reveal the fundamental physics of the nanostructures, the theoretical investigation is necessary. With appropriate assumptions and approximations, the theoretical study can clarify the effect of individual influence factors, which is an obvious advantage over the experimental results including the influence from many factors simultaneously. Thus, the theoretical investigation is powerful to explain the experimental observation. Furthermore, the theoretical study can predict the electronic and optical properties of nanostructures, which is helpful for the future experimental studies.

Motivated by the experimental results of our collaborators, we studied the exciton states of nanostructures with complex geometries recently reported, that is, the tetrapod-shaped and coupled ring-shaped nanostructures as well as their response to external electric and magnetic fields. The calculation results showed a good agreement with the experimental observation and offered a prediction of the optical properties of these nanostructures. In addition, inspired by the recent study of the photonic crystal, we investigated the electronic structure of the periodically modulated quantum wells and predicted the formation of the Dirac cones at the Γ point of band structure.

### 2. Theoretical method

Because the nanostructures in the present thesis are in the strong confinement regime, the kinetic energy of the carriers is larger than the Coulomb energy among them. Thus, we first calculated the kinetic energy, and then took the contribution of Coulomb interaction into consideration. Because we were interested in the low energy states near the band edge, the single-band effective mass approximation was applied in our calculation. The time-independent Schrödinger equation was solved by analytical or numerical method according to the complexity of the nanostructure geometry. The nanostructures with complicated shapes cause difficulties in the

theoretical investigation by analytical methods and require reliable numerical studies. The finite element method is a flexible numerical method that offers an efficient approach to the complex geometries. In our calculation, the electron and hole wave functions were assumed as:

$$\psi_e(\mathbf{r}_e) = \varphi_e(\mathbf{r}_e)u_e(\mathbf{r}_e),$$
$$\psi_h(\mathbf{r}_h) = \varphi_h(\mathbf{r}_h)u_h(\mathbf{r}_h),$$

where $\varphi_e$ ($\varphi_h$) and $u_e$ ($u_h$) are the envelope function and atomic wave function of the electron (hole). The envelope functions and energy of single particle states were obtained by solving the single-band Schrödinger equation:

$$\mathcal{H}_{e,h}\varphi_{e,h}(\mathbf{r}_{e,h}) \equiv \left\{ -\frac{\hbar^2 \Delta_{e,h}}{2m^*_{e,h}} + V_{e,h}(\mathbf{r}_{e,h}) \right\} \varphi_{e,h}(\mathbf{r}_{e,h}) = E_{e,h}\varphi_{e,h}(\mathbf{r}_{e,h})$$

where $\Delta$ is the Laplace operator, $V$ is the confinement potential, and $E$ is the energy eigenvalue. By using the results of single particle states to form the pair state basis, the wave functions of the exciton states can be expanded with these bases.

$$\Psi(\mathbf{r}_e, \mathbf{r}_h) = \sum_{i,j} a_{ij}\varphi_e^{(i)}(\mathbf{r}_e)\varphi_h^{(j)}(\mathbf{r}_h)$$

The two-body Schrödinger equation for exciton states is:

$$\mathcal{H}_X\Psi(\mathbf{r}_e, \mathbf{r}_h) \equiv \left( \mathcal{H}_e + \mathcal{H}_h - \frac{e_0^2}{4\pi\varepsilon_0\varepsilon|\mathbf{r}_e - \mathbf{r}_h|} \right) \Psi(\mathbf{r}_e, \mathbf{r}_h) = E_X\Psi(\mathbf{r}_e, \mathbf{r}_h)$$

where $e_0$ is the elementary charge, $\varepsilon_0$ is the permittivity of free space, and $\varepsilon$ is the dielectric constant. The energy levels and wave functions of the exciton states were calculated with configuration interaction (CI) approach. By increasing the number of pair state basis in the exciton calculation, we carefully checked the convergence and ensure the sufficient accuracy of our calculation for the following quantitative discussion.

## 3. Results and discussion

### (1) Tetrapod-shaped nanostructures

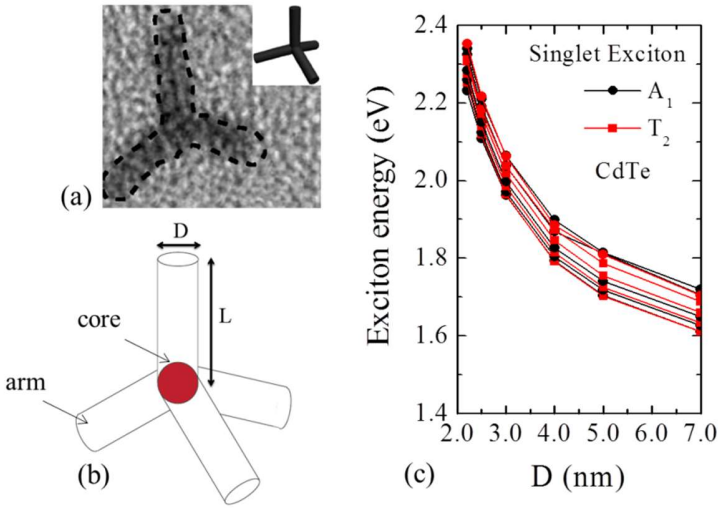


**Fig. 1: (a) TEM image of the tetrapod-shaped nanostructures (quantum tetrapods) [11]. (b) 3D model of quantum tetrapods used in our calculation. (c) The arm width (D) dependence of the spin-singlet exciton energy of quantum tetrapods made of CdTe.**

In the present thesis, firstly tetrapod-shaped nanostructures of various II-VI semiconductor materials were investigated. The tetrapod-shaped nanostructures consist of a central core and four branches at tetrahedral angles as shown in Fig. 1 (a) and (b) [9]. The central core has a zinc blende crystal structure and the branches have a wurzite crystal structure. Because of the strong confinement in the tetrapod-shaped nanostructures, their absorption spectra showed obvious quantum size effect, thus we can denote these nanostructures as "quantum tetrapod" hereafter [12]. Compared with the rapid progress of the experimental studies of quantum tetrapod, the systematic study of their exciton states is lacking. In our study, the spatial symmetry of wave functions for single particle states and electron-hole pair states were analyzed according to group theory. Our prediction of the wave function symmetry was confirmed by the numerical calculation. With CI calculation, we assigned the symmetry of exciton wave functions according to their main contributing pair state basis. As shown in Fig. 1 (c), for low energy excitons, their wave functions only have $A_1$ and $T_2$ symmetry. Because the lowest exciton state has $A_1$ symmetry, it has non-zero overlap integral between the wave functions of electron and hole. This indicated that the quantum tetrapods are optically active. The absorption spectra of quantum tetrapod were investigated with a wide range of parameters. The dominant influence of arm width on the absorption peak energy was revealed due to the strong confinement.

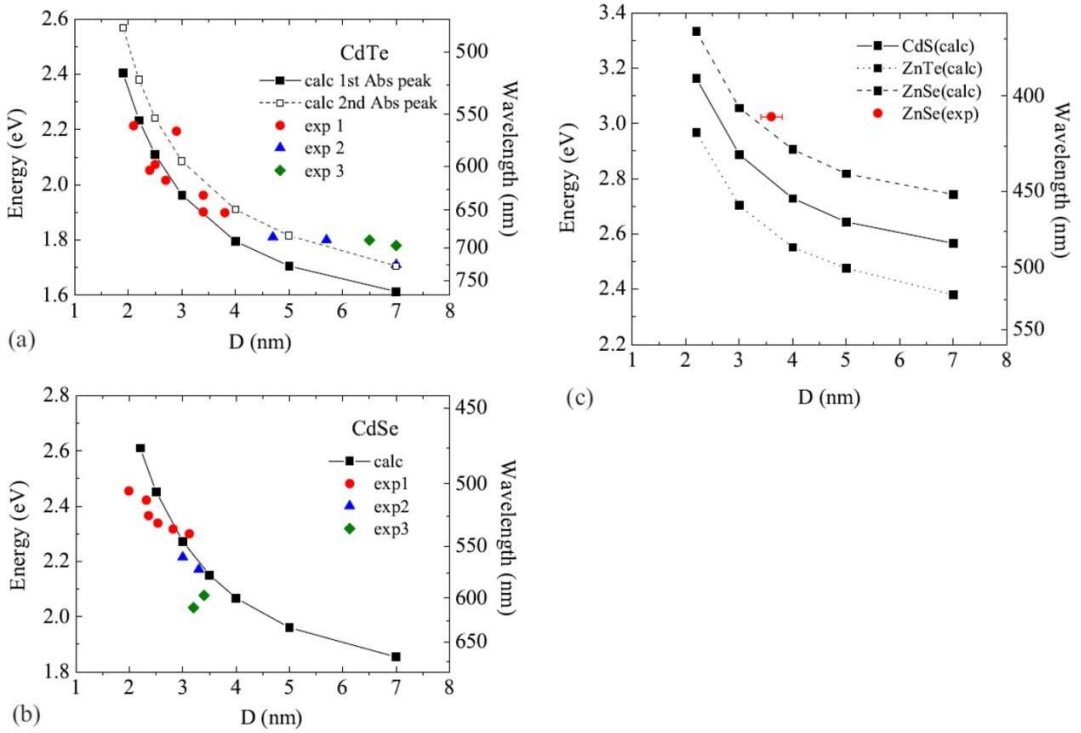


**Fig. 2: (a) The arm width (*D*) dependence of the peak energy of the lowest (black square) and second lowest (white square) absorption bands calculated for CdTe quantum tetrapods and the lowest absorption peak energy observed in Ref. [13] (exp1, circle), Ref. [14] (exp2, triangle), and Ref. [15] (exp3, diamond). (b) The peak energy of the lowest absorption band of CdSe quantum tetrapods: calculation (black square) and observation in Ref. [16] (exp1, circle), Ref. [17] (exp2, triangle), and Ref. [18] (exp3, diamond). (c) The lowest absorption peak energy calculated for CdS, ZnTe, and ZnSe quantum tetrapods (square) and observed for ZnSe (Ref. [19], circle).**

The comparison between calculation results and available experimental data showed a good agreement as

shown in Fig. 2. The absorption peaks observed in the experiment were assigned according to our prediction of the size effect of quantum tetrapods. The low energy peaks with small intensity were found which are difficult to be distinguished in the experiment results.

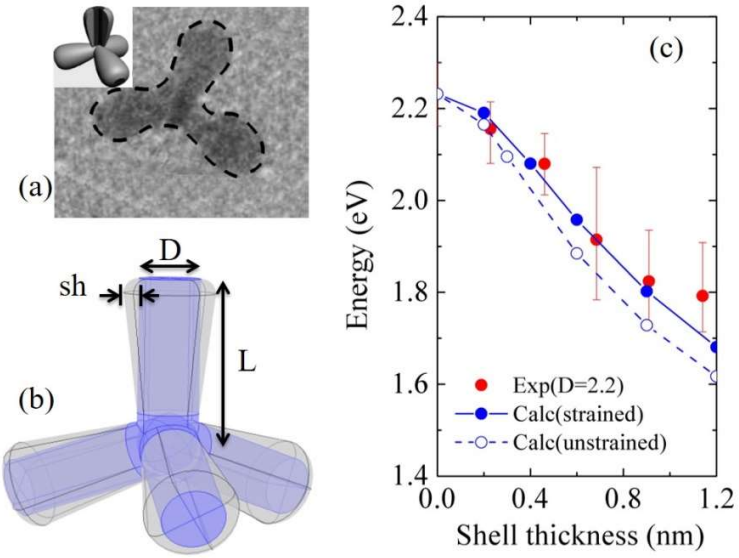


**Fig. 3: (a) TEM image of the tetrapod-shaped CdTe/CdS heterostructures (csTP) [11]. (b) 3D model of csTP used in our calculation. (c) Comparison of the calculated lowest spin-singlet exciton energy with the experimental photoluminescence peak energy of strained csTPs with arm width *D* = 2.2 nm. The experimental data are denoted by solid circles. The calculation results with and without strain effect were denoted by solid and dashed lines, respectively. The experimental results were shifted to align them with the calculated exciton energy at shell thickness *sh* = 0. The error bar indicates the full width at half maximum (FWHM) of the observed luminescence peak.**

The developing experimental investigations of quantum tetrapods succeeded in core-shell tetrapod-shaped heterostructures [20]. This new heterostructure has shells covering the lateral surface of the branches of the tetrapod as shown in Fig.3 (a) and (b). A tetrapod-shaped heterostructure composed of a CdTe tetrapod and CdS shells possess type-II band structure. The difference between the optical properties induced by the tetrahedral symmetry of tetrapod-shaped heterostructures and those of the well-studied type-II core-shell nanocrystals with spherical symmetry is interesting for fundamental investigation. So, we performed the first theoretical investigation of the influence of geometrical parameters and strain on the exciton states in branched heterostructure. We found that the strain promotes the type-II band structure. With increasing shell thickness, electrons and holes were confined in the non-adjacent regions of this heterostructure. Accordingly, more efficient charge separation is realized compared with type-II spherical core-shell QDs. The strain induced a small blue energy shift of the exciton ground state. As shown in Fig. 3 (c), when the strain effect was considered, the calculated shell thickness dependence of the lowest exciton energy showed a good agreement with that of the photoluminescence peaks observed in the experiment. The study of the core-shell tetrapod-shaped heterostructures with broken symmetry was also performed. We revealed that electrons and holes were confined in the same or different branches by manipulating the randomness, which is unique to branched core-shell heterostructures.

### (2) Ring-shaped nanostructures

Ring-shaped nanostructures offer a new platform to investigate the Aharonov-Bohm effect (A-B effect) using spectroscopic techniques. But the oscillation signature of the excitonic A-B effect in the single quantum rings is not significant in both experimental and theoretical results [21-24]. To clarify the reason for this weak excitonic A-B effect, we initially investigated the effect of magnetic field on the exciton state and trion state of a GaAs single quantum ring. By using the perturbation theory, the analytical solution of the single particle state was obtained, which showed a good agreement with numerical calculation results.

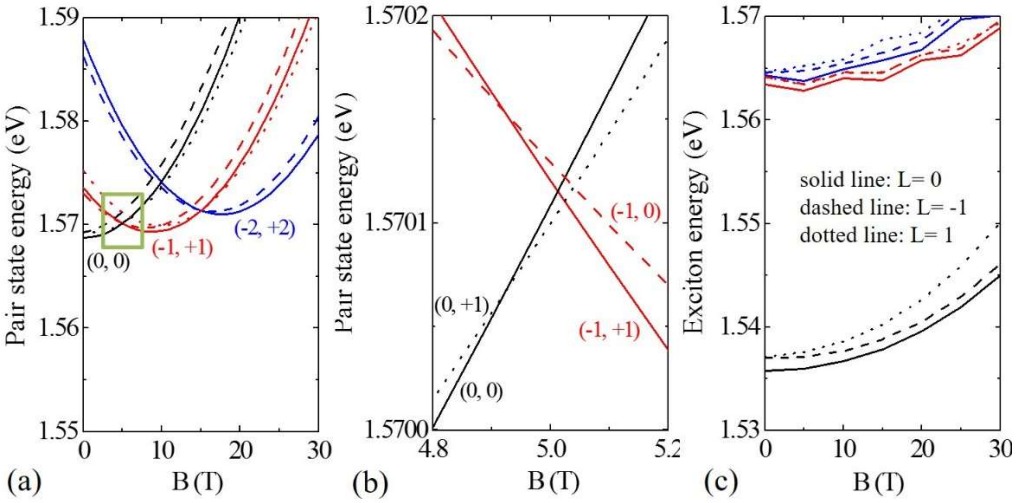


**Fig. 4: (a) Energy of the non-interacting pair states with total angular momentum L = 0, -1 and +1 as a function of the magnetic field for a 2D ring with average radius R= 12 nm and width W= 8 nm. The combination of the electron and hole angular quantum number ($l_e$; $l_h$) is denoted for the low-energy pair states with L = 0. (b) The magnified figure of the region in the green square in (a). (c) Exciton energy as a function of the magnetic field for L = 0, -1 and +1 in the same 2D ring. For both the pair states and the excitons, the states with L = 0, -1 and +1 are plotted with the solid lines, dashed lines, and dotted lines, respectively. For each L, the first, second and third lowest states are plotted in black, red and blue colors, respectively.**

The exciton states were calculated with the CI method. In the energy spectra of the electron-hole pair states without Coulomb interaction, the energy oscillation and total angular momentum transition can be found for the ground state as shown in Fig. 4 (a) and (b). When Coulomb interaction was taken into consideration, the energy oscillation feature of the lowest pair state disappeared as shown in Fig. 4 (c). The contribution of each pair state basis to the exciton ground state was analyzed. The vanishing excitonic A-B effect in the single quantum ring was ascribed to the Coulomb interaction which coupled the low-lying pair states with the same total angular momentum.

To avoid this situation and observe a clear A-B effect, we proposed the use of coupled nanostructures with applied electric field along the alignment direction of the components as shown in Fig. 5 (a) and (b). With this method, the Coulomb interaction can be reduced and a large difference in the average radii of the electron and hole trajectories can be realized at the same time. As shown in Fig. 5 (c) and (d), an obvious excitonic A-B effect was demonstrated in the QD-ring coupled nanostructures with moderate experimental conditions. We expect our proposal can be verified by the experimental observation of a sudden change of the emission spectra

intensity according to the total angular momentum transition in the excitonic A-B effect.

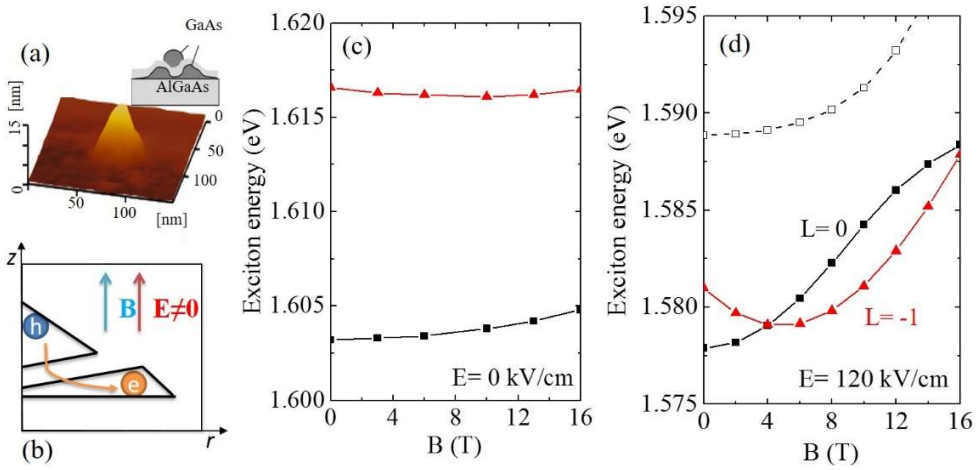


**Fig. 5: (a) AFM image of a QD-on-Ring nanostructure [25]. The inset is the schematic illustration of its cross section. (b) Illustration of the carrier separation in the QD-on-Ring nanostructure by applied electric field along the growth direction. The energy of lowest exciton states with the total angular momentum L = 0 and -1 in the QD-on-Ring nanostructure as a function of the magnetic field for the different applied electric field (c) E = 0, (d) E = 120 kV/cm. The exciton states with L = 0 and -1 are plotted with the solid squares and triangles, respectively.**

### (3) Periodically modulated quantum wells

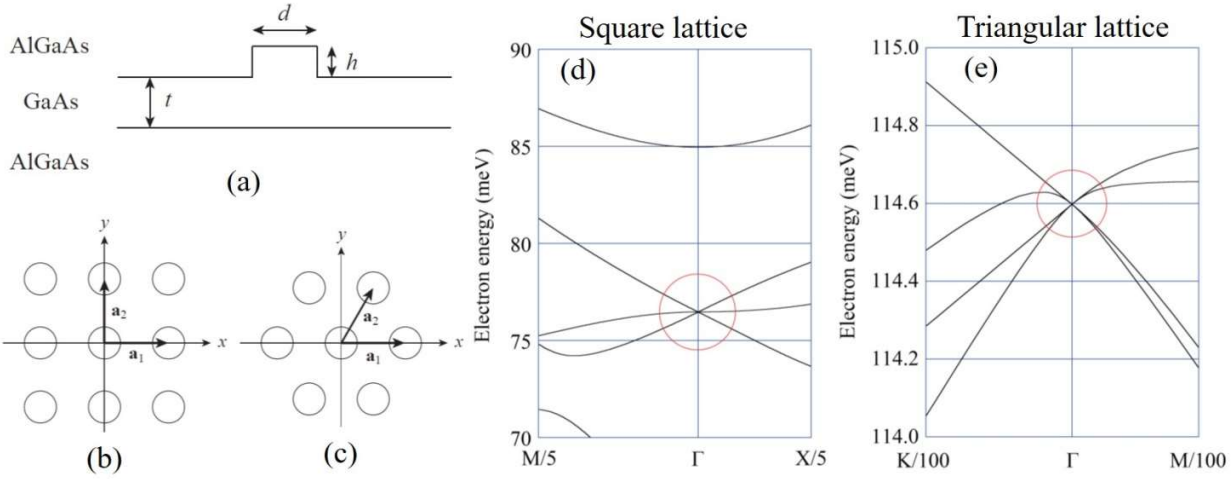


**Fig.6: (a) Side view of a periodically modulated quantum well composed of GaAs and AlGaAs layers with a cylindrical bump in each unit structure. Top view of the quantum wells with the (b) square and (c) triangular structural modulations. Energy bands of the periodically modulated GaAs/AlGaAs quantum wells with (d) square lattice (lattice constant a=30 nm, t =15 nm, h =6 nm, and d =22.8 nm), (e) triangular lattice (lattice constant a=30 nm, t=15 nm, h=6 nm, and d=20.55 nm). The vertical axis is the electron energy measured from the bottom of the GaAs conduction band. The horizontal axis is the wave vector in the two-dimensional Brillouin zone. X/5, for example, means that the horizontal axis is magnified by five times.**

The Dirac cones in the photonic crystal were characterized by their isotropic linear dispersion. Recent theoretical investigations revealed the nature of photonic Dirac cone formation [26-30]. The realization of accidental degeneracy of two modes requires the specific combination of the wave function symmetry of the involved modes. In addition to the photonic crystal, the Dirac cones can be expected for other wave systems according to the same rule of wave function symmetry. By using the k·p perturbation theory and the group theory, we judged the formation of Dirac cones in the vicinity of the Γ point for periodically modulated quantum wells whose illustration can be found in Fig. 6 (a). The necessary combinations of wave function symmetry were revealed for the modulated quantum wells with square lattice and triangular lattice. The prediction of Dirac cone formation in these two kinds of quantum wells was confirmed by numerical calculation with the finite element method as shown in Fig. 6 (d) and (e).

## 4. Conclusion

By using theoretical calculation, we investigated the exciton state, absorption and emission spectra of II-VI and III-V nanostructures with complex geometries. The effect of shape on their electronic and optical properties was revealed by combining the group theory and configuration interaction method. The quantum size effect of our calculation results showed a good agreement with the published experimental data, thus they can be used to explain the experimental observation. Moreover, our calculation predicted the electronic and optical properties of new nanostructures such as the excitonic A-B effect in the ring-shaped coupled nanostructure and the Dirac cones in the periodically modulated quantum wells. These results offer guidelines and reference information for the future experimental investigations.

**References**


[1] K. Barnham and D. Vvedensky ed., *Low-dimensional semiconductor structures: Fundamentals and Device applications*. (Cambridge University Press, 2001).

[2] Y. Masumoto and T. Takagahara ed., *Semiconductor quantum dots*. (Springer-Verlag, Berlin, 2002).

[3] B. Sun, E. Marx, and N. C. Greenham, *Nano Lett.* **3**, 961 (2003).

[4] L. Wang et al., *J. Phys. Chem. C* **111**, 9538 (2007).

[5] Z. Tan et al., *Nano Lett.* **7**, 3803 (2007).

[6] P. O. Anikeeva et al., *Nano Lett.* **9**, 2532 (2009).

[7] W. J. Parak et al., *Nanotechnology* **16**, R9 (2005).

[8] T. Pellegrino et al., *Small* **1**, 48 (2005).

[9] L. Manna et al., *J. Am. Chem. Soc.* **122**, 12700 (2000).

[10] S. Cheong et al., *J. Am. Chem. Soc.* **131**, 14590 (2009).

[11] D. N. Dirin et al., *Inorg. Mater.* **47**, 23 (2011).

[12] L. Manna et al., *Nature Mater.* **2**, 382 (2003).

[13] R. B. Vasiliev et al., *Mendeleev Commun.* **19**, 126 (2009).

[14] D. Tari et al., *Appl. Phys. Lett.* **87**, 224101 (2005).

[15] M. De Giorgi et al., *Microelectron. J.* **36**, 552 (2005).

[16] W. Y. Ko et al., *J. Mater. Chem.* **20**, 2474 (2010).

[17] Q. Pang et al., *Chem. Mater.* **17**, 5263 (2005).

[18] S. Asokan et al., *Small* **3**, 1164 (2007).

[19] H. Shen et al., *Dalton Trans.* **39**, 11432 (2010).

[20] R. B. Vasiliev et al., *Mendeleev Commun.* **19**, 128 (2009).

[21] J. Song, S. E. Ulloa, *Phys. Rev. B* **63**, 125302 (2001).

[22] H. Hu et al., *Phys. Rev. B* **63**, 195307 (2001).

[23] F. Ding et al., *Phys. Rev. B* **82**, 075309 (2010).

[24] B. Li, F. M. Peeters, *Phys. Rev. B* **83**, 115448 (2011).

[25] M. Elborg et al., *J. Crystal Growth* accepted (2017).

[26] K. Sakoda, H. Zhou, *Opt. Express* **18**, 27371 (2010).

[27] K. Sakoda, *Opt. Express* **20**, 3898 (2012).

[28] K. Sakoda, *Opt. Express* **20**, 9925 (2012).

[29] J. Mei et al., *Phys. Rev. B* **86**, 035141 (2012).

[30] K. Sakoda, *Opt. Express* **20**, 25181 (2012).

Table of Contents

# Chapter 1:

# Introduction

By the rapid progress in the fabrication technology, various semiconductor materials of the nanometer size have been reported, which will be denoted as nanostructure in the present thesis [1, 2]. For example, by the chemical synthesis methods, free-standing colloidal nanocrystals were reported [3–7]. On the other hand, the epitaxial synthesis methods succeeded in growing nanostructures on substrates [8, 9]. For example, by the droplet epitaxy method, strain-free systems can be realized for quantum wells, quantum dots and quantum rings [10]. The nanostructures attract the interests from both the experimental and theoretical investigations and have played an important role in many application fields including solar cells [11–13], LEDs [14,15], and medical imaging [16,17].

## 1.1 Low-dimensional nanostructures

The synthesized nanostructures usually have the nano-scale size in one, two or three dimensions, which correspond to the terminology of quantum well (QW), quantum wire (QWire) and quantum dots (QD). The limited size constricts the motion of electrons along certain dimensions, which is conventionally denoted as "confinement". And the semiconductor materials subject to the confinement are named low-dimensional semiconductors. Because the size of the nanostructure is comparable with the de Broglie wavelength of the electron, the wave feature of the electron becomes obvious, thus the novel effects on their electronic and optical properties can be expected according to the quantum mechanics.

When the motion of a free electron in the bulk material encounters the confinement along certain dimensions, the impenetrable boundary condition requires the wave function of the electron to behavior like a standing wave. The corresponding energy levels for the nanostructures are discrete. Compared with the bulk material, these low-dimensional semiconductors have a different density of states as shown in Fig. 1.1. Thus the significant changes in absorption and emission spectra occur because of the confinement as systematically explained in Refs. [19,20].

## 1.2 Symmetry of nanostructures

In addition to the different dimensions, the various shapes of nanostructures have a critical influence on their electronic and optical properties [4,21]. The symmetry of the nanostructure shape plays an important role for not only the degeneracy of the electronic states, but also the intensity of the optical spectra. Besides spherical-shape quantum dots, nanostructures with a lower symmetry have been reported recently, e.g., scroll-like nanoplatelets [22,23], tetrapod [24,25] and octapod-shaped nanocrystals [26,27].

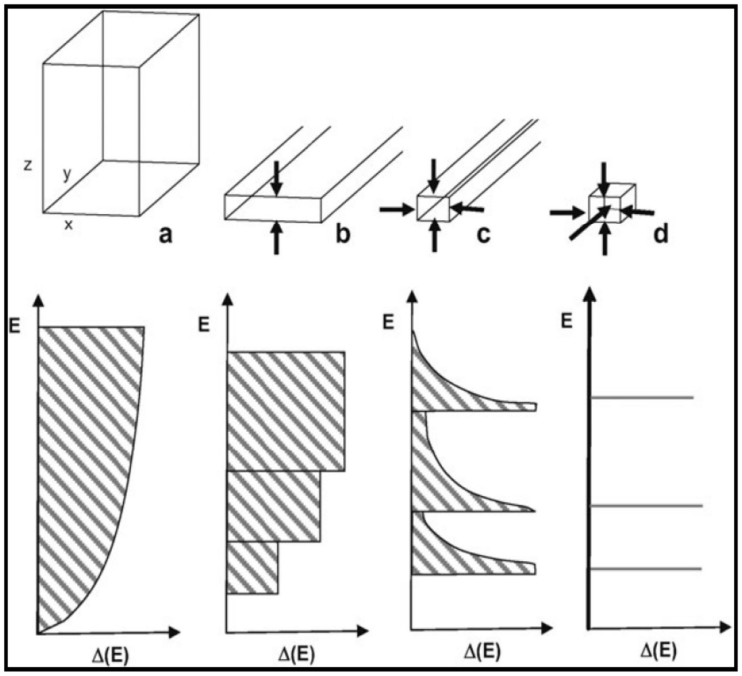


Figure 1.1: The schematic illustration of the confinement effect and the density of states (DOS) of various low-dimensional structures:(a)bulk material, (b)quantum well, (c)quantum wire and (d)quantum dot [18].

In fact, it is difficult to extract the nature of electronic structures and the features of optical properties only by experimental studies. In particular, the experimental measurement of nanostructures always suffers from the size distribution and shape randomness. So theoretical investigations are necessary. Motivated by the recent experimental results of our collaborators, we theoretically investigated the electronic and optical properties of the following representative nanostructure systems:

(a) Excitons of II-VI tetrapod-shaped nanostructure,

(b) Excitons of tetrapod-shaped core-shell heterostructure,

(c) Exciton complexes of ring-shaped and QD-Ring coupled nanostructures in the magnetic and electric fields,

(d) Electronic band structure of periodically modulated quantum wells.

## 1.3 Tetrapod-shaped nanostructures

Since the first report on their synthesis in 2000 [24], tetrapod-shaped nanocrystals of II-VI semiconductors have been attracting a great deal of attention due to their unique structure and the interest in the chemical process of their synthesis as shown in Fig 1.2. They consist of a central core and four arms connecting to the core part at tetrahedral angles.

Studies on tetrapods made of CdSe [24, 28–31], CdS [28, 32], CdTe [25, 28, 33–40], ZnTe [28, 41], ZnSe [42] have been reported. In addition to the synthesis and characteri-

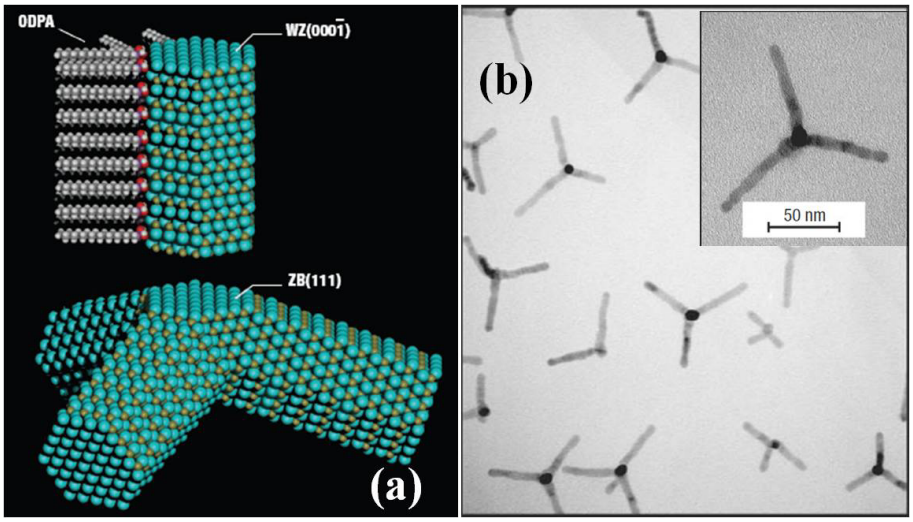


Figure 1.2: (a)Schematic model of a CdTe tetrapod. (b)TEM images of the tetrapods [25].

zation studies, applications to single-electron transistors [43] and photovoltaic cells were reported [11, 12, 44–46]. Because the energy levels of electron and hole in tetrapod-shaped nanocrystals are quantized due to the three-dimensional confinement of their wave functions, we call the tetrapod-shaped nanocrystals "quantum tetrapods" hereafter.

In their experimental studies, the specimens of quantum tetrapods not only suffer from their size distribution like other conventional nanocrystals, but also from their imperfect shapes. It is common that the geometric parameters of each arm are not the same in a single quantum tetrapod. Also the specimen of the quantum tetrapod is always mixed with bipod (with two arms) and tripod (with three arms). Consequently, their absorption and luminescence spectra possess peaks with a large broadening. It leads to difficulties in extracting the features of physics of the quantum tetrapods from the experimental results alone.

For the theoretical analysis of the electronic states of the quantum tetrapods, single-particle states were discussed by using a semiempirical pseudopotential method [47, 48] and the effective-mass approximation [34], while exciton states were investigated by the Hartree approximation [49–51] and the pseudopotential method [52]. On the other hand, we recently analyzed the exciton states of CdTe quantum tetrapods by numerical diagonalization of the configuration interaction Hamiltonian [53, 54]. This method is superior to the Hartree approximation, if sufficiently converged eigenvalues are obtained, because the latter does not take into consideration the full correlation energy.

In our systematic investigation, we revealed the influence of the tetrahedral symmetry of quantum tetrapods on their electronic and optical properties. We predicted the size dependence of the absorption peaks for quantum tetrapods of various II-VI materials. The comparison between calculation and available experimental data showed a good agreement. The detail of this investigation will be described in Chapter 3.

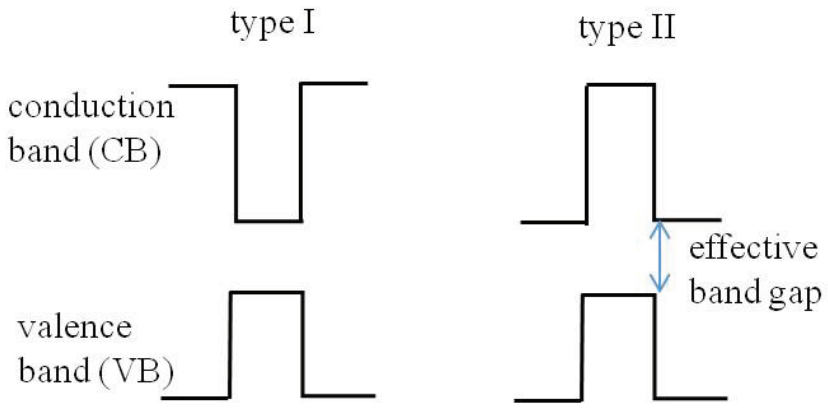


Figure 1.3: The illustration of the energy band alignment of type-I and type-II heterostructures.

## 1.4 Low-dimensional heterostructures

In addition to nanostructures composed of a single material, the continuous growth of different materials in one nanostructure leads to low-dimensional heterostructures [6]. Because of the different energy band structures of the component materials, the heterostructure can have a type-I or type-II band diagram as shown in Fig. 1.3. For the type-II heterostructures, the effective band gap is different from those for the component materials. Thus the heterostructure is a platform to manipulate the band gap and transition energy to fill the gap of the emission energy of pure semiconductor materials. The low-energy conduction band (CB) electron and the valence band (VB) hole are spatially separated in the type-II system. This leads to a long lifetime of the electron-hole pair due to the small recombination probability, which is desirable for the application to solar cells.

The investigations of the spherical-shape and rod-shape core-shell nanocrystals have been reported [55, 56]. In 2009, our collaborating group in the Material Department of the Lomonosov Moscow State University reported a systematic study of the core-shell tetrapod-shaped nanostructures [57], which is denoted as csTPs hereafter. The core-shell tetrapod consists of a quantum tetrapod and shells covering the lateral surface of the arms of the quantum tetrapod as shown in Fig. 1.4.

Compared with the quantum tetrapods, the study of the csTPs is more complicated. In accordance with the band alignment of their constituent materials, synthesized CdTe/CdS csTPs have the type-II band structure, that is, the electrons tend to be localized in the shells, which is isolated from the electrons in other arms. Meanwhile, the holes tend to be localized in the tetrapod part of the csTPs. As we mentioned, structural symmetry plays an important role regarding the nature of the carrier wave functions and also crucially influences the optical properties of the nanocrystals. The difference between the optical properties induced by the tetrahedral symmetry of the type-II csTPs and those of the well-studied type-II core-shell nanocrystals with a spherical symmetry is interesting for fundamental investigation.

On the other hand, the component materials of heterostructures usually have a non-

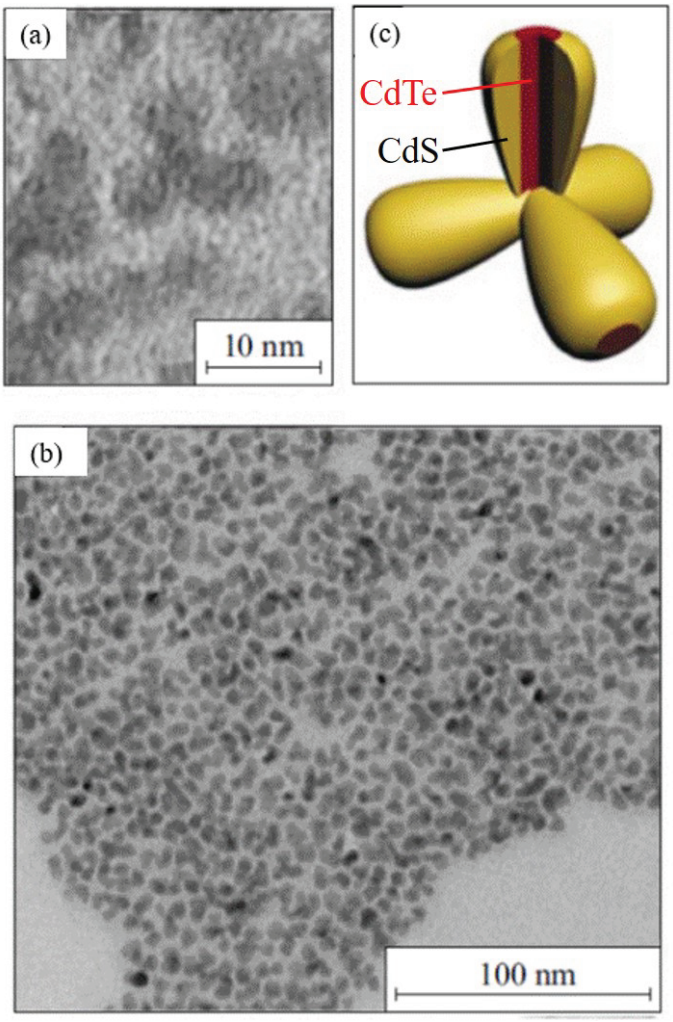


Figure 1.4: (a)(b) CdTe/CdSe tetrapod-shaped heterostructures based on CdTe tetrapods. (c) The illustration of the CdSe shell of tetrapod-shaped heterostructures covering the lateral surface of the arms of a CdTe tetrapod [7].

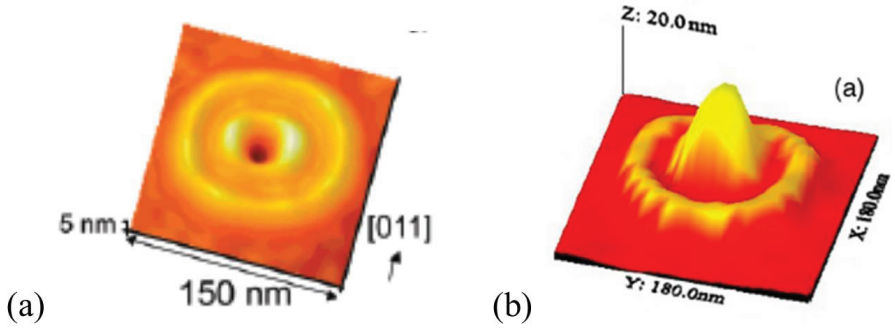


Figure 1.5: Atomic force microscopy (AFM) image of coupled nanostructures: (a) concentric quantum double rings and (b) a concentric quantum dot-ring nanostructure [63, 65].

negligible difference in their lattice constants. At the interface between the two materials, the arrangement of lattice point is modified at both sides (strain) to realize the continuous growth of the heterostructure. The strain in the heterostructure has a non-negligible influence on their energy band close to the interface [58]. For the csTPs consisting of a CdTe tetrapod and CdS arms, the large lattice mismatch between the constituent materials leads to non-negligible strain in the csTP. The strain strongly affects the band structure of the csTPs and is important to the investigation of the optical properties of the csTPs.

Our calculation results including the strain effect showed a better agreement with the experimental data than that without the strain effect. An efficient electron-hole separation was revealed in the csTPs compared with the type-II spherical core-shell nanocrystals. In addition to studying excitons in the csTPs with a perfect tetrahedral symmetry, we will also discuss the effect of the broken symmetry. The detailed discussion will be given in Chapter 4.

## 1.5 Ring-shaped nanostructure and coupled nanostructures

The ring-shaped nanostructures form an important sub-field of the nanostructure investigation. The central hole of the rings leads to the non-singly-connected structure, which is distinguished from the singly-connected structure, e.g., spherical QD. Consequently, the exploration of physical properties and applications of ring-shaped nanostructures attracted broad attention [59]. The ring-shape nanostructures can be fabricated by lithography [60] or droplet epitaxy method [61, 62]. The droplet epitaxy method leads to the possibility of growth of strain-free systems, e.g., the lattice-matched GaAs/AlGaAs nanostructures can be obtained, which is an advantage compared with conventional SK(Stranski-Krastanov) growth method. By the droplet epitaxy method, the geometry of the ring-shaped nanostructures can be controlled. Furthermore, coupled nanostructures can also be successfully fabricated. Thus, different kinds of ring-shaped nanostructures and coupled nanostructures were reported [63–65] as shown in Fig. 1.5.

Single quantum ring is the simplest ring-shaped nanostructure, but it offers a new platform to investigate the Aharonov Bohm (A-B) effect using spectroscopic techniques.

According to the simplest one-dimensional (1D) ring model [66], the kinetic energy of an electron in a 1D ring under the magnetic field ($\mathbf{B}$) piercing the ring interior is expressed as

$$E_l = \frac{\hbar^2}{2m^* R^2}\left(l + \frac{\phi}{\phi_0}\right)^2, \tag{1.1}$$

where $m^*$ is the effective mass, $R$ is the ring radius, $l = 0, \pm 1, \pm 2 \ldots$ is the angular momentum that specifies the electron motion, $\phi = \pi R^2 B$ is the magnetic flux, $\phi_0 = 2\pi\hbar/e$ is the flux quantum, and $e$ is the elementary charge. The spectral set $\{E_l(\phi)\}_{l=0,\pm 1,\ldots}$ becomes identical when $\Delta\phi = n\phi_0\,(n = 1, 2, \ldots)$, so it leads to a magneto oscillation in the energy spectrum with an oscillation period of $\phi_0$. A signature of the A-B oscillation was observed using the far-infrared capacitance spectroscopy for self-assembled quantum rings [67].

Similar spectral oscillation is expected to appear in the energy spectra of an exciton which consist of a CB electron and a VB hole bound by the Coulomb interaction. The ring size in this case must be smaller than the exciton Bohr radius, which means the Coulomb interaction is much smaller than the kinetic energies of the electrons and holes. Otherwise, the electron and hole are tightly bound and move together inside the ring, and the charge-neutral composite does not respond to the magnetic flux [68]. Thus, different trajectories for the electron and hole are necessary for the emergence of the excitonic A-B effect [69]. For this purpose, the non-uniform confinement of the electron and hole along the growth direction was utilized by applying an electric field perpendicular to the ring to make the average radius of their trajectories different from each other [70, 71]. However, the oscillation signature in both the experimental and the theoretical results of this case was not significant, probably because the Coulomb potential mixed different electron-hole pair states so that Eq. (1.1) did not hold any more.

We calculated the energy spectra of the exciton in a single quantum ring. The magnetic response does not show an obvious A-B oscillation. By analyzing the exciton wave functions, we revealed the reason for this vanishing excitonic A-B effect. On the other hand, our calculation of the trion state in the same single quantum ring showed energy oscillation for their ground state. Even when the Coulomb interaction is strong, the trion behaves like a noncharge-neutral composite and its motion is influenced by the magnetic field.

To overcome the issue of the vanishing A-B effect, we propose the use of coupled nanostructures to achieve a clear excitonic A-B effect. Among the reported ring-shaped coupled nanostructures [63–65, 72], we focus on the self-assembled quantum-dot (QD)-ring coupled structures, whose formation has recently been observed [72]. In Chapter 6, we will build a 3D model of the QD-ring coupled structure according to the experimental observation. Our calculation demonstrates that a clear excitonic A-B effect is obtained in these coupled nanostructures with the help of an external electric field.

As for the quantum double rings (QDRs) fabricated by Mano et al. [63] for the first time by the droplet epitaxy method, they have a smaller height and a larger lateral size than the single quantum rings fabricated in the same institute (NIMS). Micro photoluminescence (PL) spectra and electronic structures of GaAs QDRs covered with an AlGaAs

barrier layer were reported in Refs. [63] and [64]. Because the QDR has a nearly perfect circular symmetry, its electronic state can be characterized by the radial quantum number and the azimuthal quantum number. Some previous theoretical studies on the QDRs used this circular symmetry [73]. This property was also used for the theoretical study of its electronic states in a magnetic field perpendicular to the rings [74–76], which is relevant to the excitonic A-B effect [77]. Although the QDRs also attracted the interest of researchers for the A-B effect [78], we are interested in their large lateral sizes that can be used for frequency tuning.

The recent development of photonic crystal (PC) microcavities with large quality factors (Q) [79,80] has made it possible to observe interesting quantum optical phenomena such as the Purcell effect [81]. In the experiments reported so far, exciton emission of semiconductor QDs was used for this purpose, since the process of fabricating them has been fully established and is compatible with that of the PC microcavities. The ensemble of QDs shows a wide inhomogeneous distribution of exciton emission wavelengths due to their size distribution. This makes it difficult to tune their emission wavelength to the cavity resonance frequency when we try to observe photon emission from single dots to verify the Purcell effect. Most experiments have used temperature tuning of the exciton energy level, while others have used an excellent digital etching technique in addition to temperature tuning [82]. However, when the sample temperature is changed, not only the emission wavelength but also other important properties such as the dephasing time change. In addition, it takes a rather long time to reach a uniform temperature distribution after setting a new target temperature, which may be an experimental obstacle. Another quick and reliable tuning method is desirable. Recently we observed a relatively large Stark shift up to 4 meV for GaAs quantum double rings (QDRs) due to their large lateral sizes [83]. This indicated a possible method to tune the emission wavelength of QDRs to the cavity resonance frequency. For a better understanding of the experimental observation, the influence of the lateral electric field on the electronic structure of the QDRs was calculated. The results will be discussed in Chapter 5.

## 1.6 modulated QW nanostructures

Photonic crystals are regular arrays of materials with different refractive indices [84]. Photonic Dirac cones, or the Dirac cones with the linear dispersion relation of the electromagnetic eigen modes, can be realized on the $\Gamma$ point (Brillouin-zone center) by accidental degeneracy of two modes (See Fig. 1.6) [85–89] in the band structure of the photonic crystals. Mei et al. [87] discussed the formation of Dirac cones, Berry phase, and mapping into the Dirac Hamiltonian for phononic and photonic crystals by the $\mathbf{k} \cdot \mathbf{p}$ perturbation theory. Because the Dirac point in the Brillouin-zone center is equivalent to a zero effective refractive index [85], it has much potential for various applications like scatter-free waveguides [90] and lenses of arbitrary shapes [91].

The essence of the photonic Dirac-cone formation by accidental degeneracy of two modes is the particular combination of the spatial symmetry of their wave functions [87–89]. Its general proof for arbitrary periodic optical media was given by the $\mathbf{k}\cdot\mathbf{p}$ perturbation

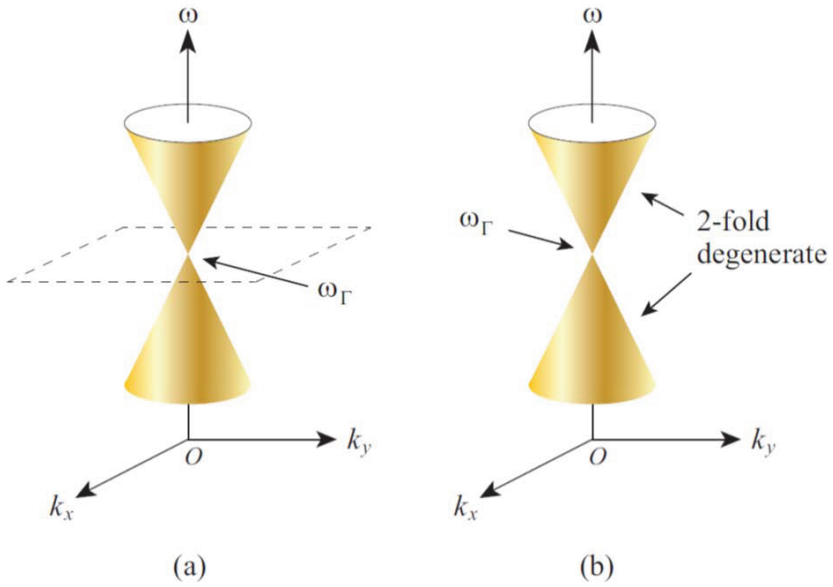


Figure 1.6: (a) Dirac cone (gold) with an auxiliary quadratic dispersion surface (dotted lines) and (b) double Dirac cone on the Γ point ($\mathbf{k} = 0$) of the two-dimensional Brillouin zone materialized by accidental degeneracy of two modes with particular combinations of mode symmetries. $\omega_\Gamma$ denotes the Dirac point.

theory combined with the group theory [87, 88]. Because the presence of the photonic Dirac cone on the Γ point is purely a consequence of particular combinations of mode symmetries, Dirac cones are expected to be realized not only in photonic structures but also in any wave systems including electron, phonon, and exciton systems. By introducing periodic structural modulation and/or applying periodic external potentials, we can realize subbands to the energy spectra or dispersion relations of these quasi particles. Then, the symmetry of their wave functions is governed by the symmetry, or the point group, of the periodic modulation. In Chapter 8, we would like to show the fact that the general rules of the formation of photonic Dirac cone can be applied to the modulated quantum well nanostructures. Our calculation results demonstrate the formation of the Dirac cone in the band structure of these quantum well with the square and triangular structural modulations. This can be used as a method for controlling the effective mass of quasi particles at will.

# Chapter 2:

# Method of calculations

## 2.1 Effective mass approximation (EMA)

### 2.1.1 Energy band of semiconductor crystals

The periodical arrangement of atoms in the crystalline structure can be represented by primitive unit cells translated along the primitive lattice vectors in the real space. Alternatively, this arrangement in crystals can be described by the reciprocal lattice in the wave vector space ($\mathbf{k}$). Electron in the crystal feel the potential from the periodically arranged atoms, and their motion can be described by the Schrödinger equation [20]:

$$H\psi_\lambda(\mathbf{k},\mathbf{r}) \equiv \left\{-\frac{p^2}{2m_0} + V_0(\mathbf{r})\right\}\psi_\lambda(\mathbf{k},\mathbf{r}) = E_\lambda(\mathbf{k})\psi_\lambda(\mathbf{k},\mathbf{r}) \tag{2.1}$$

where $p$ is the momentum of the electron, $m_0$ is the free electron mass, and $V_0$ is the periodically varying potential energy. The electron wave function satisfying the above equation has the form of the Bloch wave function:

$$\psi_\lambda(\mathbf{k},\mathbf{r}) = \frac{e^{i\mathbf{k}\cdot\mathbf{r}}}{L^{3/2}}u_\lambda(\mathbf{k},\mathbf{r}) \tag{2.2}$$

where $L^3$ is the volume of the crystal, $\lambda$ specifies the band, $u_\lambda(\mathbf{k},\mathbf{r})$ is the Bloch function that describes the wave function in the atomistic scale.

If the electron wave function (Eq. 2.2) is substituted into Eq. 2.1 and we solve the Schrödinger equation with the second order perturbation theory for the wave vector $\mathbf{k}$, the band energy dispersion shows a quadratic dependence of $\mathbf{k}$ close to the $\Gamma$ point in the first Brillouin zone. The effective mass is defined to approximate the parabolic feature in the vicinity of the band extremum.

$$m^*_\lambda = \frac{\hbar^2}{\frac{d^2E_\lambda(\mathbf{k})}{d\mathbf{k}^2}} \tag{2.3}$$

For the investigations of the electronic states close to the band extremum, the effective mass approximation is valid to approximate the effect of the periodic atoms arrangement in the crystal [19].

### 2.1.2 Calculation method for the electronic structure

For a nanostructure with confinement along certain directions, the confinement effect leads to the discrete electronic structure, which can be calculated by several calculation methods, e.g. the $\mathbf{k}\cdot\mathbf{p}$ method, empirical pseudopotential method, density functional method, and tight-binding method.

The density functional theory, empirical pseudopotential method and the tight-binding method deal with the atomistic detail of the nanostructures, which leads to high accuracy, but meanwhile suffers from the significant computational cost, especially for the big nanostructures composed of millions of atoms.

On the other hand, with the effective mass approximation (EMA), the $\mathbf{k}\cdot\mathbf{p}$ calculation is an efficient method without the requirement of a large amount of computational assumptions. It calculates the dispersion relation with the known electron wave function and energies at the $\Gamma$ point. The range of $\mathbf{k}\cdot\mathbf{p}$ calculation in the $\mathbf{k}$ space increases by increasing the number of the energy band involved. The conventional 6-band and 8-band $\mathbf{k}\cdot\mathbf{p}$ method are only accurate for the region close to the $\Gamma$ point. For the $\mathbf{k}$ space far from the $\Gamma$ point, 15-band and 30-band $\mathbf{k}\cdot\mathbf{p}$ calculation are necessary to describe the band structure of the full first Brillouin zone [92].

### 2.1.3 Single-band calculation with EMA

The nanostructures involved in my calculation mainly have the zinc-blende crystal structure, in which the CB minimum has the s-orbital character and the VB maximum has the p-orbital character. At the Brillouin zone center, the VB is doubly degenerate, which includes the heavy hole and light hole bands. In the nanostructures, this degeneracy is lifted due to the spatial confinement. Because of the small effective mass, the kinetic energy of the light hole is larger than that of the heavy hole at the Brillouin zone center. The difference between their kinetic energy is inversely proportional to the squared length in the confinement direction. Our calculation interest mainly concentrated on the transition between the low-energy electron and hole states close to the band edge. The influence of the light hole was not involved because its energy is located out of the energy range of our interest. Consequently, a single band calculation with the EMA is sufficient in our study.

To calculate the single particle energy in low-dimensional nanostructures, especially for big nanostructures with the size much larger than the lattice constant, we assume that the electron and hole wave function are given by the envelope function approximation:

$$\psi_\lambda(\mathbf{k},\mathbf{r}) = \varphi_\lambda(\mathbf{r})u_\lambda(\mathbf{k},\mathbf{r}), \tag{2.4}$$

where $\varphi_\lambda$ is the envelope function, which slowly varies over the atomic scale, and the $u_\lambda$ is the atomic part of the single particle wave function. With the EMA, the envelope function and the energy of the single particle states are calculated by solving the time-independent Schrödinger equation [20]:

$$\mathcal{H}\varphi(\mathbf{r}) = \left\{-\frac{\hbar^2\Delta}{2m^*} + V(\mathbf{r})\right\}\varphi(\mathbf{r}) = E\varphi(\mathbf{r}) \tag{2.5}$$

where $m^*$ is the effective mass, which was assumed to be isotropic in my calculations as the first-order approximation. $V(\mathbf{r})$ is the potential term including the external field as well as the confinement potential that reflects the symmetry and morphology of the nanostructures. For nanostructures with simple shapes, such as, quantum wells and disk-shaped quantum dots, solutions can be obtained by analytically solving the Schrödinger equation. If the shape of the nanostructure is complicated, a numerical method is necessary to solve the Schrödinger equation.

The finite element method (FEM) is a flexible numerical method that offers an efficient approach to the complex geometries for the calculation of energy eigenvalues of quantum mechanical systems. The basic idea of the FEM is to break up the region of interest in the problem into small elements with nodes at their ends. If we take the integration of the partial differential equation (PDE), the integration can be expressed by the summation of the integration in each element. By assuming the solution with the interpolation of basis function at each node, the solution of PDE can be obtained by calculating the eigenvalue of the matrix according to the basis functions. By decreasing the size of the element or increasing the degree of the interpolation functions, the accuracy of the solution can be improved. In the present study, the numerical calculation of the single-particle Schrödinger equation was implemented with the COMSOL multiphysics commercial FEM software.

### 2.1.4 The effect of the external field

When the external electric field or magnetic field is applied over the nanostructure, additional potential terms are induced into the potential energy part of the Schrödinger equation to consider the effect of the external field. The influence of the electric field and magnetic field on the exciton of nanostructures will be discussed in Chapter 5 and 6, respectively.

### 2.1.5 The effect of the strain in heterostructures

To realize the continuous growth of a heterostructure composed of materials with different lattice constants, the lattice points close to the interface between two materials are displaced from their original positions, which forms the strain as shown in Fig. 2.1. If the strain accumulated at the interface is larger than the critical value, the strain energy will be relaxed by forming defects. The strain changes the arrangement of the lattice points and consequently modifies the energy band. The effect of strain is introduced into the Schrödinger equation by the deformation potential. The single particle Hamiltonian with the strain-induced band edge modification will be discussed in the fourth chapter.

## 2.2 Exciton and trion calculation

### 2.2.1 Coulomb interaction

For nanostructures, the confinement limits the spatial extension of the electron and hole wave functions, so the interaction between the electrons and holes is expected to

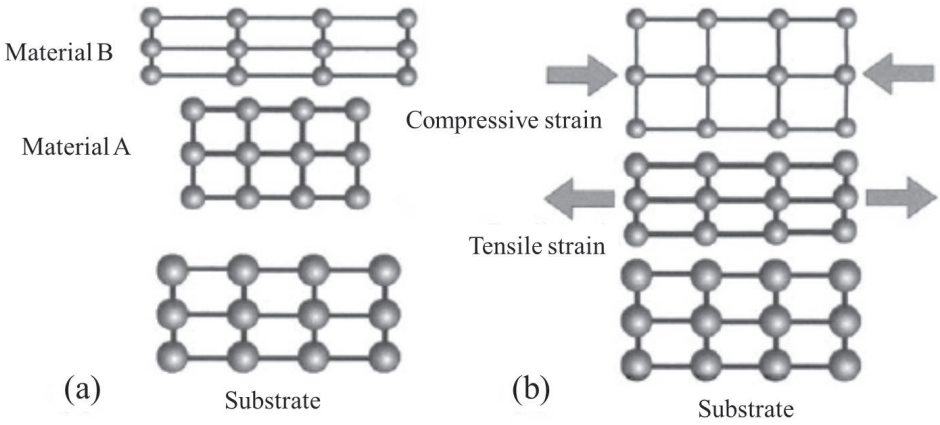


Figure 2.1: (a)The lattice of various crystals without deformation (b)The deformed lattice to fulfill the lattice match at the interface between different crystals [93].

be stronger than the bulk materials. The Coulomb interaction binds the electron and hole, which leads to a red shift with respect to the non-interacting electron-hole pair state energy. This energy shift is denoted by the binding energy ($E_b$). By modifying the overlap between the electron and hole wave functions, the Coulomb interaction also has an effect on the peak intensity of the absorption (Abs) and PL spectra. Thus, in order to investigate the optical properties of the semiconductor nanostructures, the Coulomb interaction should properly be treated.

Considering a low-dimensional semiconductor nanostructure with a size of $d$ along the confinement direction, according to the exciton Hamiltonian, the kinetic part of the Hamiltonian is proportional to $1/d^2$, meanwhile, the Coulomb interaction term is approximately proportional to $1/d$. For nanostructures with small $d$, the kinetic energy is expected to be much larger than the Coulomb energy. According to the comparison between the bulk material Bohr radius ($a_b$) and the size of the nanostructure along the confinement direction ($d$), the nanostructure can be distinguished into different quantum confinement regimes (strong confinement regime, intermediate confinement regime and weak confinement regime). In the strong confinement regime ($a_b > d$), the Coulomb interaction can be neglected in the calculation [94].

In the present study, our calculation involved the CdTe/CdS heterostructure and the GaAs/$Al_{0.3}Ga_{0.7}$As quantum nanostructures. According to S.Adachi's handbook [95], the dielectric constant of GaAs and AlAs are 12.9 and 10.06, respectively. With the linear interpolation scheme, the dielectric constant of $Al_{0.3}Ga_{0.7}$As was estimated to be 12.05 [96]. As pointed out by Peyghambarian and Koch [19], the effect of the difference in the dielectric constant on the binding energy can be neglected for the GaAs/$Al_{0.3}Ga_{0.7}$As system due to their similar values. Similarly, the effect of different dielectric constant was also neglected for the CdTe/CdSe system ($\varepsilon = 10.4$ for CdTe, $\varepsilon = 9.8$ for CdS [95]). As for the difference in the dielectric constant between the colloidal CdTe/CdSe tetrapod and the surface ligands (and the solvent), its effect was neglected in our calculation for simplicity.

In additional to the Coulomb interaction in the exciton, we can extend our study to other few-body systems, for instance, the trion (two electrons and one hole or two holes and one electron) and bi-exciton (two electrons and two holes). The increasing number of particles in the target system leads to a considerable increase in the computational cost. Thus an appropriate calculation method is necessary to deal with this problem with the reasonable calculation burden. There are several developed methods for the calculation of the few-body system, e.g. Hartree method and configuration interaction method (CI method). In the present study, the CI method was applied which fully takes the Coulomb interaction into consideration.

### 2.2.2 Configuration interaction

In this section, the CI method will be briefly introduced which is a powerful method to deal with the few-body system problem with the relatively small number of particles [94].

Let us start by considering a system with $N$ identical particles. The Hamiltonian is:

$$H = H_1 + H_2 \tag{2.6}$$

where $H_1$ is the summation of the Hamiltonians of the non-interacting $N$ particles, and $H_2$ represents the interaction among them.

Because the $N$ particles in the system are indistinguishable, the $H_0$ for each particle should be the same. For the non-interacting $N$ particles system, the wave function $\Psi$ and eigen energy $E$ can be assumed as:

$$\Psi_M(\mathbf{r}_1, \mathbf{r}_2, ..., \mathbf{r}_N) = \prod_{i=1}^{N} \psi_{m_i}(\mathbf{r}_i) \tag{2.7}$$

$$E_M = \sum_{i=1}^{N} E_{m_i} \tag{2.8}$$

where $\psi_{m_i}$ and $E_{m_i}$ are the wave function and eigen energy of the single particle state with the quantum number $m_i$, $M = [m_1, m_2, ...m_N]$ is the configuration which denotes the quantum number set of $N$ particle system.

In our study, the $N$ particles (electrons and holes) are fermions. The wave function of $N$ fermions should be antisymmetric when we apply the permutation operations on the fermions. Considering all possible ($N!$) permutations among the fermions, the wave function should be revised such that

$$\Psi_M(\mathbf{r}_1, \mathbf{r}_2, ..., \mathbf{r}_N) = \frac{1}{\sqrt{N!}} \sum_{\sigma \in Sym(N)} sgn(\sigma) \prod_{i=1}^{N} \psi_{m_{\sigma(i)}}(\mathbf{r}_i), \tag{2.9}$$

where $\sigma$ is a member of symmetric group $Sym(N)$ and $sgn(\sigma) = 1$ for even permutations and -1 for odd permutations. A compact form of the $N$ fermion wave function is the Slater determinant, which describes the feature of antisymmetry.

The Schrödinger equation for the system with $N$ identical particles is

$$H\Psi = (H_1 + H_2)\Psi = E\Psi \tag{2.10}$$

If the wave function of the $N$ interacting fermions is assumed as a linear combination of wave function bases of non-interacting fermions with configuration $M_i$:

$$\Psi(\mathbf{r}_1, \mathbf{r}_2, ..., \mathbf{r}_N) = \sum_{M_i} C_{M_i} \Psi_{M_i}(\mathbf{r}_1, \mathbf{r}_2, ..., \mathbf{r}_N) \tag{2.11}$$

multiplying $\Psi^*_{M_j}$ to Eq. 2.10 and integrate with respect to $(\mathbf{r}_1, \mathbf{r}_2, ..., \mathbf{r}_N)$, Eq. 2.10 is reduced to:

$$\sum_{M_i} C_{M_i} \left\{ E_{M_i} \delta_{M_j, M_i} + \langle M_j | H_2 | M_i \rangle \right\} = \sum_{M_i} C_{M_i} E \delta_{M_j, M_i} \tag{2.12}$$

where $E$ is the eigen energy of the $N$ interacting fermion system, $\langle M_j | H_2 | M_i \rangle$ is the interaction matrix elements. The eigen energy can be obtained by the diagonalization of the matrix $\left\{ E_{M_i} \delta_{M_j, M_i} + \langle M_j | H_2 | M_i \rangle \right\}$.

Because the number of solution for Eq. 2.12 is infinite, it is impossible to include the infinite number of wave function bases $M_i$ in the calculation. If we are only interested in the low-energy states, the summation can be truncated and only certain low-energy wave function bases are involved as an approximation. By increasing the number of involved wave function bases, the accuracy of solutions will be enhanced. Also, we can judge whether the truncated bases are sufficient by checking the convergence of the calculated eigen energy as a function of the number of bases.

For large-size nanostructures with small kinetic energy intervals that is comparable with the off-diagonal interaction matrix elements, a large number of the high-energy states are necessary to be taken into consideration because their contributions to the lowest state are not negligible. Although modern computers can deal with the CI calculation with a considerably large number of basis functions, some technique is desirable to reduce the calculation time. Considering the symmetry of the nanostructure, such as, the cylindrical symmetry, we can classify the basis states into different groups according to the selection rule of their total angular momentum, and the interaction matrix elements between the basis states from different groups are zero according to this symmetry. In each group, the energy spacing between the pair states is often large enough to obtain an acceptable convergence.

### 2.2.3 Direct Coulomb interaction and exchange interaction

In the investigation of a system composed of two indistinguishable particles, the mere product of the individual wave functions does not satisfy the permutation symmetry. The linear combination of all the permutations is required. Consider the exchange of the spatial coordinate, the wave functions of this two-particle system are

$$\Psi_\pm = \frac{1}{\sqrt{2}} [\varphi_a(\mathbf{r}_1)\varphi_b(\mathbf{r}_2) \pm \varphi_b(\mathbf{r}_1)\varphi_a(\mathbf{r}_2)] \tag{2.13}$$

where $\varphi_a$ and $\varphi_b$ are the wave functions of individual particles, and $\Psi_\pm$ is the two-particle wave function, which denotes the symmetric or antisymmetric properties with respect to the permutation.

If the interaction Hamiltonian $H_2$ in Eq. 2.10 is the Coulomb interaction. The expectation value of the second term is

$$\langle\Psi_\pm|H_2|\Psi_\pm\rangle = \langle\varphi_a(\mathbf{r}_1)\varphi_b(\mathbf{r}_2)|H_2|\varphi_a(\mathbf{r}_1)\varphi_b(\mathbf{r}_2)\rangle \pm \langle\varphi_a(\mathbf{r}_1)\varphi_b(\mathbf{r}_2)|H_2|\varphi_b(\mathbf{r}_1)\varphi_a(\mathbf{r}_2)\rangle \quad (2.14)$$

where the first and second term on the right-hand-side is the direct Coulomb interaction and exchange interaction terms, respectively.

In additional to the permutation symmetry of the spatial part of the wave function, the permutation symmetry of the spin part is also important. It is well known that the spin configuration of the two-electron system can be categorized as the spin-singlet and spin-triplet states according to their permutation symmetry [97]. When we consider the spin configuration for the electron-hole pair states, they are also categorized as spin-singlet $|ij(s)\rangle$ and spin-triplet states $|ij(t)\rangle$

$$|ij(s)\rangle = \frac{1}{\sqrt{2}}(|i\uparrow j\downarrow\rangle + |i\downarrow j\uparrow\rangle) \quad (2.15)$$

$$|ij(t)\rangle = \begin{cases} |i\uparrow j\uparrow\rangle \\ \frac{1}{\sqrt{2}}(|i\uparrow j\downarrow\rangle - |i\downarrow j\uparrow\rangle) \\ |i\downarrow j\downarrow\rangle \end{cases} \quad (2.16)$$

The Coulomb matrix elements of the spin-singlet and spin-triplet excitons can be found in Chapter 3.

Because the transitions between the spin-triplet excitons and the ground state are spin-forbidden, the spin-singlet and spin-triplet excitons correspond to the bright and dark excitons. And the exchange interaction leads to the energy splitting between the lowest bright and dark excitons. According to Ref. [98], this energy splitting shows a nearly linear dependence on the size of the nanostructures. In the present thesis, the exchange interaction was involved in my models of II-VI materials, for instance, the tetrapod-shaped nanostructures due to their small size. On the other hand, the small exchange interaction was neglected for the GaAs nanostructures due to their large size.

The main computation burden comes from the calculations of the interaction matrix elements that are multiple dimension integrals. In our study, the Coulomb matrix elements are six-dimensional integrals, which were calculated by the Monte Carlo method. The Monte Carlo method is a kind of numerical integration using the random numbers and it changes the definite integration to a summation. For the simplest case, let us consider a one-dimensional integral $\int_a^b f(x)dx$ for $x \in D = [a, b]$. By taking a large number $(N)$ of sampling random points with respect to the uniform probability distribution in the integral domain $D$, the probability of each sampling point is $p(x_i) = 1/N$. The targeting integral can be approximated with the product of the length of $D$ and the average value

of $f(\mathbf{r})$ in this domain:

$$\int_a^b f(x)dx = (b-a)\sum_{i=1}^{N} f(x_i)p(x_i) = \frac{(b-a)}{N}\sum_{i=1}^{N} f(x_i) \tag{2.17}$$

The Monte Carlo integral is a desirable method for the multiple dimension integration because the calculation time does not increase a lot with increasing integral dimensions. Its disadvantage is that the error of the solution decreases slowly by increasing the number of sampling random points. Especially when the function of the integrand seriously deviates from the uniform distribution function, the convergence of calculation is slow due to the uniform sampling strategy.

To overcome this problem, if we can roughly estimate the shape of the integrand function in advance, the strategy of random point sampling will be modified to the so-called importance sampling method. The basic idea of the importance sampling method is that a large number of sampling random points should be taken for the region where the integrand has a large value. When we induce a function $h(x)$ whose shape in $D$ is similar to the integrand $f(x)$ into Eq. 2.17 and assume the $h(x)$ is not zero for $x \in D$.

$$\int_a^b f(x)dx = \int_a^b \frac{f(x)}{h(x)}h(x)dx = \int_a^b \frac{f(x(y))}{h(x(y))}dy = \frac{(b-a)}{N}\sum_{i=1}^{N} \frac{f(x(y_i))}{h(x(y_i))} \tag{2.18}$$

where we assume $h(x) = dy/dx$ and $y(x) = \int h(x)dx$. In Eq. 2.18, the integrand $f(x(y))/h(x(y))$ become smooth in $D$. By using the uniform sampling of $y$ for the integral in Eq. 2.18, a faster convergence than Eq. 2.17 is expected. Actually the $x(y)$ in Eq. 2.18 can be considered as the random points taken with respect to the probability density function $h(x)$ similar to the integrand $f(x)$. In Fig. 2.2, by using a one-dimensional integral with the exact solution of $\pi/4$, we compare the convergence speed of the Monte Carlo integral with the uniform sampling strategy and the importance sampling strategy. A probability density function $h(x) = (4-2x)/3$ was assumed, whose accumulative distribution function can be easily obtained. The latter one shows an obviously faster convergence speed than the former one. In our study, if the integrand of the integral is the wave function of confined electronic states, we can guess the distribution function of the integrand and accelerate our calculation by the importance sampling method.

## 2.3 Calculation of the absorption spectra

The electron transition between different states leads to the photon emission or absorption. To study the transition process, the Fermi Golden rule is always applied to calculate the transition probability per unit time for the transition of an electron from an initial state $|i\rangle$ to a final state $|f\rangle$ [99].

$$P_{i,f} = \frac{2\pi}{\hbar}\left|\langle f|H_{int}|i\rangle\right|^2 \rho \tag{2.19}$$

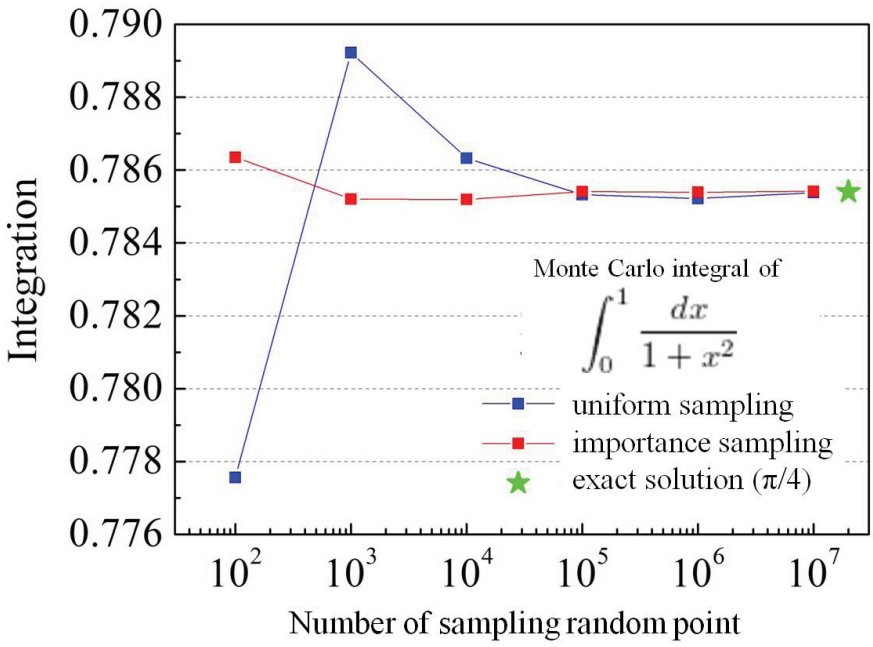


Figure 2.2: The comparison of the convergence of a one dimensional Monte Carlo integral with the uniform sampling strategy and the importance sampling strategy (with the probability density function $h(x) = (4 - 2x)/3$).

where $H_{int}$ is the Hamiltonian for the interaction between the light and the matter, $\rho$ is the density of the final states.

With the electric dipole approximation, the $H_{int}$ can be reduced to [19]

$$H_{int} = E_0 \mathbf{e}_q \cdot \mathbf{d} = \frac{E_0 e}{i m_0 \omega} \mathbf{e}_q \cdot \mathbf{p} \tag{2.20}$$

where $\mathbf{e}_q$ is the unit vector that describes the polarization direction of the incident field, $E_0$ is the electric field intensity, $\mathbf{d}$ is the electric dipole moment, $\omega$ is the frequency, $\mathbf{p}$ is the momentum, $e$ is the elementary charge and $m_0$ is the genuine electron mass.

The wave functions of the initial and final states were assumed as a product of the envelope function ($\varphi$) and the Bloch function ($u_{k=0,\lambda}$) and substituted into the dipole matrix element $\langle f|H_{int}|i\rangle$ as

$$d_{if} = \langle f|H_{int}|i\rangle = \frac{E_0 e}{i m_0 \omega}[\langle \varphi_f|\mathbf{e}_q \cdot \mathbf{p}|\varphi_i\rangle\langle u_{k=0,\lambda 2}|u_{k=0,\lambda 1}\rangle + \langle \varphi_f|\varphi_i\rangle\langle u_{k=0,\lambda 2}|\mathbf{e}_q \cdot \mathbf{p}|u_{k=0,\lambda 1}\rangle] \tag{2.21}$$

The first and the second term on the right-hand side of Eq. 2.21 correspond to the intra-band and inter-band transition. In the present thesis, I concentrate on the inter-band transition ($\lambda 1 \neq \lambda 2$), thus the 1st term in the above equation is neglected. The $\langle u_{k=0,\lambda 2}|\mathbf{e}_q \cdot \mathbf{p}|u_{k=0,\lambda 1}\rangle$ is related to the Kane matrix element [99]. It is obvious that the dipole matrix element is proportional to the overlap integral of the envelope functions. Accordingly,

$|d_{i,f}|^2$ is proportional to the squared overlap integral that indicates the probability of the electron and hole occurring at the same spatial position. Thus the spatial symmetry of the envelope function has a critical influence on the transition probability.

During the transition, the energy and momentum must be conserved. As for the inter-band transition between the p-like valence band and the s-like conduction band, the atomic part of the electron wave function has an angular momentum difference $|\Delta l| = 1$. Because the involved photon induces an additional angular momentum $l = 1$ in the dipole approximation, to keep the conservation of the momentum, the transition only takes place for the envelope functions with angular momentum difference $\Delta l = 0$, which corresponds to the dipole-allowed transition.

When the Coulomb interaction is considered, the $|d_{i,f}|^2$ is proportional to the squared overlap integral of the exciton wave function with the same physical meaning [100].

$$|d_{i,f}|^2 \propto \left| \int_V \Psi_{ex}(\mathbf{r}_e, \mathbf{r}_h) \delta(\mathbf{r}_e - \mathbf{r}_h) d\mathbf{r}_e d\mathbf{r}_h \right|^2 \tag{2.22}$$

The formulas for the band edge absorption spectra for the 3D, 2D, 1D and 0D semiconductors are shown in Koch's textbook in details [20]. In the present study, the absorption spectra of the nanostructures with 3D confinement were calculated by the equation for the quantum dots.

$$\alpha(\omega) \propto \omega \sum_f |d_{i,f}|^2 \frac{\gamma}{\gamma^2 + (\omega_f - \omega)^2} \tag{2.23}$$

where $\omega_f$ is the quantized exciton frequency corresponding to the transition energy. A series of Lorentzian peaks was introduced to smooth the absorption peaks, in which $\gamma$ is the half-width at half-maximum (HWHM) of the peaks.

In the experiment, the observed absorption peaks always have a certain full width of half maximum (FWHM) rather than the delta-function feature in the calculation, this peak width is defined as the broadening. The broadening is distinguished as the homogeneous broadening due to the electron-phonon interaction and the inhomogeneous broadening due to the size distribution of the nanostructures. If the inhomogeneous broadening is considered in the absorption spectra, the average absorption spectra can be calculated by taking the convolution of the size distribution function $f(R)$ and the absorption spectrum $(\alpha(\omega)|_R)$ for a given size of $R$ [20]. We should notice that the size distribution of the experimental specimen always leads to a large peak broadening, the low-energy peaks with small intensity may merge into adjacent strong peaks, which need to be assigned by the calculation.

# Chapter 3:

# Exciton of tetrapod-shaped nanostructures

## 3.1 Background

In 2011, we reported the first theoretical investigation of the effect of quantum tetropod shape on their exciton states by the configuration interaction method [53]. By using group theory, we found that the low energy electron and hole states had $A_1$ or $T_2$ symmetry. The low energy electron-hole pair states also have $A_1$ or $T_2$ symmetry. Consequently, the symmetry of the low energy excitons was assigned according to their main contributing pair states. A distinct selection rule for the electric-dipole transition due to the tetrahedral symmetry of quantum tetrapods was revealed and only $A_1$ excitons were optically active. Our calculation results indicated that the width of tetrapod arms has the dominant effect on the absorption peak wavelength, which showed a good agreement with available experimental data. In the present study, we applied the same method to CdTe, CdS, CdSe, ZnTe, and ZnSe quantum tetrapods with a wider range of sample parameters and examined the above five properties. To the best of our knowledge, no systematic investigation has been reported on the electronic and optical properties of those quantum tetrapods in spite of the rapid progress of their synthesis studies.

## 3.2 Theory and model

We assume the tetrahedral symmetry for quantum tetrapods to clarify their unique electronic and optical properties caused by their structural symmetry, although it is known that there are various types of non-symmetric deformation in actual specimens. Then, Fig. 3.1 shows the structure and band diagram of the quantum tetrapods that we analyze in this study. They consist of a spherical central core and four cylindrical arms. Because early experimental studies showed that the core had a zinc blende structure whereas the arms had a wurtzite structure [25, 33, 34], we generally assume non-zero band offsets between the core and arms as shown in Fig. 3.1(b) except ZnSe and ZnTe tetrapods for which both the core and arms have the zinc blende structure [41, 42].

We deal with both electron and hole states of quantum tetrapods by the single-band effective-mass approximation, which is justified when we only treat relatively low energy states close to the absorption edge. The valence band actually consists of heavy and light hole states. Their energy difference is 16 meV for wurtzite CdS, for example, and they are mixed by the confinement potential. However, the kinetic energy of the light hole is generally larger than the heavy hole due to the smaller effective mass of the former, so the light hole states are less important when we discuss the low energy part of the absorption spectrum. This was proven, for example, by Ref. [101] that showed a good agreement

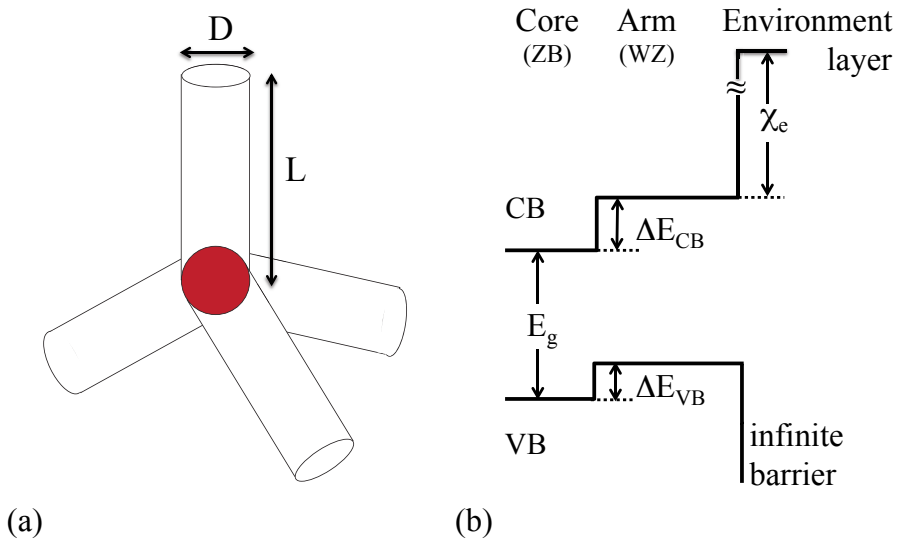


Figure 3.1: (a) Structure and (b) band diagram of quantum tetrapods. We assume the perfect tetrahedral symmetry for their structure, which consists of a spherical central core and four cylindrical arms. We denote the diameter and length of the arms by $D$ and $L$, respectively. The diameter of the central core is assumed to be the same as $D$. In the band diagram, we generally assume different energy values for the core and arm, since early experimental studies revealed that the core had a zinc blende structure whereas the arms had a wurtzite structure. The confinement potential height of the conduction band is assumed to be the same as the electron affinity ($\chi_e$), while an infinite potential barrier is assumed for the valence band. The band gap is denoted by $E_{\mathrm{g}}$ and the band offsets between the arm and core are denoted by $\Delta E_{\mathrm{CB}}$ and $\Delta E_{\mathrm{VB}}$ for the conduction and valence bands, respectively [54].

Table 3.1: Parameters used in the present calculation. $m_0$ is the genuine electron mass. See Fig. 3.1 for the definition of $\Delta E_{\mathrm{CB}}$, $\Delta E_{\mathrm{VB}}$, and $\chi_e$ [54].

| Material | $E_{\mathrm{g}}$ (eV) | $m_e^*$ ($m_0$) | $m_h^*$ ($m_0$) | $\Delta E_{\mathrm{CB}}$ [102] (eV) | $\Delta E_{\mathrm{VB}}$ [102] (eV) | $\chi_e$ [103] (eV) | $\varepsilon$ [95] |
|---|---|---|---|---|---|---|---|
| $\mathrm{CdSe}^{\mathrm{ZB}}$ | 1.74 [104] | 0.11 [105] | 0.44 [105] | | | | 9.6 |
| $\mathrm{CdSe}^{\mathrm{WZ}}$ | 1.799 | 0.13 [106] | 0.45 [106] | 0.094 | 0.035 | 4.95 | |
| $\mathrm{CdS}^{\mathrm{ZB}}$ | 2.5 [107] | 0.14 [105] | 0.51 [105] | | | | 9.8 |
| $\mathrm{CdS}^{\mathrm{WZ}}$ | 2.579 | 0.205 [108] | 0.7 [108] | 0.115 | 0.046 | 4.79 | |
| $\mathrm{CdTe}^{\mathrm{ZB}}$ | 1.5 [34] | 0.11 [109] | 0.69 [109] | | | 4.18 [110] | 10.4 |
| $\mathrm{CdTe}^{\mathrm{WZ}}$ | 1.547 | 0.11 | 0.69 | 0.065 | 0.018 | | |
| $\mathrm{ZnSe}^{\mathrm{ZB}}$ | 2.67 [111] | 0.165 [112] | 0.57 [113] | | | 4.09 | 8.9 |
| $\mathrm{ZnTe}^{\mathrm{ZB}}$ | 2.29 [114] | 0.122 [115] | 0.6 [116] | | | 3.53 | 9.4 |

between the single-band and the multi-band calculations of low-energy exciton states in CdTe/CdSe core-shell quantum dots. As we will show in the following, the single-band calculation for quantum tetrapods also gives a good agreement with available experimental data. As for the selection rule, on the other hand, we do not think that there is a difference even when we take the light hole into consideration, since the structural symmetry is $T_d$ and is sufficiently low. So, we assume the following forms for the electron and hole wave functions:

$$\psi_e(\mathbf{r}_e) = \varphi_e(\mathbf{r}_e)u_e(\mathbf{r}_e), \tag{3.1}$$
$$\psi_h(\mathbf{r}_h) = \varphi_h(\mathbf{r}_h)u_h(\mathbf{r}_h), \tag{3.2}$$

where $\varphi_e$ ($\varphi_h$) and $u_e$ ($u_h$) are the envelope function and atomic wave function of the CB electron (VB heavy hole), respectively. The electron and hole coordinates are denoted by $\mathbf{r}_e$ and $\mathbf{r}_h$. The envelope functions are obtained by solving the Schrödinger equation assuming an isotropic effective mass for both the electron ($m_e^*$) and heavy hole ($m_h^*$):

$$\mathcal{H}_e\varphi_e(\mathbf{r}_e) \equiv \left\{-\frac{\hbar^2\Delta_e}{2m_e^*} + V_e(\mathbf{r}_e)\right\}\varphi_e(\mathbf{r}_e) = E_e\varphi_e(\mathbf{r}_e), \tag{3.3}$$
$$\mathcal{H}_h\varphi_h(\mathbf{r}_h) \equiv \left\{-\frac{\hbar^2\Delta_h}{2m_h^*} + V_h(\mathbf{r}_h)\right\}\varphi_h(\mathbf{r}_h) = E_h\varphi_h(\mathbf{r}_h), \tag{3.4}$$

where $\Delta$ is the Laplace operator, $V$ is the confinement potential, and $E$ is the energy eigenvalue. The numerical calculation was conducted by the finite element method using commercial software COMSOL Multiphysics. Material parameters assumed in this study are listed in Table 3.1.

Because we assume the tetrahedral symmetry for the quantum tetrapod structure, the confinement potential $V$ is invariant for any symmetry operation $R$ of point group $T_d$.

Since the Laplace operator is also invariant for $R$, the single-particle Hamiltonian $\mathcal{H}_{e,h}$ commutes with $R$:

$$R\mathcal{H}_{e,h}R^{-1} = \mathcal{H}_{e,h} \quad (^\forall R \in T_d). \tag{3.5}$$

Therefore, the eigen functions $\varphi_e$ and $\varphi_h$ are irreducible representations of point group $T_d$. It has two one-dimensional representations ($A_1$ and $A_2$), one two-dimensional representation ($E$), and two three-dimensional representations ($T_1$ and $T_2$) [117].

For exciton energy levels and wave functions, we calculate them by numerical diagonalization of configuration interaction Hamiltonian. We solve the following two-body Schrödinger equation based on the expansion of the total wave function $\Psi$ by the linear combination of pair states of electron and hole envelope functions:

$$\mathcal{H}_X\Psi(\mathbf{r}_e,\mathbf{r}_h) \equiv \left(\mathcal{H}_e + \mathcal{H}_h - \frac{e_0^2}{4\pi\varepsilon_0\varepsilon|\mathbf{r}_e-\mathbf{r}_h|}\right)\Psi(\mathbf{r}_e,\mathbf{r}_h) = E_X\Psi(\mathbf{r}_e,\mathbf{r}_h), \tag{3.6}$$

$$\Psi(\mathbf{r}_e,\mathbf{r}_h) = \sum_{i,j} a_{ij}\varphi_e^{(i)}(\mathbf{r}_e)\varphi_h^{(j)}(\mathbf{r}_h), \tag{3.7}$$

where $e_0$ denotes the elementary charge, $\varepsilon_0$ is the permittivity of free space, and $\varepsilon$ is the dielectric constant of the quantum tetrapod. Because the Coulomb term is also invariant for any symmetry operation $R$ of $T_d$, the exciton Hamiltonian $\mathcal{H}_X$ also commutes with $R$:

$$R\mathcal{H}_X R^{-1} = \mathcal{H}_X \quad (^\forall R \in T_d). \tag{3.8}$$

Therefore, the exciton wave function $\Psi$ is an irreducible representation of point group $T_d$ as well.

It is important to note that only pair states of the $A_1$ symmetry contribute to the dipole-allowed optical transition, since the following overlap integral ($I_\mathrm{o}$) is non-zero only for the $A_1$ symmetry:

$$I_\mathrm{o} = \int d\mathbf{r}\varphi_e^*(\mathbf{r})\varphi_h(\mathbf{r}). \tag{3.9}$$

Because the exciton wave function and the constituent pair states in Eq. (3.7) should have the same symmetry, only excitons of the $A_1$ symmetry contribute to the dipole-allowed optical transition. As a consequence, if the lowest exciton has another symmetry, quantum tetrapods are essentially non-luminescent.

In our calculation of the Coulomb energy, we did not take into consideration the surface polarization charge induced by the discontinuity of the dielectric constant as was done for spherical quantum dots in Ref. [118]. This is because we cannot obtain its analytical solution for the tetrapod geometry in contrast to the spherical geometry, so we have to rely on the numerical solution of Poisson's equation to evaluate the Coulomb term, which is quite time-consuming and impractical in the theoretical framework of the present study. The neglect of the surface polarization charge may result in the underestimation of the binding energy of excitons. This matter remains a future problem.

To evaluate the Coulomb term, we should take into consideration the exchange interaction for different spin configurations. For spin-singlet pair states, we can easily prove that the matrix element of the two-body part ($\mathcal{H}_2$) of the exciton Hamiltonian

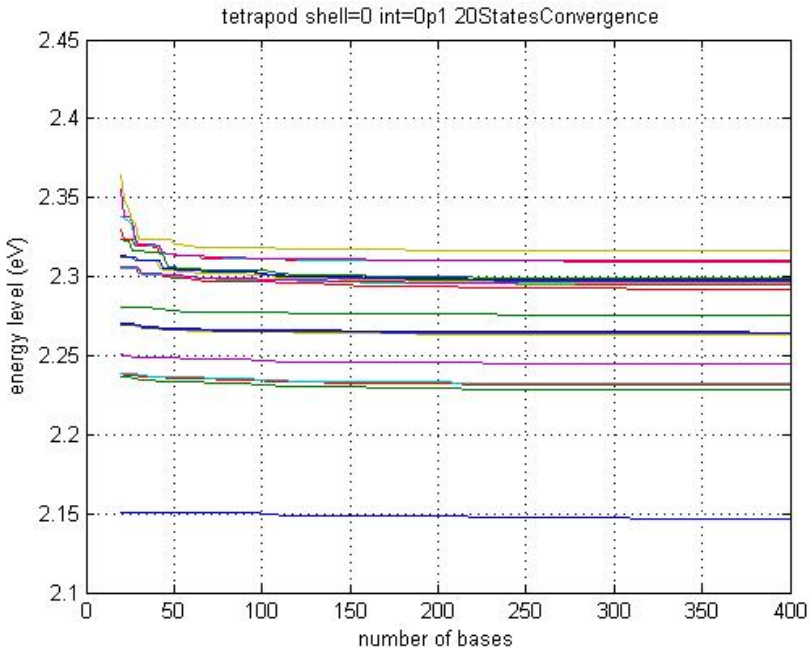


Figure 3.2: Energy convergence of the lowest twenty exciton states as a functoin of the number of pair state basis of tetrapod-shaped nanocrystals.

$(\mathcal{H}_X)$ is given by

$$\langle kl(s)|\mathcal{H}_2|ij(s)\rangle = \langle kj|H_2|il\rangle - 2\langle jk|H_2|il\rangle\,, \tag{3.10}$$

where

$$\langle kj|H_2|il\rangle = -\int\int d\mathbf{r}_1 d\mathbf{r}_2 \varphi_h^{(j)*}(\mathbf{r}_2)\varphi_e^{(k)*}(\mathbf{r}_1)\frac{e_0^2}{\varepsilon_0\varepsilon|\mathbf{r}_1-\mathbf{r}_2|}\varphi_e^{(i)}(\mathbf{r}_1)\varphi_h^{(l)}(\mathbf{r}_2), \tag{3.11}$$

etc. For spin-triplet pair states, the matrix element of the two-body part only has the Coulomb term:

$$\langle kl(t)|\mathcal{H}_2|ij(t)\rangle = \langle kj|H_2|il\rangle\,. \tag{3.12}$$

The multiple dimension integrals in Eq. (3.11) were calculated by the standard Monte Carlo method. Convergence of the exciton energy was checked by increasing the number of electron-hole pair states basis up to 400. As shown in Fig. (3.2), with increasing number of pair state bases, the exciton energy showed a fast convergence. Because the Bohr radius ($a_{\rm B}$) of the semiconductor materials analyzed in the present study is from 2.6 nm (CdS) to 6.5 nm (CdTe), the structural size of the tetrapod that is represented by $D$ satisfies $D/2 \leq a_{\rm B}$ in most cases, which means that the system is in the strong confinement regime. So, the Coulomb energy is relatively small compared with the kinetic energy, which justifies our numerical method of the diagonalization of the configuration interaction Hamiltonian. It also brings about distinct peaks in the absorption spectra in spite of the large inhomogeneous broadening as will be shown in the following section.

We found that most of the electron and hole wave functions in the low energy range

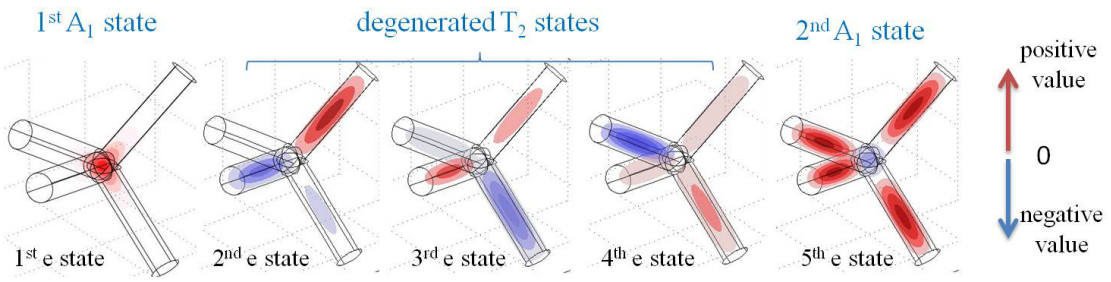


Figure 3.3: Wave functions of the lowest five electron states of bare tetrapod-shaped nanocrystals.

are characterized by the angular momentum around the arm axis, $l$, and the number of nodes along the arm axis, $n$, since four arms are approximately independent being separated by the central core and the arms have a cylindrical symmetry. We also found that as far as the low energy range close to the absorption edge is concerned, important contribution is made by one-particle states with $l = 0$. Then, it is convenient to know their possible symmetry in advance, since we can judge whether they can contribute to the dipole-allowed optical transition. When we denote the electron or hole wave function localized in the $i$th arm by $\phi_i$, it is easy to see that their symmetric combination gives a wave function of the $A_1$ symmetry of point group $T_d$:

$$\phi_{A_1} = \frac{1}{2}\left(\phi_1 + \phi_2 + \phi_3 + \phi_4\right). \tag{3.13}$$

The remaining three independent linear combinations give the basis of a $T_2$-symmetric energy level:

$$\phi^{(1)}_{T_2} = \frac{1}{2}\left(\phi_1 + \phi_2 - \phi_3 - \phi_4\right), \tag{3.14}$$

$$\phi^{(2)}_{T_2} = \frac{1}{2}\left(\phi_1 - \phi_2 + \phi_3 - \phi_4\right), \tag{3.15}$$

$$\phi^{(3)}_{T_2} = \frac{1}{2}\left(\phi_1 - \phi_2 - \phi_3 + \phi_4\right). \tag{3.16}$$

In our calculation, the arm of our tetrapod model was of a cylinder shape, so the electron and hole wave functions in the arm must have cylindrical symmetry about its axis. Azimuthal quantum number $l$ can be used to distinguish the feature of cylindrical symmetry of different states. Since we only consider the low energy states, which have $l = 0$, they are symmetric under the mirror reflection operation about a diagonal plane ($\sigma_d$). Consulting the character table of point group $T_d$ shown in Table 3.2, the low energy states with $l = 0$ can only realize the $A_1$ and $T_2$ symmetry. This is consistence with our previous discussion in Eqs. (3.13)-(3.16).

Because the single-particle state with the $T_2$ symmetry are 3-fold degenerate, we can find out the accuracy of numerical calculation by examining the relative error of the energy for three $T_2$ states. The relative error for 3-fold degenerate electron (hole) states

Table 3.2: The character of point group $T_d$. The symmetry operations are listed in the first row. The irreducible representations of point group $T_d$ are listed in the first column.

| $T_d$ | $E$ | $6IC_4$ | $3C_2$ | $6\sigma_d$ | $8C_3$ |
|---|---|---|---|---|---|
| $A_1$ | 1 | 1 | 1 | 1 | 1 |
| $A_2$ | 1 | -1 | 1 | -1 | 1 |
| $E$ | 2 | 0 | 2 | 0 | -1 |
| $T_1$ | 3 | 1 | -1 | -1 | 0 |
| $T_2$ | 3 | -1 | -1 | 1 | 0 |

was $1.0 \times 10^{-4}$ ($5.8 \times 10^{-7}$), which indicated sufficient accuracy in our calculation.

The lowest electron wave function, which has the $A_1$ symmetry, is localized in and around the central core as shown in Fig 3.3. It is worth noting that we can tell the symmetries of low energy excitons from this fact. Actually, the pair states composed of the lowest electron level and low energy hole levels, the latter of which have $A_1$ or $T_2$ symmetry as mentioned above, can only have $A_1$ or $T_2$ symmetry, which can be easily verified by using the well-known reduction formula of group theory [117]. By using the configuration interaction method in our calculation, the dominantly contributing pair state for each exciton can be found. Furthermore, the symmetry of excitons can be assigned according to the symmetry of contributing pair states. Therefore, excitons in the low energy range close to the absorption edge are characterized by the $A_1$ and $T_2$ symmetries, among which only $A_1$ excitons contribute to dipole-allowed optical transitions. As a consequence, if the lowest exciton has the $T_2$ symmetry, quantum tetrapods are non-luminescent unless thermal excitation induces a non-vanishing population of higher energy $A_1$ excitons.

## 3.3 Results and discussion

Figure 3.4 shows the $D$ (arm diameter) dependence of the lowest twenty exciton energies for CdTe, CdS, CdSe, ZnTe, and ZnSe quantum tetrapods. From our previous study [53], we found that the $L$ (arm length) dependence of the exciton energy was small, so we fixed it to 9 nm, which is a typical value observed in experiments. On the other hand, we varied $D$ from 2.2 to 7 nm in order to compare our numerical results with available experimental data. We also examined the wave functions of the lowest twenty electron and hole states, which govern the absorption and emission spectra in the vicinity of the absorption edge, and found that all of them were characterized by the angular momentum of $l = 0$ and had $A_1$ or $T_2$ spatial symmetry. In a higher energy range, we also found $l \geq 1$ states. But they were not important for the energy range that we deal with in this study.

As we described in the previous section, all these excitons have $A_1$ or $T_2$ symmetry. They show an apparent blue shift with decreasing $D$ as a consequence of quantum confinement of exciton wave functions. Most of the lowest spin-singlet excitons have the $A_1$ symmetry in our results, so those quantum tetrapods are luminescent. Exceptions are

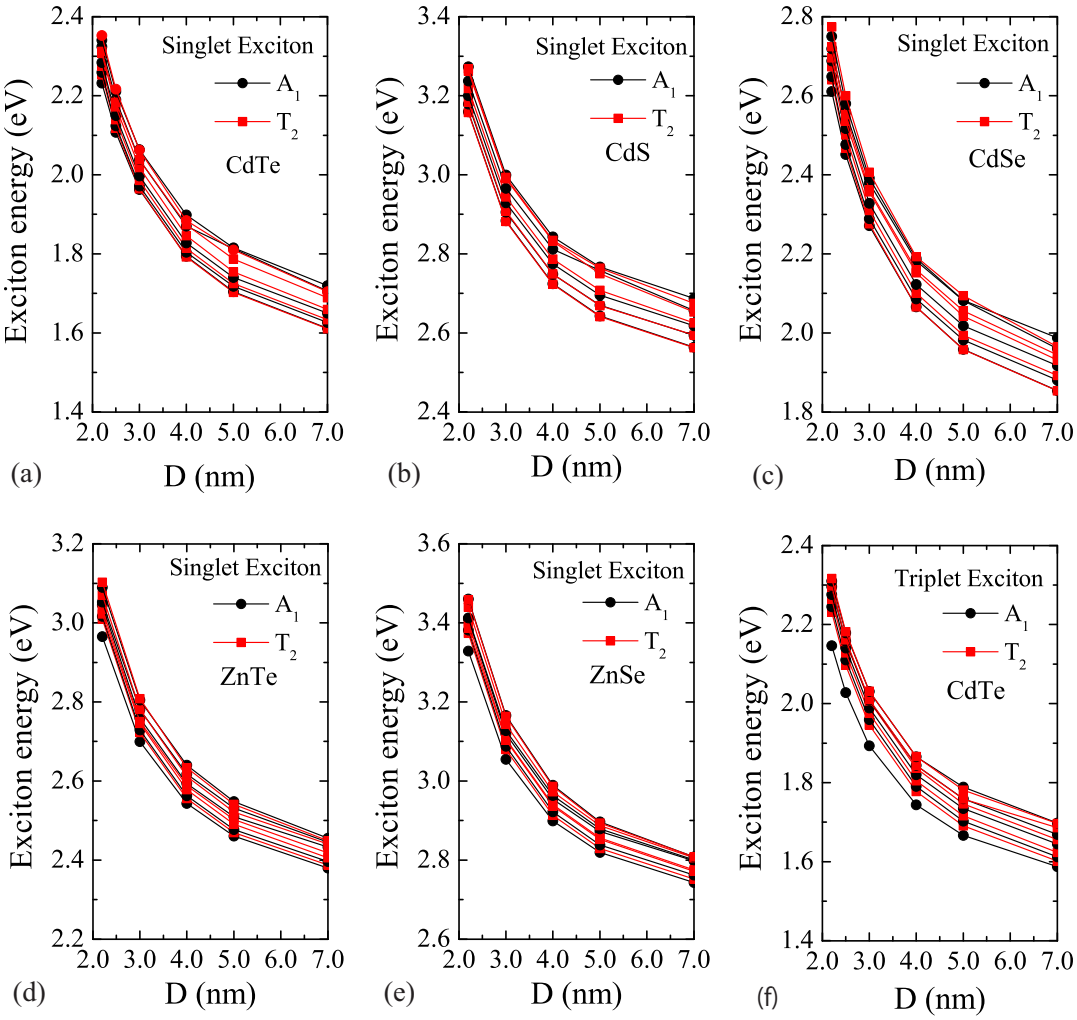


Figure 3.4: The $D$ dependence of the spin-singlet exciton energy of quantum tetrapods made of (a) CdTe, (b) CdS, (c) CdSe, (d) ZnTe, and (e) ZnSe. (f) Spin-triplet exciton energy of the CdTe quantum tetrapod [54].

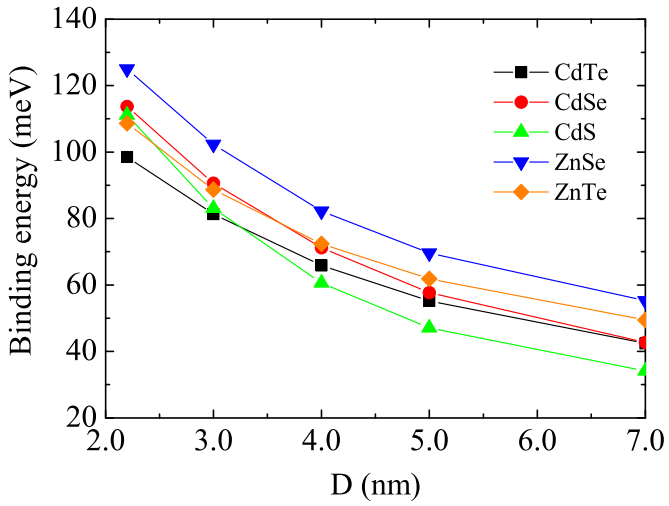


Figure 3.5: The $D$ dependence of the binding energy of the lowest spin-triplet exciton [54].

CdS for all $D$, CdTe with $D \geq 4$ nm, and CdSe with $D \geq 5$ nm. Their lowest spin-singlet excitons have the optically inactive $T_2$ symmetry, so they are basically non-luminescent. However, the energy difference between this lowest $T_2$ and the lowest $A_1$ excitons is less than 2 meV. So, the room-temperature thermal energy (26 meV) mixes the population of these two exciton states and luminescence from the $A_1$ exciton level must be observed.

In Fig. 3.4(f), the energy of spin-triplet excitons is shown. As we found for CdTe tetrapods with 1.9 nm $\leq D \leq$ 2.2 nm in our previous study [53], the binding energy of the lowest spin-triplet exciton, which is defined by the energy difference between the lowest pair state and the lowest spin-triplet exciton state, is exceptionally large due to the strong confinement of both electron and hole wave functions to a small central-core region, and so, the large negative Coulomb energy. This binding energy decreases with increasing $D$ because of the delocalization of the wave functions. As shown in Fig. 3.5, this tendency is common to all tetrapods that we dealt with in this study.

Because we obtained the energy levels and wave functions, we could calculate the absorption spectra of quantum tetrapods according to Fermi's golden rule. The absorption spectra of CdTe tetrapods are shown in Fig. 3.6. Because the single-band approximation is appropriate for the low energy range around the absorption edge, we focused on the lowest and second lowest absorption bands in our calculation, for which the single-band approximation can safely be applied. A continuum of higher energy absorption bands should follow these two bands. The actual specimens of quantum tetrapods have a fairly large size distribution. So, we rather arbitrarily assumed an inhomogeneous width of 60 meV (FWHM) for each absorption line. This value corresponds to the diameter-size ($D$) distribution of about 0.5 nm on average, which was deduced from the $D$ dependence of the exciton energy shown in Fig. 3.4. This value (0.5 nm) of the diameter-size distribution is among the typical values found in experimental studies. In addition to an obvious quantum confinement effect, the relative decrease of the lowest band intensity with increasing $D$

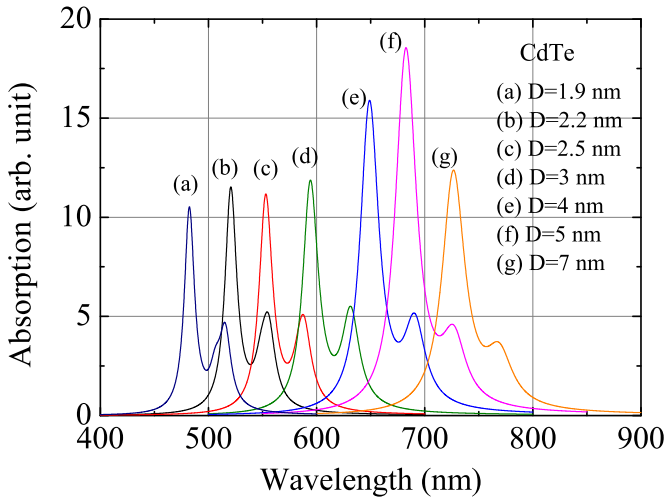


Figure 3.6: The $D$ dependence of the absorption spectrum of the CdTe tetrapod [54].

is observed in Fig. 3.6, which is caused by the decrease of the overlap integral of the lowest electron and hole wave functions mainly due to the delocalization of the latter with increasing $D$. This point will be discussed again later in connection with Fig. 3.8.

It is worth noting the difference in the optical properties between quantum tetrapods and spherical QDs. According to our calculation results, the lowest absorption peak has the main contribution from the lowest exciton state with the $A_1$ symmetry, which consists of the lowest electron and hole states with wave functions strongly localized in the core part of the quantum tetrapods. This situation is similar to the spherical QDs, whose lowest exciton also has the $A_1$ symmetry. For higher energy $A_1$ excitons in quantum tetrapods, their wave functions are mainly in the arm part. Comparing with the spherical QDs, the arms of tetrapods under weak spatial confinement will lead to small exciton energy intervals and weak absorption peak intensity due to the reduction of the wave-function overlap integral between electron and hole. The rotational symmetry in the arms with angular momentum $l = 0$ will also leads to the single particle states with $T_2$ symmetry, which lead to $T_2$ excitons that do not contribute to dipole-allowed transitions. When $l \neq 0$ in the arms, the states with $T_1$ and $E$ symmetry are also present, which are not found in the spherical QDs.

Figure 3.7 shows the absorption spectra of five kinds of quantum tetrapods, where $D$ is fixed to 3 nm. Their spectral shift is mainly caused by the change in the band gap energy.

Finally, Fig. 3.8 shows the $D$ dependence of the lowest absorption peak energy and its comparison with experiments, where the amount of the $D$ dependence is mainly governed by the kinetic energy of carriers, and so, by their effective mass. Experimental data are mainly available for CdTe and CdSe tetrapods. If we take into consideration the fairly large size distribution and structural deformation from the perfect tetrahedral symmetry in actual specimens, we may conclude that the agreement between our calculation and the

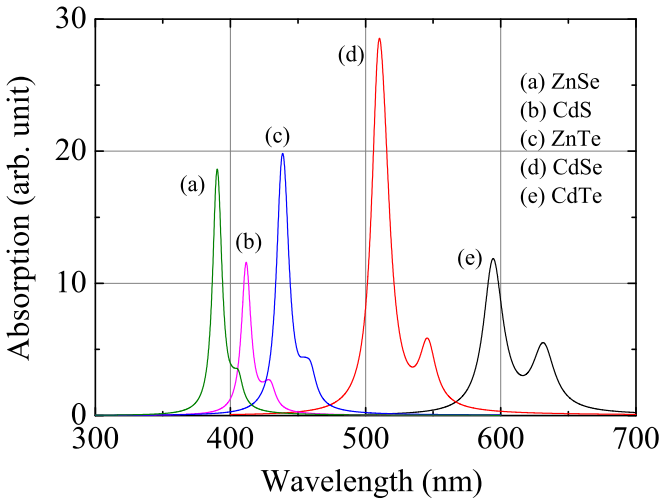


Figure 3.7: The material dependence of absorption spectra. $D$ was assumed to be 3 nm [54].

experimental observation is good.

However, there is a somewhat systematic deviation between them for the CdTe tetrapod with $D \geq 3$ nm. This deviation may be explained by the relative decrease of the lowest band intensity compared with the second lowest band. If the inhomogeneous width is large, the lowest band may be difficult to identify experimentally and the second band may be regarded as the absorption edge. From this point of view, the calculated peak energy of the second band is also plotted in Fig. 3.8(a), which shows considerably good agreement with the experimental data for $D \geq 4$ nm.

We also quantitatively evaluated the influence of arm phase on the exciton energy of tetrapods and showed the results in Fig. 3.9. It's worth noting that changing the arm phase from wurtzite to zinc blende led to an energy decrease of the lowest spin-singlet exciton. The change in the binding energy of the lowest exciton induced by different arm phases was less than 3 meV for the entire range of $D$ in the present calculation, which is considerably smaller than the change in the exciton energy. Therefore, the difference in the exciton energy mainly derived from the change in one-particle energy of electron and hole. This exciton energy difference increased with decreasing $D$, which was caused by the larger band gap of the wurtzite arms where a larger portion of electron wave function is distributed for smaller $D$.

## 3.4 Conclusion

We systematically investigated exciton states of CdTe, CdS, CdSe, ZnTe, and ZnSe quantum tetrapods by numerical diagonalization of configuration interaction Hamiltonian with the single-band effective-mass approximation. We found five main features of their electronic and optical properties: (1) the lowest twenty electron and hole states, which gov-

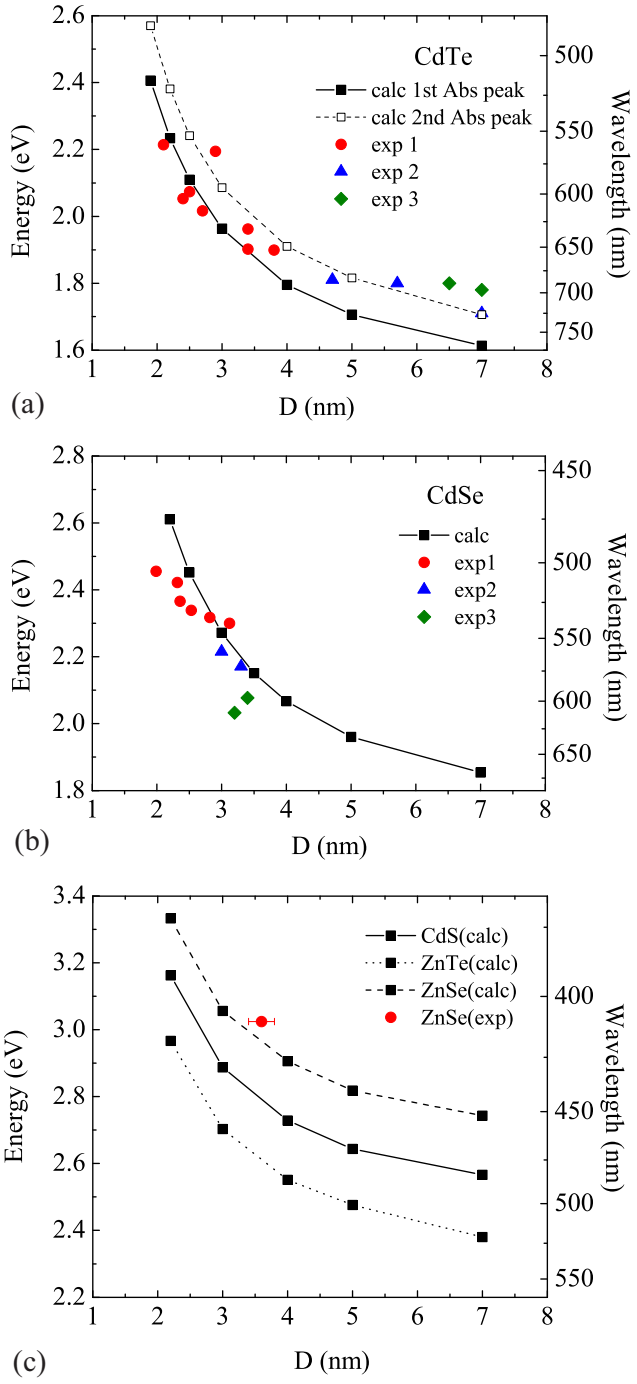


Figure 3.8: (a) The $D$ dependence of the peak energy of the lowest (black square) and second lowest (white square) absorption bands calculated for CdTe quantum tetrapods and the lowest absorption peak energy observed in Ref. [39] (exp1, circle), Ref. [34] (exp2, triangle), and Ref. [33] (exp3, diamond). (b) The peak energy of the lowest absorption band of CdSe quantum tetrapods: calculation (black square) and observation in Ref. [31] (exp1, circle), Ref. [29] (exp2, triangle), and Ref. [30] (exp3, diamond). (c) The lowest absorption peak energy calculated for CdS, ZnTe, and ZnSe quantum tetrapods (square) and observed for ZnSe (Ref. [42], circle) [54].

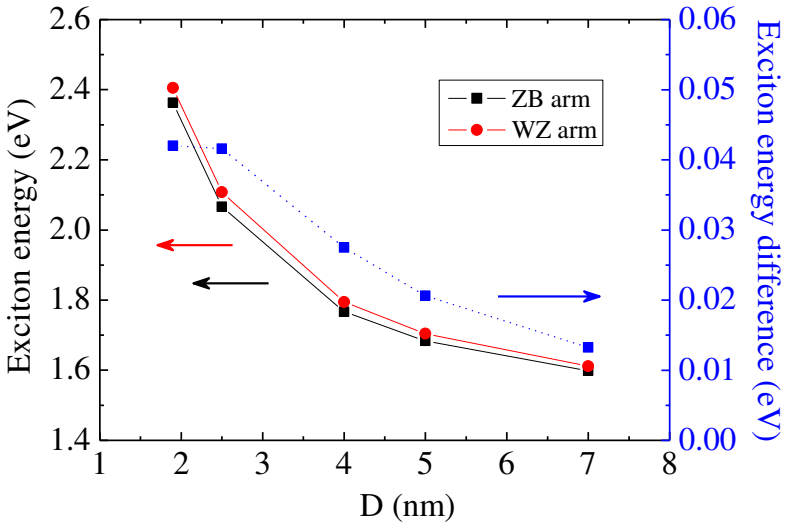


Figure 3.9: The lowest spin-singlet exciton energy of CdTe tetrapods with wurtzite and zinc blende arms, and their energy difference as a function of $D$.

ern the absorption and emission spectra in the vicinity of the absorption edge, have $A_1$ or $T_2$ symmetry; (2) the lowest twenty exciton states have the $A_1$ or $T_2$ symmetry as well; (3) most of the lowest spin-singlet excitons have the $A_1$ symmetry, so they are optically active and luminescent. Even when it is of $T_2$ symmetry, the room-temperature thermal energy induces non-vanishing population in the lowest $A_1$ exciton, so the tetrapod can essentially be luminescent; (4) the binding energy of the lowest spin-triplet exciton is exceptionally large, for small $D$ in particular, because of the large Coulomb interaction between electron and hole due to their efficient confinement into the small central-core region; (5) the wavelength of the lowest absorption band agrees well with available experimental data.

# Chapter 4:

# Exciton of the tetrapod-shaped core-shell nanostructure

## 4.1 tetrapod-shaped core-shell nanostructure

In the previous chapter, we revealed the influence of the tetrahedral symmetry of II-VI tetrapod nanostructures on their electronic and optical properties. Now we extend our study to tetrapod-shaped heterostructures recently synthesized by chemical methods [57, 119–123]. The surface of a bare tetrapod nanostructure is partly covered by another II-VI material that forms the tetrapod-shaped core-shell nanostructure (csTPs).

In the present chapter, we applied the same theoretical method to the exciton states of CdTe/CdS csTP nanocrystals (NCs) with different dimensions. We concentrated on the following two aspects: Firstly, the influence of tetrahedral symmetry on the electronic structures of the csTPs by using the group theory. A comparison with core-shell spherical NCs revealed a uniquely efficient carrier separation in the csTPs. Secondly, the effect of strain on the electronic properties was investigated. In addition to the investigation of excitons in csTPs with perfect tetrahedral symmetry, we also discussed the effect of broken symmetry. For the CdTe/CdS csTPs with a type-II band structure, the distinct peaks in absorption spectra are mainly contributed by the high-energy exciton states, which are beyond the range of the present investigation.

## 4.2 Model of strained nanoheterostructures

Figure 4.1(a) shows the three-dimensional structure of the CdTe/CdS csTP that we assumed in our numerical study in accordance with the observation reported in Ref. [57]. It consists of a spherical central core (CdTe with zinc-blende structure), four cylindrical arms (CdTe with wurtzite structure), and four CdS shells (CdS with wurtzite structure) covering the lateral surfaces of the arms. The shells on the csTP arms are assumed to be isolated from each other. The maximum shell thickness, the diameter and length of the arms are denoted by $sh$, $D$ and $L$, respectively.

The shells on all the arms were assumed to be the same except for their spatial orientation, thus this csTP model exhibited perfect tetrahedral symmetry as the bare tetrapods in Ref. [53]. The band diagrams for the electrons and holes of the bulk CdTe and CdS are shown in Fig. 4.1(b). When the effect of strain is taken into consideration, these band diagrams will be modified due to the distortion of the lattice framework.

The approach described in Ref. [125] for a freestanding structure was used in our study to calculate the strain distribution over the entire csTP heterostructure. We applied

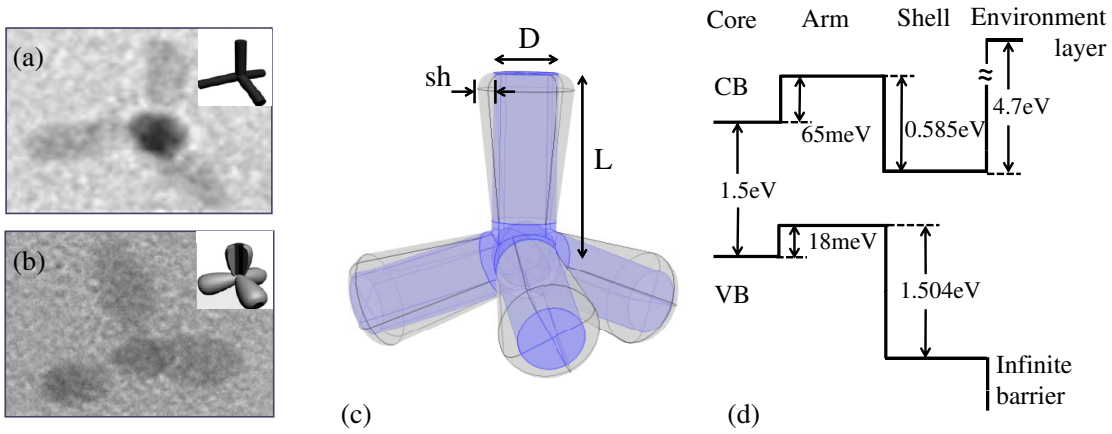


Figure 4.1: SEM images of (a) bare tetrapod and (b) core-shell tetrapod. (c) Structure of the CdTe/CdS core-shell tetrapod assumed in the calculation. It consists of a spherical central core (CdTe with zinc blende structure), four cylindrical arms (CdTe with wurtzite structure), and four CdS shells covering the arms. The maximum shell thickness and the diameter and length of the arms are denoted by $sh$, $D$ and $L$, respectively. The diameter of the central core is assumed to be the same as $D$. (d) Energy band diagrams for electrons and holes. The confinement potential height of CB is assumed to be the same as the electron affinity. 4.7 eV is assumed for the CdS electron affinity, which is the sum of the electron affinity (4.18 eV) for CdTe with the zinc blende structure [110] and the CB offset between CdTe and CdS [123], whereas 1.5 eV is assumed for the zinc blende CdTe bandgap [34]. An infinite potential barrier is assumed for the VB. As for the band offset between the CdTe with the zinc blende and wurtzite structures, we used 65 meV for the CB and 18 meV for the VB, which were obtained by theoretical calculation [102]. For the effective masses of the electrons ($m_e^*$) and heavy holes ($m_h^*$), we assumed $m_e^* = 0.11 \times m_0$ and $m_h^* = 0.69 \times m_0$ for CdTe [109] and $m_e^* = 0.18 \times m_0$ and $m_h^* = 0.7 \times m_0$ for CdS [50], where $m_0$ is the genuine electron mass [124].

the continuum elasticity approximation, which assumes that the heterostructure has a coherent interface where the lattice points of the constituent materials match each other perfectly.

To fulfill the interface matching requirement, we initially assumed an interface matching configuration with unstrained CdTe arms and a deformed shell. Considering the gradual growth of the thin shell on the arm, the CdTe arm was initially assumed to be the unstrained substrate [125]. The central core was assumed to be a part of the unstrained substrate due to the lattice similarity between the wurtzite CdTe arm and zinc-blende CdTe core at their interface. The deformation is denoted by $\mathbf{u^0}$ ($\mathbf{u^0} = \mathbf{0}$ in the arm), which produces anisotropic initial strain $\varepsilon^0_{xx} = \varepsilon^0_{yy} = (a^A - a^S)/a^S$, and $\varepsilon^0_{zz} = (c^A - c^S)/c^S$, in which the superscript A(S) denotes the arm (shell)domain in the csTP model, and $a$ and $c$ are the lattice constants of wurtzite crystals. The lattice constants used in our calculation were $a = 0.457$ nm, $c = 0.747$ nm [126] and $a = 0.4136$ nm, $c = 0.6713$ nm [127] for wurtzite CdTe and CdS, respectively. With the interface matching assumption, no rotation was considered for the initial strain. Thus the initial strain tensor had zero off-diagonal elements. The initial strain can be expressed as:

$$\varepsilon^0_{ij} = \frac{1}{2}\left(\frac{\partial u^0_i}{\partial x_j} + \frac{\partial u^0_j}{\partial x_i}\right) \quad i, j = x, y, z \tag{4.1}$$

where $u_i$ is a component of the deformation $\mathbf{u^0}$.

It should be noted that the interface matching configuration is not an equilibrium configuration. The system will deform with respect to the interface matching configuration and relax to equilibrium with the lowest elastic energy, while maintaining the interface matching. During this relaxation, the deformation vector is defined as $\mathbf{u}$. The consequent elastic strain is related to the components of $\mathbf{u}$:

$$\varepsilon^e_{ij} = \frac{1}{2}\left(\frac{\partial u_i}{\partial x_j} + \frac{\partial u_j}{\partial x_i}\right) \quad i, j = x, y, z \tag{4.2}$$

Because the total strain distribution that we needed is generated by the total deformation ($\mathbf{u^0} + \mathbf{u}$) from the initial unstrained configuration to the equilibrium configuration, the total strain of the system is:

$$\varepsilon_{ij} = \varepsilon^e_{ij} + \varepsilon^0_{ij}\delta_{ij} \quad i, j = x, y, z \tag{4.3}$$

where $\varepsilon^0_{ij} = 0$ in the arm domain, and $\delta_{ij} = 1$ (or $\delta_{ij} = 0$) if $i = j$ ($i \neq j$). The elastic energy is:

$$W = \int \frac{1}{2}\Sigma_{ijkl} C_{ijkl}\varepsilon_{ij}\varepsilon_{kl} dV, \quad i, j, k, l = x, y, z \tag{4.4}$$

where $C_{ijkl}$ is the anisotropic elastic modulus tensor for the wurtzite structure, taken from the Landolt-Börnstein database [127].

The elastic energy minimization was implemented with the finite element method software COMSOL Multiphysics based on the virtual work principle [128]. The deformation and consequent strain distribution can be obtained for the equilibrium configu-

ration. To enhance the computational efficiency and accuracy, we calculated the strain distribution in the "core + one arm" region of the csTP according to its symmetry. Because interface matching was maintained during the calculation, the continuous deformation of the constituent materials was employed as a boundary condition at the interface ($\mathbf{u^A}\mid_{\mathbf{interface}}=\mathbf{u^S}\mid_{\mathbf{interface}}$). For the uniqueness of the solution, the core was assumed to be motionless ($\mathbf{u}=0$) as a constraint to prevent the translation or rotation of the structure. The other outer boundaries were specified as free surfaces due to the zero external force assumption for freestanding csTPs.

The strain induced modification of the lowest conduction band (CB) $V_{e\varepsilon}$ and the highest valence band (VB) $V_{h\varepsilon}$ can be evaluated using the strain-related Hamiltonian for a wurtzite semiconductor found in Ref. [95]. Considering the single-band calculation in the present study, we found that the band modification of the electron in question and the heavy hole states were:

$$V_{e\varepsilon}(\mathbf{r}_e) = a_{cz}\varepsilon_{zz} + a_{ct}(\varepsilon_{xx}+\varepsilon_{yy}) \tag{4.5}$$

$$V_{h\varepsilon}(\mathbf{r}_h) = (D_1+D_3)\varepsilon_{zz} + (D_2+D_4)(\varepsilon_{xx}+\varepsilon_{yy}) \tag{4.6}$$

where $a_{cz}$ and $a_{ct}$, respectively, are the deformation potentials of CB along the c-axis and transverse to the c-axis of wurtzite materials, $D_i(i=1\sim 4)$ are the deformation potentials of VB. For the wurtzite CdTe arms, the deformation potentials were derived from those of zinc-blende CdTe [129] with the quasi-cubic approximation [95]. The idea of this approximation is based on the similarity between the wurtzite structure along the [0001] direction and the zinc-blende structure along the [111] direction. For the wurtzite CdS shell, the deformation potentials were taken from Refs. [127, 130].

The strain induced band-edge shifts play a role in the potential modification of the heterostructure. This modification can be expressed as an extra potential term in the single-particle Schrödinger equation:

$$H_i\varphi_i(\mathbf{r}_i) \equiv \left\{-\frac{\hbar^2\triangle_i}{2m_i^*} + V_i(\mathbf{r}_i) + V_{i\varepsilon}(\mathbf{r}_i)\right\}\varphi_i(\mathbf{r}_i) = E_i\varphi_i(\mathbf{r}_i), \quad i=e,h, \tag{4.7}$$

where $\triangle$ is the Laplace operator, $V_i$ is the band offset of unstrained CB and VB, $\varphi_i$ is the envelope function of electrons and holes, and $E$ is the energy eigenvalue. $m^*$ is the isotropic effective mass assumed in our calculation. The numerical calculations were performed with the finite element method using the commercial software COMSOL Multiphysics.

In the II-VI semiconductors, the heavy and light hole states are not degenerate, and the heavy hole states have lower kinetic energy due to their larger effective mass. Because we are only interested in the low-energy excitons, the VB state mixing is not concerned in the present paper. In addition, there was good agreement between the low-energy excitons of CdTe/CdSe core-shell spherical NCs calculated with single-band and multi-band theory [101]. Thus the single-band approximation in the present study is valid as long as we focus our discussion on low-energy excitons.

The obtained envelope functions and energy of the low-energy electron and hole states are utilized to form pair states for the calculation of excitons. The calculation

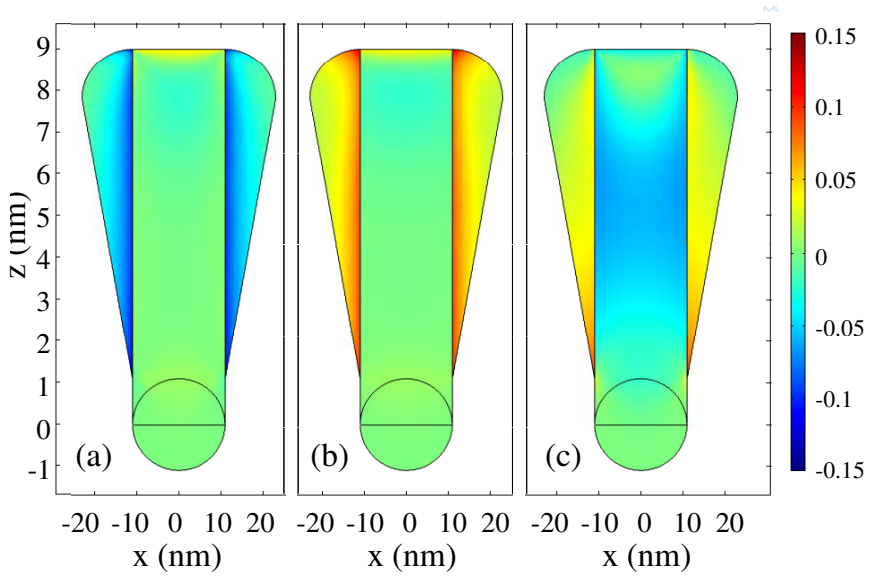


Figure 4.2: Cross-section of the calculated strain components (a) $\varepsilon_{xx}$, (b) $\varepsilon_{yy}$, and (c) $\varepsilon_{zz}$ in one arm of a csTP with $sh = 1.2$ nm [124].

of exciton states using configuration interaction approach followed the same procedures described in our previous study [53]. When the defect is not concerned, our present calculation method is suitable for the tetrapod-shaped core-shell nanocrystals with other materials in the strong confinement regime, which ensures the validity of configuration interaction approach and sufficient convergence in the numerical calculation.

## 4.3 Results and Discussion

Figure 4.2 shows the distribution of the calculated strain components $\varepsilon_{xx}$, $\varepsilon_{yy}$, and $\varepsilon_{zz}$ in an x-z cross-section of one branch of a csTP with $sh = 1.2$ nm. The CdTe arms are under compressive strain in all three directions due to the larger lattice constant. On the other hand, the CdS shells are under tensile strain $\varepsilon_{yy}$ and $\varepsilon_{zz}$, but the $\varepsilon_{xx}$ in the x-z cross-section is compressive due to Poisson's effect as shown in Fig. 4.2(a). The main features of the strain components in Fig. 4.2 agree with those of the InAs/InP core-shell nanowire [56], in which the core material has a larger lattice constant as the CdTe/CdS system in our calculation.

The compressive strain in the arms is dominated by its $\varepsilon_{zz}$ components. Because the z-direction component of the deformation potential of CdTe is negative for CB and positive for VB, the corresponding band edge energy shifts mainly have positive and negative values as shown in Fig. 4.3. This modification of VB is smaller than that of CB due to the smaller deformation potential in VB. With increasing $sh$, the strain decreases in the shell and increases in the arm, leading to larger band modification in the arm. As a result, the effective band gap of the arm is larger and the type-II nature of the heterostructure band structure is more pronounced.

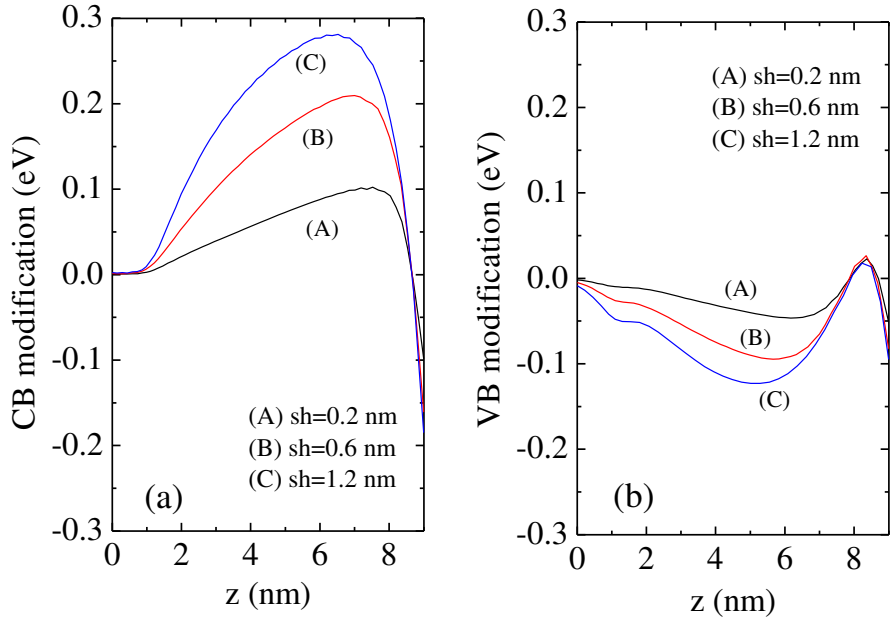


Figure 4.3: The strain induced band edge modification of (a) the CB and (b) the VB along the axial direction of the arms for csTPs ($D = 2.2$ nm) with different shell thicknesses [124].

To study the possible symmetries of single-particle states, we expressed the symmetric eigenfunctions by a linear combination of the wave function localized in each arm of bare tetrapod in the previous section. The eigenfunctions of $A_1$ and $T_2$ symmetry are given by Eqs.(3.13)$\sim$(3.16). The basis function $\phi_i$ is rotationally symmetric about the arm axis, so their angular momentum $l$ around the arm axis is equal to 0.

However, in the high energy range, there are also such functions with non-zero angular momentum. In that case, there are two basis functions rotating clockwise and counterclockwise on each arm. The total eight functions constitute the eigenfunctions of the tetrapods. Their symmetries can be found by the conventional reduction procedure [117].

For $l = 1$, the two basis functions on each arm have the angular ($\theta$) dependence around the arm axis like $e^{\pm i\theta}$, or we may use their linear combination, $cos\theta$ and $sin\theta$. Then, we examine their transformation property when symmetry operation R of point group $T_d$, which are listed in Table 4.1, are applied. Since the number of invariant arms $N_R$ is equal to zero for $IC_4$ and $C_2$, they are irrelevant to the following calculation.

For the reflection by the diagonal mirror plane, $\sigma_d$, we may take the origin of $\theta$ on the mirror plane without loss of generality. Then the two functions are transformed as

$$\sigma_d \begin{pmatrix} cos\theta \\ sin\theta \end{pmatrix} = \begin{pmatrix} 1 & 0 \\ 0 & -1 \end{pmatrix} \begin{pmatrix} cos\theta \\ sin\theta \end{pmatrix} \tag{4.8}$$

so their character $\chi_1(\sigma_d)$, which is given by the sum of the diagonal elements of the above transformation matrix, is vanishing. On the other hand, when we apply the three-fold

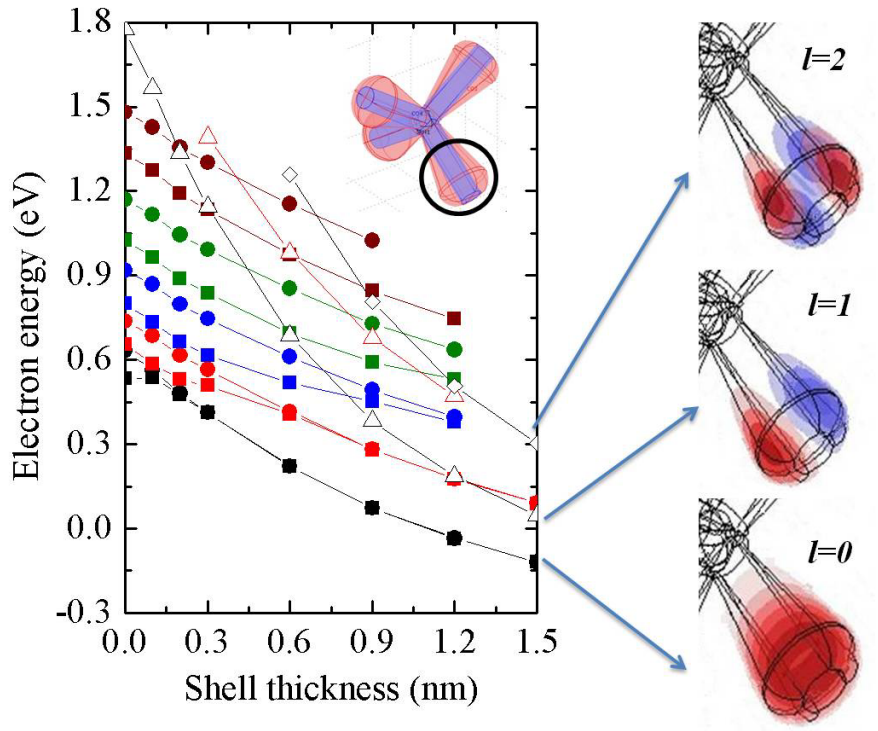


Figure 4.4: (a) The electron states energies as a function of the shell thickness. The origin of the energy is taken at the conduction band bottom of the central CdTe core. Square and circle denote the $A_1$ and $T_2$ states, respectively. Triangle denotes the non-zero $l$ states. (b)The wave function of electron states with various $l$ on one arm of the tetrapod.

Table 4.1: Symmetry of the electron state in a core-shell tetrapod. The character of electron state as well as the symmetry obtained by the reduction procedure were shown.

| $T_d$ | $R$ | $E$ | $6IC_4$ | $3C_2$ | $6\sigma_d$ | $8C_3$ | | *symmetry* |
|---|---|---|---|---|---|---|---|---|
| | $N_R$ | 4 | 0 | 0 | 2 | 1 | | |
| $l=0$ | $\chi_1(R)$ | 1 | – | – | 1 | 1 | | |
| | $\chi(R)$ | 4 | 0 | 0 | 2 | 1 | $\rightarrow$ | $A_1+T_2$ |
| $l=1$ | $\chi_1(R)$ | 2 | - | - | 0 | -1 | | |
| | $\chi(R)$ | 8 | 0 | 0 | 0 | -1 | $\rightarrow$ | $E+T_1+T_2$ |
| $l=2$ | $\chi_1(R)$ | 2 | - | - | 0 | -1 | | |
| | $\chi(R)$ | 8 | 0 | 0 | 0 | -1 | $\rightarrow$ | $E+T_1+T_2$ |
| $l=3$ | $\chi_1(R)$ | 2 | - | - | 0 | 2 | | |
| | $\chi(R)$ | 8 | 0 | 0 | 0 | 2 | $\rightarrow$ | $A_1+A_2+T_1+T_2$ |

rotation $C_3$, they are transformed as

$$C_3 \begin{pmatrix} cos\theta \\ sin\theta \end{pmatrix} = \begin{pmatrix} -\frac{1}{2} & -\frac{\sqrt{3}}{2} \\ \frac{\sqrt{3}}{2} & -\frac{1}{2} \end{pmatrix} \begin{pmatrix} cos\theta \\ sin\theta \end{pmatrix} \tag{4.9}$$

so $\chi_1(C_3) = -1$. Then, from the total character $\chi(R) \equiv \chi_1(R)N_R$, we obtain the symmetries of eigenfunctions by the standard reduction procedure [117]. As the results, we find that there are $E$, $T_1$ and $T_2$ modes.

Similarly, in the case of $l = 2$, we have the following relations:

$$\sigma_d \begin{pmatrix} cos2\theta \\ sin2\theta \end{pmatrix} = \begin{pmatrix} 1 & 0 \\ 0 & -1 \end{pmatrix} \begin{pmatrix} cos2\theta \\ sin2\theta \end{pmatrix} \tag{4.10}$$

$$C_3 \begin{pmatrix} cos2\theta \\ sin2\theta \end{pmatrix} = \begin{pmatrix} -\frac{1}{2} & \frac{\sqrt{3}}{2} \\ -\frac{\sqrt{3}}{2} & -\frac{1}{2} \end{pmatrix} \begin{pmatrix} cos2\theta \\ sin2\theta \end{pmatrix} \tag{4.11}$$

and again there are $E$, $T_1$ and $T_2$ modes. For $l = 3$, similar consideration leads to the presence of $A_1$, $A_2$, $T_1$ and $T_2$ modes. These qualitative conclusions are confirmed by numerical calculation in the following.

Figure 4.4(a) shows the calculated electron energy as a function of the shell thickness $t$. As a general feature, the electron energy decreases with increasing $t$ because the confinement volume (central core + arms + shells) is larger, which reduces the electron kinetic energy. The electron confinement potential of the shell is smaller than the core and arms as shown in Fig. 4.1(d), which also reduces the electron energy.

Another feature of Fig. 4.4(a) is the presence of non-zero $l$ states for large $t$. For $t = 1.2nm$, for example, three such states are shown by the triangle symbol in the figure. $l$ is equal to one for the lowest state among the three. Its wave function is shown in Fig. 4.4(b). For the second lowest one among the three states with non-zero angular momentum, $l$ is also equal to one. The difference between the two $l = 1$ state is that the latter wave function has a node along the arm axis, while the former one does not. These non-zero $l$ states have relatively high energies for smaller $t$. Although it is not shown in Fig. 4.4, we also found $l = 3$ states in the higher energy range. On the other hand, the difference among several $A_1$ or $T_2$ states are mainly the number of nodes along the arm axis.

In a spherical type-II structure, we only need to be concerned with the carrier wave functions along the radial direction. When the shell thickness is infinite, the electrons and holes can be considered completely spatially separated. For real core-shell type-II spherical NCs, the finiteness of the shell thickness leads to a non-zero overlap of the confined electron and hole wave functions. Hence, a sufficiently large shell thickness is necessary for efficient carrier separation.

The situation in a csTP with tetrahedral symmetry is more complex than in a spherical heterostructure. Figure 4.5 shows the effect of strain on the wave functions of the lowest electron and hole states, which mainly determine the nature of the lowest exciton state. The wave function of the lowest electron and hole states of csTPs have $A_1$ symmetry

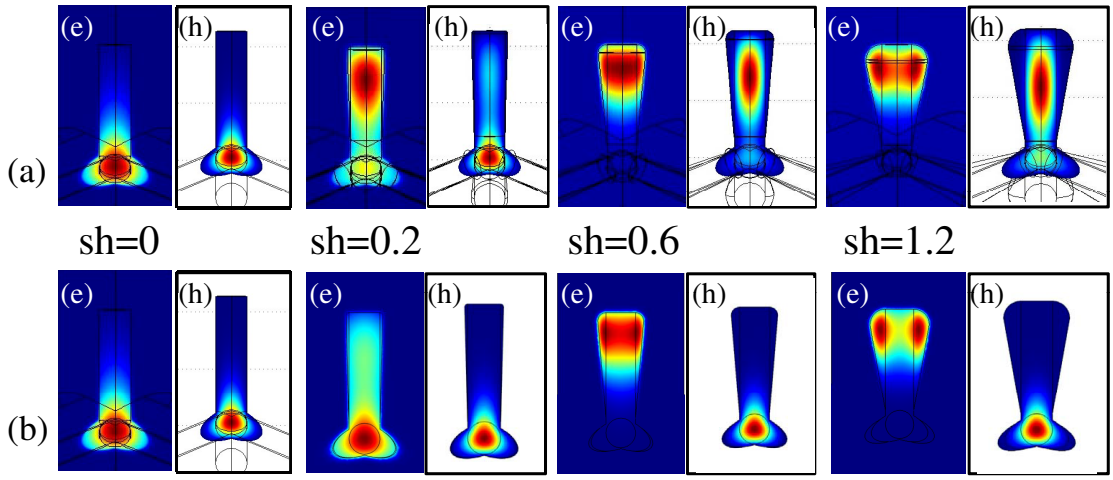


Figure 4.5: Cross-section of the wave function of the lowest electron and hole states for csTPs with various shell thicknesses. Wave functions of csTPs (a) without and (b) with the strain effect are plotted for comparison. The labels (e) and (h) denote the wave function of electron and hole states, respectively [124].

and are localized in the core region for a bare tetrapod ($sh = 0$). As $sh$ increases, the larger volume in the "CdTe arm + CdS shell" region attracts both the electrons and holes. The electrons are eventually distributed in the CdS shells for a sufficiently large $sh$, because of the smaller potential energy there. We notice that as the shell thickness increases to 1.2 nm, the electrons in the shell and the holes in the arm are still not completely separated.

The inclusion of strain leads to a more pronounced type-II band alignment in the CdTe/CdS csTPs. This phenomenon is consistent with the results for the core-shell type-II spherical NCs in which the core material has a larger lattice constant than the shell [58, 131, 132]. But we notice that the type-II nature of the strained csTPs induces the carrier separation more effectively. As shown in Fig. 4.5(b), the strain induced band modification prevents carrier delocalization out of the core region. As $sh$ increases, electrons with larger kinetic energy can be redistributed in the shell with smaller potential energy, but the holes remain in the core region. The electrons and holes can be considered completely separated according to their localization in the nonadjacent regions.

With the results of single particle states, we can discuss the exciton states in csTPs. For all the $sh$ values in the present study, the lowest spin-singlet exciton has $A_1$ symmetry (optically active), which mainly consists of the lowest electron-hole pair state. As $sh$ increased, a red shift in the exciton energy was observed for the type-II structure as a result of the decreasing confinement. Moreover, the oscillator strength of the lowest and the second lowest $A_1$ spin-singlet exciton quickly decreased due to the carrier separation as shown in Fig. 4.6. The oscillator strength of the lowest exciton decreased by 99% when the shell thickness increased to 0.6 nm, reflecting the high efficiency of carrier separation in csTPs. With a sufficiently large shell thickness, the luminescence of csTPs with perfect symmetry may be very weak. Therefore, we suppose that there are other contributions to the luminescence observed in the experiment, for example csTPs with broken symmetry,

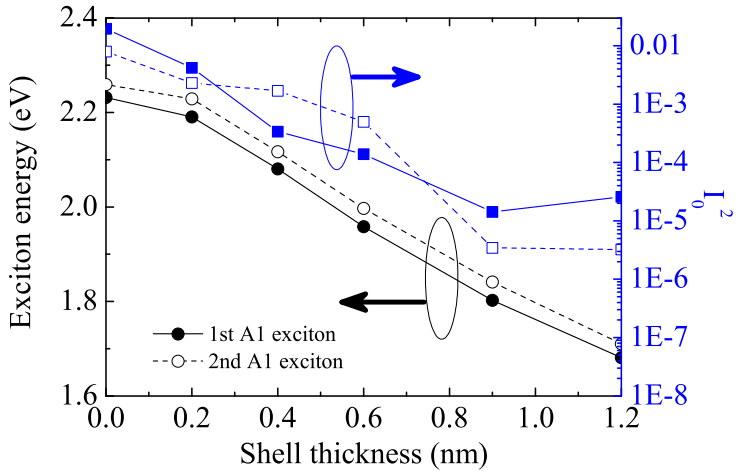


Figure 4.6: Variation in the energy (circles) and the square of the overlap integral (squares) of the lowest (solid line) and the second lowest (dashed line) $A_1$ exciton as a function of shell thickness [124].

which we discuss below.

The effect of dimensions and strain on the energy of the lowest spin-singlet exciton is shown in Fig. 4.7 (a). The inclusion of strain induces a small blue shift in the lowest exciton energy. This can be explained by the penetration of carrier wave functions into the CdTe arms with an enhanced band gap modified by the strain. Meanwhile, the increasing $sh$ leads to a red shift with a magnitude larger than the influence of the strain. This is consistent with the calculation results for spherical core-shell type-II NCs [130, 132]. For csTPs with a large $D$, the energy of the lowest exciton is less tunable by $sh$, which is consistent with the results for CdTe/CdSe spherical dots reported in Ref. [101]. On the other hand, the strain has less effect on the lowest exciton energy because there is less strain in an arm with a larger $D$.

Figure 4.7 (b) compares calculation results and a previously reported experimental observation [57]. To concentrate on the effect of shell thickness, the experimental results were shifted to align them with the calculation result at $sh = 0$. When the large inhomogeneous broadening in the experimental results is taken into consideration, the $sh$ dependence of the calculated exciton energy agrees well with the photoluminescence data.

In an actual csTP specimen, broken symmetry may influence the carrier distribution and consequently the emission properties. Because it is impossible to study all kinds of randomness, here we analyzed the combination of parameters $D$ and $sh$, which have a dominant influence on the optical properties [53]. We studied the change induced by two kinds of modifications to csTP with $D = 2.2$ nm and $sh = 0.9$ nm, and tried to identify the essential features of symmetry breaking in a qualitative manner: For the first case, we modified one arm with a larger diameter $D'$ ($D' > D$) or a larger shell thickness $sh'$ ($sh' > sh$) for the csTP; for the second case, we modified the same arm or two different arms of the csTP with a larger diameter $D'$ and a larger shell thickness $sh'$.

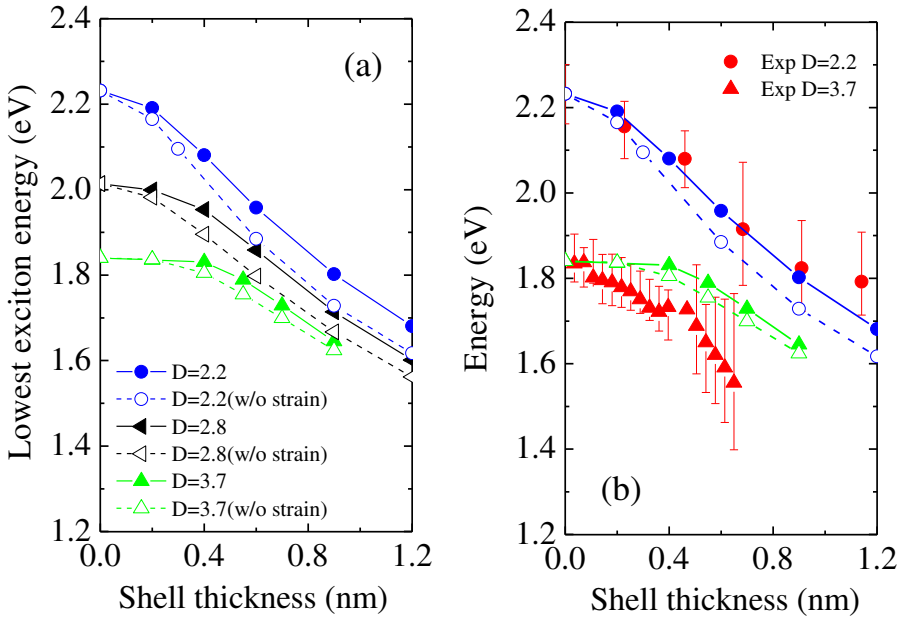


Figure 4.7: (a) The shell thickness dependence of the lowest spin-singlet exciton energy of strained csTPs with different $D$ values. The corresponding data for unstrained csTPs are also plotted for comparison. (b) Comparison of the calculated lowest spin-singlet exciton energy with the experimental photoluminescence peak energy of strained csTPs. The data for $D = 2.2$ nm and $D = 3.7$ nm are denoted by circles and triangles respectively. The experimental results were shifted to align them with the calculated exciton energy at $sh = 0$. The error bar indicates the full width at half maximum (FWHM) of the observed luminescence peak [124].

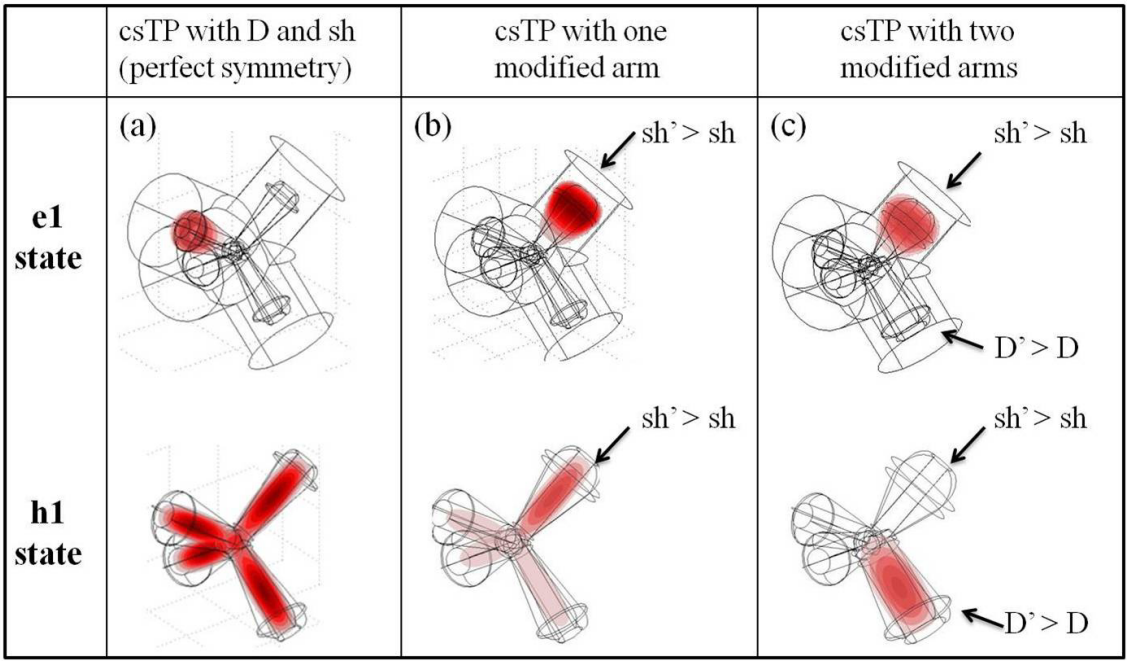


Figure 4.8: The wave function of the lowest electron and hole state for (a) csTP with perfect symmetry (arm width D, shell thickness sh), (b) csTP with one modified arm ( with larger shell thickness sh' ), (c) csTP with two modified arms (with larger shell thickness sh' and larger arm width D' , respectively.

As shown in Fig. 4.8(b), with larger $D'$ or $sh'$ in only one arm, the low-energy electron and hole state tend to locate in the modified arm due to the increased confinement volume, which is consistent with the results described in Ref. [50]. We revealed that $D'$ and $sh'$ mainly influence the hole and electron distribution, respectively. On the basis of this result, we can design the hole and electron distribution by manipulating the parameters of each isolated branch of a csTP.

As shown in Fig. 4.8(c), with the simultaneous modification of $D'$ and $sh'$ in two different arms, we found that the low energy electron and hole states were localized on the corresponding different arms. This kind of randomness-induced carrier separation is unique for branched core-shell NCs, and cannot be found in core-shell spherical or rod systems. With the simultaneous modification of $D'$ and $sh'$ on the same arm, the increased wave function overlap between low-energy electrons and holes is assumed to contribute to the luminescence in the experiment.

Figure 4.9 shows the absorption spectra of $sh = 0.9$ nm csTP with and without perfect symmetry. To capture any small changes of the spectra, a small full width at half maximum (FWHM) of 10 meV was assumed. With larger $D'$ or $sh'$, the intensity of the main peak decreased compared with that of the csTP with perfect symmetry, and a new peak occurs on the longer wavelength side corresponding to the absorption in the modified arm. The new peak for $sh' = 1.2$ nm had nearly the same wavelength as that of the absorption peak for csTP with $sh = 1.2$ nm. Since the low energy electron and hole wave functions for large sh are localized in the "arm + shell" regions, their absorption

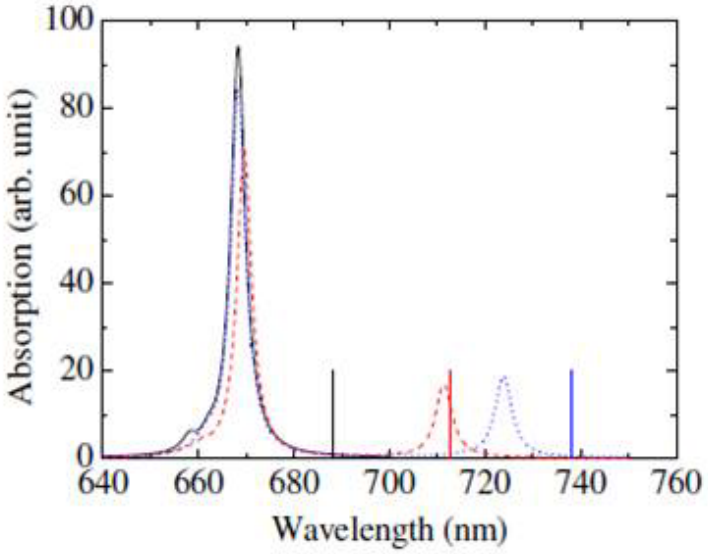


Figure 4.9: Comparison of absorption spectra for $sh = 0.9$ nm csTP with perfectly tetrahedral symmetry (solid line), and broken symmetry including $D = 2.8$ nm for one arm (dash line), $sh = 1.2$ nm for one arm (dot line). The straight lines (from left to right) denote the wavelength of the lowest singlet exciton for these three models, respectively. The FWHM of the spectra is assumed to be 10 meV.

spectra are well represented by the sum of spectra of individual "arm + shell" regions. So, the absorption spectrum of the broken-symmetry structure in the above case can be approximated by a weighted average of spectra of $sh = 0.9$ nm and $sh = 1.2$ nm with a ratio of 3:1. Thus, as far as both the electron and hole are located in the same arm, the broken symmetry can be regarded as a part of inhomogeneous broadening.

It is worth noting that the larger $D'$ led to smaller energy spacing between hole levels. The energy difference between the lowest exciton and higher exciton with relatively larger oscillator strength is only 4 meV. Therefore the room temperature thermal energy (26 meV) may mix the population of these excitons, and the luminescence from the lowest exciton can be expected. This feature was not found for arm of csTP with larger $sh'$. Thus, the non-uniformity of $D$ contributed to the luminescence.

## 4.4 Conclusion

The exciton states of strained CdTe/CdS core-shell tetrapod-shaped NCs were investigated theoretically. The inclusion of the strain effect promotes the type-II nature of the band structure in CdTe/CdS csTPs. When compared with type-II spherical NCs, tetrahedral symmetry combined with the strain effect leads to more efficient carrier separation by confining the low-energy electrons and holes in nonadjacent regions. The strain effect induces a blue shift of the lowest spin-singlet exciton state. Increasing shell thickness leads to a red shift with a larger magnitude than the influence of strain, which is consistent with previous results for spherical type-II core-shell NCs. For csTPs with a larger $D$, both

*sh* and the strain have less influence on the energy of the lowest exciton. The shell thickness dependence of the calculated exciton energy agreed well with available experimental data. From a practical point of view, type II CdTe/CdS csTPs with charge separation are interesting for photovoltaic applications in devices with an active layer based on nanoparticles, wherein the charge separation occurs within the nanoparticle [133]. So, the present calculation provides an opportunity to predict electronic properties and improve the effectiveness of charge separation.

The study of csTPs with broken symmetry revealed that electrons and holes can be confined in the same or different branches by manipulating the randomness. The randomness induced carrier separation into different branches of a csTP is unique for a branched core-shell heterostructure. When the electrons and holes are localized in the same branch, we supposed the spatial direct transition in the branch contribute to the luminescence observed in the experiment. Tetrapods with broken symmetry provide evidence for the view that type II csTPs behave like four weakly connected quantum dots (each branch of the tetrapod) with the possibility of an electron remaining in a single dot for a long time. This might find interesting applications in nanoelectronics (e.g. as memory devices or elements for quantum computing).

# Chapter 5:

# Electronic structure of quantum double rings in the lateral electric field

## 5.1 Quantum double rings

Self-assembled GaAs quantum double rings (QDRs) were fabricated for the first time by Mano et al. [63] by means of droplet epitaxy [61, 62]. Micro photoluminescence (PL) spectra and electronic structures of GaAs QDRs covered with an AlGaAs barrier layer were reported in Refs. [63] and [64]. Because the QDR has a nearly perfect circular symmetry, its electronic state can be characterized by radial quantum number $N$ and azimuthal quantum number $l$. Some previous theoretical studies on the QDR used this circular symmetry [73]. This property was also used for the theoretical study of its electronic states in a magnetic field perpendicular to the rings [74–76], which is relevant to the exciton Aharonov-Bohm effect [77]. Recently a relatively large Stark shift up to 4 meV was observed for GaAs QDRs due to their large lateral sizes [83], which can be used for frequency tuning. Figure 5.1 shows their AFM (atomic force microscope) image. In previous experiment of the Stark shift of GaAs QDRs [83], however, the external electric field broke the circular symmetry of the geometry because it was applied parallel to the sample surface, that is, parallel to the double rings. Thus we have to use another numerical method that does not assume circular symmetry to analyze the energy levels of the electron and hole in the QDR.

In this chapter, we report such calculations on the energy levels and distribution of the probability density of the electron and heavy hole in the GaAs QDR, and the optical transition oscillator strength by the three-dimensional finite element method. We present the Stark shift of the lowest 14 energy levels for both electron and heavy hole in the lateral electric field up to 2 kV/cm. We will show that an energy shift of 4 meV is brought about by an applied electric field of 0.7 kV/cm for the ground state transition. But considering its oscillator strength decreases rapidly with increasing electric field, so the observed shifted emission peak may not be explained by the Stark shift of the ground-state exciton emission alone. We presume that higher energy levels are also relevant whose emissions become allowed due to symmetry breaking by the applied electric field and/or intense photo excitation of carriers.

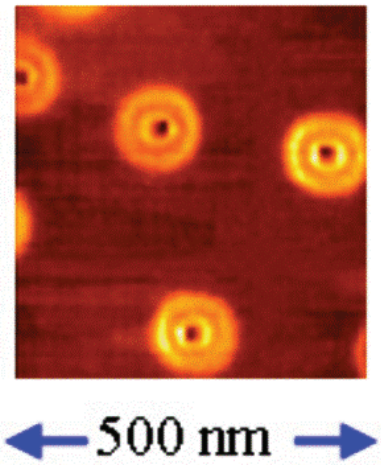


Figure 5.1: AFM image of GaAs QDRs [134].

## 5.2 Model of quantum double rings in the uniform electric field

We calculated the energy levels of the electron and heavy hole confined in the QDR by the finite element method with the single-band effective-mass approximation. We used a three-dimensional model of a specimen that was obtained by measuring its shape with AFM. Figure 5.2 shows one half of the vertical cross section of the double ring structure for the GaAs QDR embedded in the $Al_{0.3}Ga_{0.7}As$ barrier layer reported in Ref. [63]. The GaAs QDR is denoted by dark gray and the $Al_{0.3}Ga_{0.7}As$ substrate and barrier layer are denoted by light gray. The QDR is circularly symmetric about the $z$ axis. The amplitude of the wave functions out of the volume denoted by the light gray color was assumed to be vanishing, because we are interested in only those states that are well confined in the GaAs QDR.

The conduction band of GaAs has an s-orbital character and is non-degenerate, while its valence band has a p-orbital character and is doubly degenerate on the $\Gamma$ point of the first Brillouin zone [19]. The degeneracy is lifted by the introduction of mesoscopic confinement because of the difference of the effective mass between the two bands, so appreciably separate heavy- and light-hole bands are formed [20]. In the energy range of the analysis given below, only the heavy hole is relevant. So, we also used the single-band effective-mass approximation for the valence band.

The effective mass of the electron and heavy hole in the two materials and their band offsets are listed in Table 5.1, which are the same values used in a previous calculation without an applied electric field [63]. We assumed an isotropic effective mass for the heavy hole following previous calculations [63, 74, 75], although anisotropy of the effective mass of the heavy hole is brought about by the quantum confinement [19]. According to Ref. [19], the heavy hole effective mass of GaAs is 0.11 (0.5) times electron mass in the direction parallel (perpendicular) to the quantum well. However, the change in the heavy hole energy brought about by the anisotropy is rather small for low energy states with

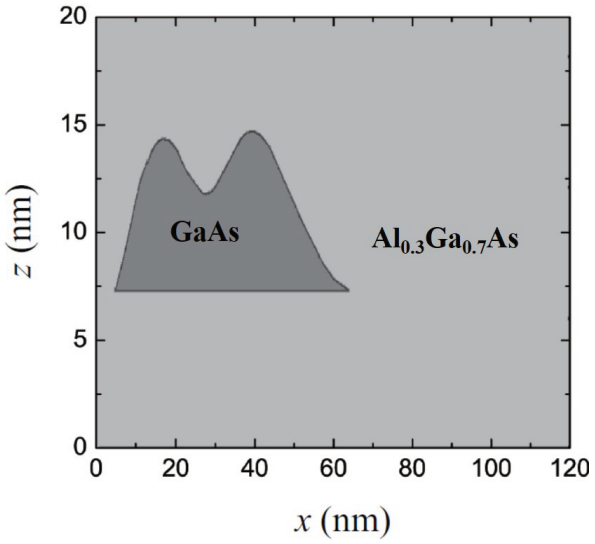


Figure 5.2: One half of the vertical cross section of the double ring structure of GaAs assumed in the calculation. The GaAs QDR is denoted by dark gray and the $Al_{0.3}Ga_{0.7}As$ substrate and barrier layer by light gray. The QDR is symmetric about the $z$ axis. The static electric field is applied in the positive $x$ direction.

small angular momenta as we will see in the next section, so we also used the isotropic effective mass for the heavy hole. The one-particle Schrödinger equation with external static electric field was solved by the finite element method with the commercial software COMSOL Multiphysics. The discretization mesh size of the finite-element calculation was decreased sufficiently to obtain converged results.

Table 5.1: Parameters used in the calculation. $m_0$ is electron mass [134].

| Quantity | Unit | $GaAs$ | $Al_{0.3}Ga_{0.7}As$ |
|---|---|---|---|
| Electron effective mass [135] | $m_0$ | 0.067 | 0.093 |
| Heavy hole effective mass [135] | $m_0$ | 0.51 | 0.57 |
| Conduction band offset [136] | $meV$ | | 262 |
| Valence band offset [136] | $meV$ | | 195 |

## 5.3 Results and Discussion

Figure 5.3 shows the energy levels as functions of the external electric field $E$ applied in the lateral ($x$) direction. The lowest 14 levels are given for the electron in Fig. 5.3(a) and for the heavy hole in Fig. 5.3(b). The origin of the vertical axis of Fig. 5.3(a) is the conduction-band bottom of the $Al_{0.3}Ga_{0.7}As$ barrier layer and that of Fig. 5.3(b) is the valence-band top of the $Al_{0.3}Ga_{0.7}As$ layer.

First, let us check the energy levels without the electric field. In this case, the QDR configuration has circular symmetry so that all electronic states are characterized by the

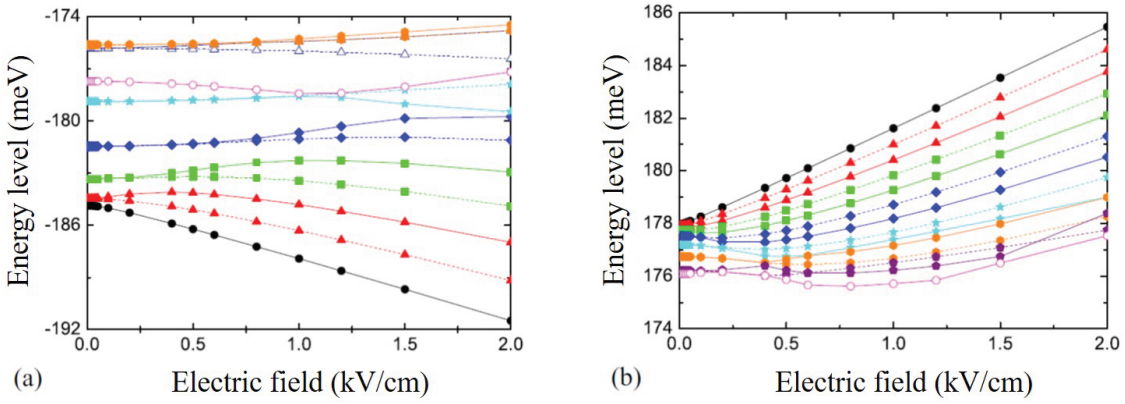


Figure 5.3: Energy levels of the quantum-confined (a) electron and (b) heavy hole in the GaAs QDR as functions of the external electric field in the lateral direction. The origin of the vertical axis of Fig. 5.3(a) is the conduction band bottom of the AlGaAs barrier layer and that of Fig. 5.3(b) is the valence-band top of the AlGaAs layer. $l = 0$ (s), 1 (p), 2 (d), 3 (f), 4 (g), 5, and 6 states are denoted by circle, triangle, square, diamond, star, hexagon, and pentagon, respectively. $N = 1$ states are denoted by solid symbols and $N = 2$ states are denoted by open symbols. States with even and odd parities about the x axis are denoted by solid line and dashed line, respectively.

principal quantum number $N$ and the azimuthal quantum number (angular momentum) $l$. We denote the states with $l$= 0, 1, 2, 3, and 4 by s, p, d, f, and g, respectively. We should note that the s states are not degenerate but all other states are doubly degenerate, since there are two independent wave functions proportional to $\exp(il\phi)$ and $\exp(-il\phi)$, respectively, where $\phi$ is the azimuthal angle.

The energy levels for $E = 0$ were obtained in the previous calculation by the exact diagonalization of the effective-mass Hamiltonian by means of the Fourier-Bessel expansion of the wave function assuming structural circular symmetry [64]. When we compare the energy levels for $E = 0$ calculated by the present method with the previous results [63], they agree with each other quite well. In addition, the transition energy of the ground state, which is attributed to the 1s hole to 1s electron transition, is 1.613 eV and the energy difference to the first excited state, which is attributed to the 2s hole to 2s electron transition, is 9.0 meV in their calculation. These values show reasonable agreement with reported experimental results, that is, 1.68 eV for the former and 8.5 meV for the latter [63]. When we use the anisotropic effective mass for the heavy hole described in the previous section, we obtain 1.617 eV for the ground state energy and 10.4 meV for the energy difference to the first excited state. Since the changes induced by the effective-mass anisotropy are relatively small, we assumed the isotropic effective mass in the rest of the calculations.

Next, let us examine the probability density distribution of the electron and heavy hole. Figure 5.4 shows its vertical cross section for the 1s, 2s, and 3s states of the confined electron and heavy hole. For both particles, the 1s and 2s states are localized in the outer and inner rings, respectively, which is consistent with the previous calculation [63].

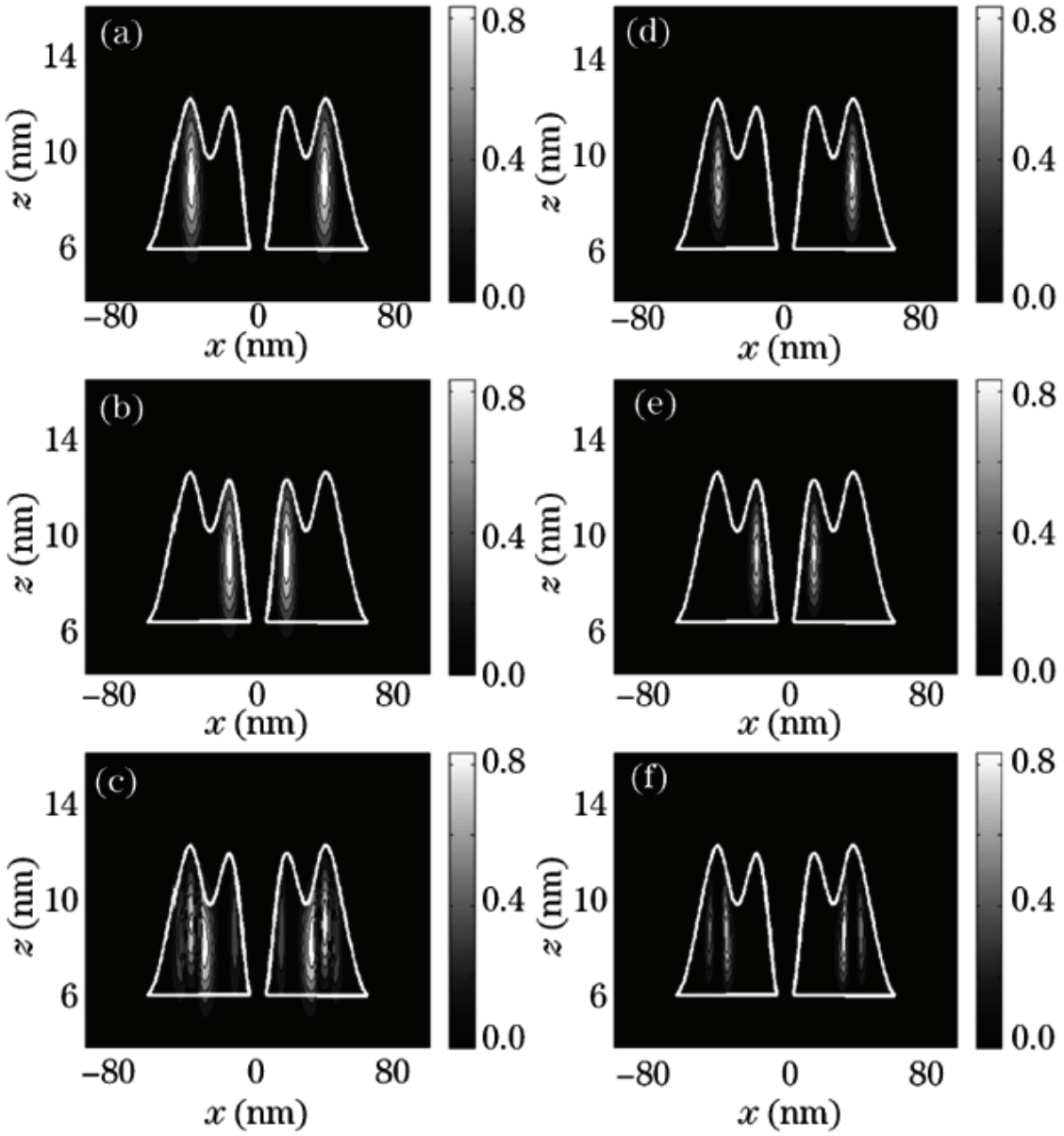


Figure 5.4: Distribution of the probability density in the QDR. (a) 1s state, (b) 2s state, and (c) 3s state of the electron and (d) 1s state, (e) 2s state, and (f) 3s state of the heavy hole [134].

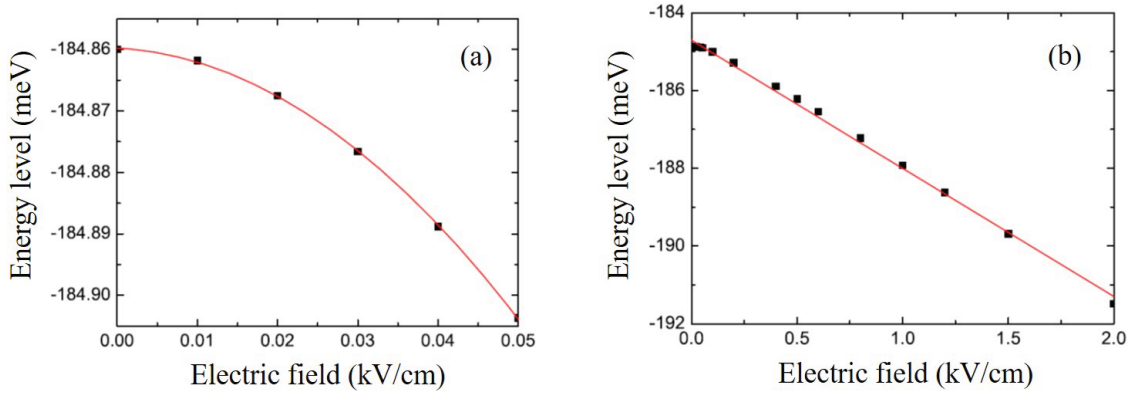


Figure 5.5: The 1s electron energy as a function of the lateral electric field. Energy shift (a) for relatively small electric fields with a quadratic-fitting curve and (b) for relatively large electric fields with a linear-fitting curve.

We should note, however, that this feature may not be universal but may depend on the distance between the inner and outer rings and their widths as was shown by Climente et al. [73]. As for 3s states, their wave functions apparently have nodes.

Now let us proceed to the case of non-zero electric fields. Figure 5.5 shows the 1s electron energy as a function of the lateral electric field. The origin of the vertical axis is the conduction band bottom of the $Al_{0.3}Ga_{0.7}As$ barrier layer as before. Black dots denote the numerical results and solid lines are linear- and quadratic-fitting curves. It is clearly seen that the energy shift shows a quadratic change for relatively small electric fields up to 0.05 kV/cm and then shows a linear change for relatively large electric fields up to 2.0 kV/cm. The transition from quadratic to linear behavior with increasing amplitude of the electric field is consistent with the perturbation theory. When applied electric field is small, its influence on the energy of the non-degenerate lowest electron state (1s) can be described with non-degenerate perturbation theory. Because of the odd symmetry of electric dipole in the spatial coordinates, the first order perturbation term is zero. The second order perturbation of energy dominates, that leads to the quadratic dependence of electric field.

As we mentioned, the electric field in the $x$ direction broke the cylindrical symmetry of the QDR geometry. Therefore, the $l$ is not a good quantum number for non-zero $E$. But the wave functions of the electrons and holes have even or odd symmetry about the direction of the electric field ($x$). The matrix element of electric dipole $\langle \psi_j | eEx | \psi_i \rangle$ between the states $i$ and $j$ are nonzero when they have the same symmetry about the $x$ direction. (Here $e$ denotes the elementary charge.) Consequently, these two states will couple with each other and their wave function will mix. Since we have the 1p state about 0.5 meV above the 1s state, the coupling between the 1s and 1p state is not negligible for large electric field. The influence of electric field on this system must be described with degenerate perturbation theory. The linear dependence on electric field occurred, due to the nonzero first order perturbation term between the 1s and 1p state.

Figure 5.5 shows that about a 2 meV shift of the 1s state is attained by application

of the electric field of about 0.7 kV/cm. Since the behavior of the 1s heavy hole state is similar as shown below, we conclude that we can expect the 4 meV Stark shift of the GaAs emission peak energy found in previous experiment [83] with an electric field of the order of 0.7 kV/cm. This value of the Stark shift seems reasonable, since we obtain a Stark shift of 5.6 meV if we assume a polarization of electron and hole along the diameter of the outer ring that is approximately 80 nm. However we should note that the Coulomb binding energy of the exciton may depend on the charge polarization caused by the applied electric field. We evaluated the Coulomb attraction energy between the electron and heavy hole with a dielectric constant of 12.53 for GaAs QDR [137]. By assuming the average distance between the electron and heavy hole equal to the radius of QDR (60 nm), the Coulomb energy of 1.9 meV was obtained. Because the Coulomb energy is much smaller than the kinetic energy of electrons and holes, it was neglected in the following discussion. In addition, the oscillator strength of the ground-state emission decreases rapidly with increasing electric field due to charge separation. So, the shifted emission peak observed in the recent experiment may not be explained by the Stark shift of the ground-state transition alone.

Now, let us go back to Fig. 5.3. A clear transition from quadratic to linear behavior is also found for the 1s heavy hole state. On the other hand, each degenerate energy level with $l \neq 0$ is split into two by the application of the electric field in the lateral ($x$) direction. Their wave functions are symmetric or anti-symmetric about the $x$ axis. The symmetric and anti-symmetric states are denoted by solid and dashed lines, respectively. In contrast to the case of the 1s electron (heavy hole) state, for which all other energy levels are located above (below) it, the energy shift as a function of the applied electric field is not necessarily monotonic for the rest of the energy levels because of the repulsion between levels with the same symmetry. This feature of our results is consistent with a previous calculation for single rings [138]. Another feature of Fig. 5.3 is the smaller spacing of energy levels for the heavy hole due to its larger effective mass than the electron, which results in the faster transition from quadratic to linear behavior.

When two energy levels with the same parity come close and cross each other with the increasing applied electric field, an anti-crossing should take place. This behavior can be seen for the 1g and 2s electron states in Fig. 5.3(a), for example. Figure 5.6 shows a magnified view of Fig. 5.3(a) around $E = 1.08$ kV/cm and energy level of -178.5 meV and top views of five relevant wave functions. With increasing $E$, the 2s state goes down whereas the split 1g states go up. Because the 2s state has even parity about the $x$ axis, one of the 1g states with even parity repels the 2s state and shows the anti-crossing behavior. Then, as revealed by the distribution of the wave functions, the characters of the two branches are exchanged with each other. A similar behavior was found for single rings [138].

An interesting behavior of the probability density distribution is accompanied by the non-monotonic variation of energy levels with the applied electric field as shown in Fig. 5.7. For the 1s electron, its polarization is normal as shown in the left part of the figure. But for the 1p electron with even parity, which is shown in the right part, the electron is polarized in the opposite direction firstly and then in the normal direction when the

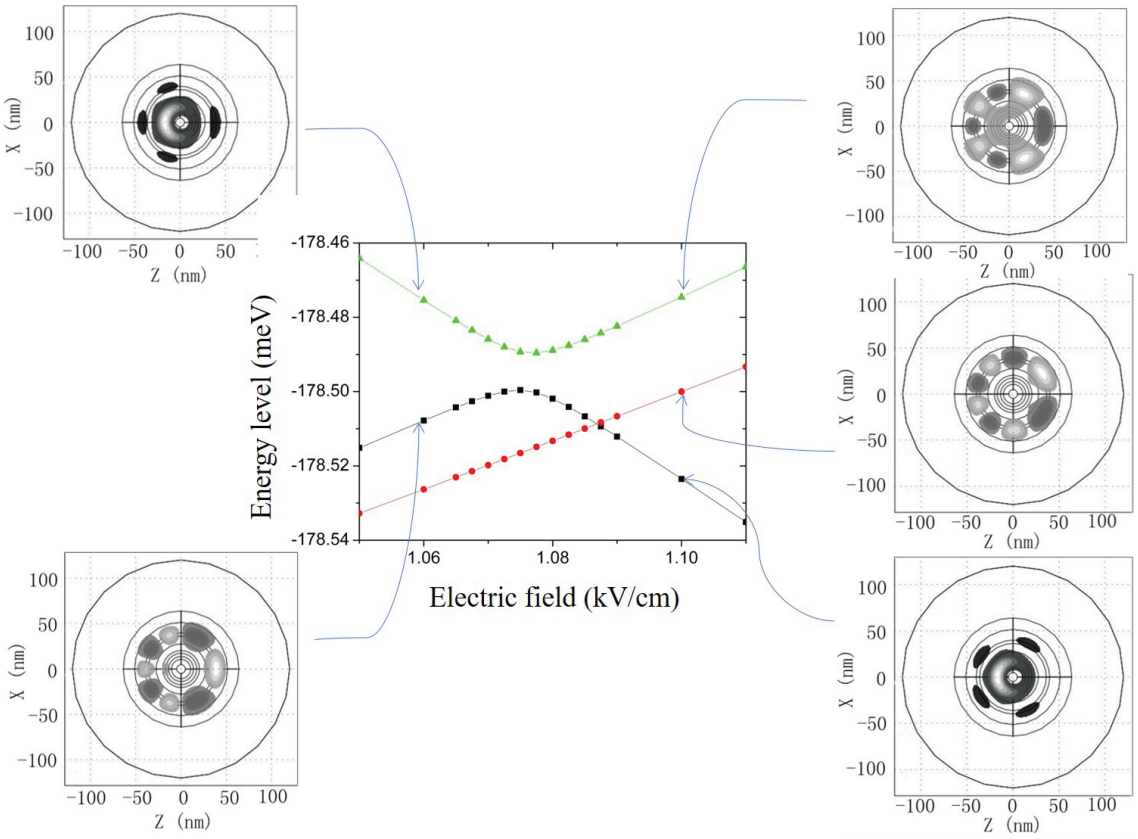


Figure 5.6: Anti-crossing of the 2s and 1g electron states and the distribution of the wave functions of the relevant states.

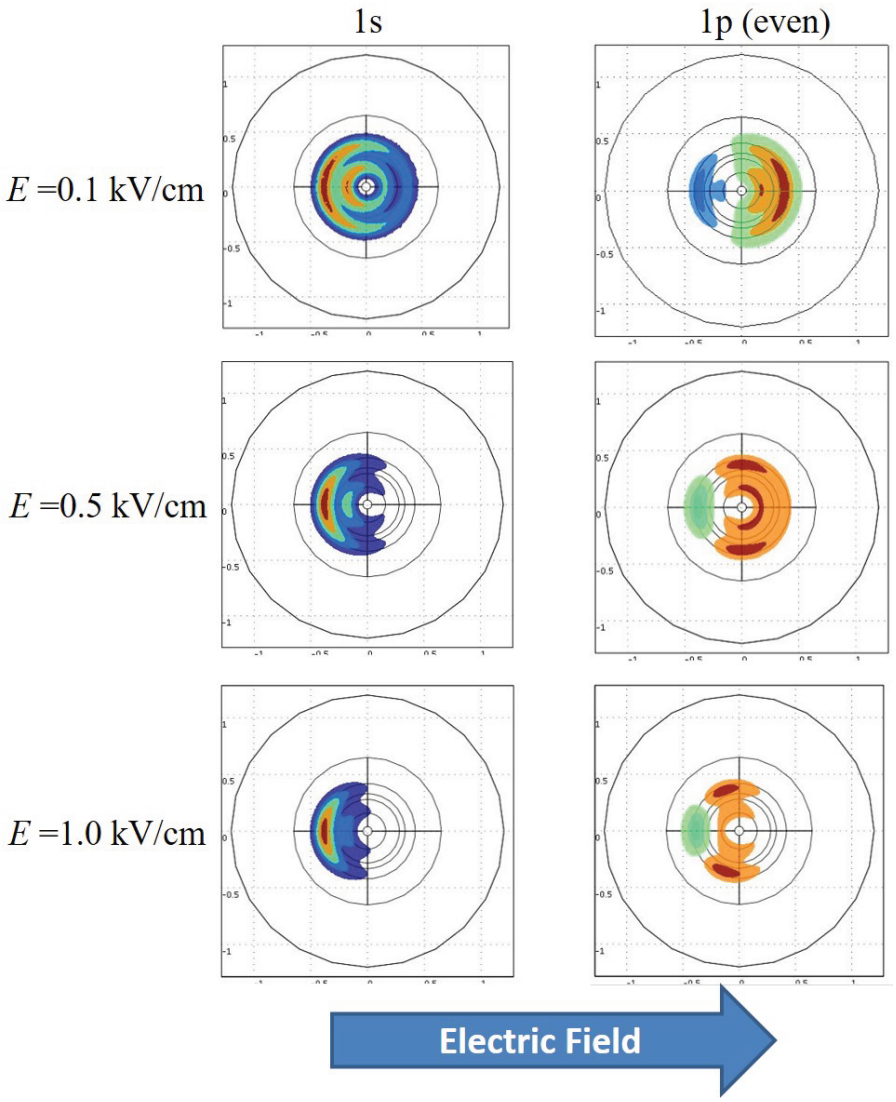


Figure 5.7: Wave function of 1s and 1p (even parity) electrons in three different electric fields.

electric field is further increased.

## 5.4 Conclusion

We calculated the energy levels of the quantum-confined electron and heavy hole of the GaAs QDR in the lateral electric field by means of the finite element method with the single-band effective-mass approximation. We assumed a three-dimensional model of the QDR that was derived from the shape of the specimen measured by AFM. For a vanishing electric field, we obtained energy levels consistent with the previous calculation by the exact diagonalization of the effective-mass Hamiltonian. These results were characterized by principal quantum number $N$ and azimuthal quantum number $l$ although we did not use the circular symmetry of the structure explicitly, which shows the accuracy of our calculation. The numerical results showed a transition from quadratic to linear behavior of the energy shift for the 1s electron and 1s heavy hole as a function of the applied electric field, which is consistent with the degenerate perturbation theory. On the other hand, energy levels of other states often showed non-monotonic changes due to repulsion with adjacent energy levels of the same spatial symmetry. Consequently, this behavior leads to anomalous behaviors of charge polarization and oscillator strength. We can attain a fairly large Stark shift of 4 meV that was recently observed in reported experiment by an external electric field of the order of 0.7 kV/cm. However, the observed shifted emission peak may not originate from the ground-state transition alone, but also from higher energy transitions whose emission have larger oscillator strength.

# Chapter 6:

# Aharonov-Bohm effect in QD-ring coupled nanostructures

## 6.1 Excitonic Aharonov-Bohm effect in the ring-shaped nanostructures

Since the first report on the self-assembly of semiconductor quantum rings in 1997 [139], ring-shaped nanostructures have attracted extensive attention as they offer a new platform to investigate the Aharonov-Bohm (A-B) effect using spectroscopic techniques. According to the formulation of A-B effect, the oscillation signature of single charged particles can be expected in their energy spectra. However, the A-B effect of exciton in the ring-shaped nanostructure may not be observed clearly due to the Coulomb interaction between the electrons and holes. To our best knowledge, the oscillation signature in both the experimental and the theoretical results of this case was not significant [70, 71].

In this chapter, we firstly studied the effect of magnetic field on the exciton state of a single quantum ring and revealed the reason for the vanishing excitonic A-B effect. We propose the use of coupled nanostructures to achieve a clear excitonic A-B effect. We focus on the self-assembled quantum-dot (QD)-ring coupled structures (denoted as QD-on-Ring hereafter), whose formation has recently been observed [72, 140] in the National Institute for Materials Science (NIMS). In this system, a QD is formed exactly above the center of a quantum ring. The QD and the ring are separated by a thin barrier layer (see the atomic-force microscope image in Fig. 6.1). Their advantage for the excitonic A-B effect is as follows: (1) By applying an electric field along the alignment direction of the QD and the ring, we can decrease the influence of the Coulomb interaction on the A-B effect by the partial separation of the electron and hole wave functions. (2) When the electron and hole are mainly located in the ring and the QD, respectively, the average radius of their angular motion has a large difference in the plane perpendicular to the magnetic field, which is desirable for an obvious A-B effect. In the present study, we examined the effects of the electric and magnetic fields on the electronic and optical properties of the QD-on-Ring nanostructures and found an obvious A-B effect.

## 6.2 Calculation of the excitons in ring-shaped nanostructures

A three-dimensional (3D) model of the QD-on-Ring with cylindrical symmetry was assumed in our calculation as shown in Fig. 6.1(c). A uniform thickness was assumed for

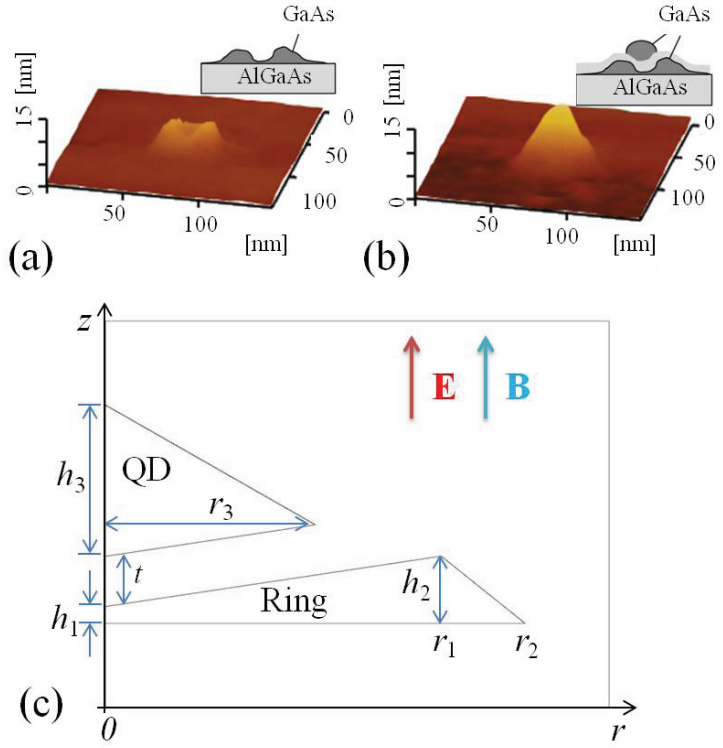


Figure 6.1: Atomic-force microscope images of (a) a quantum ring and (b) a QD-on-Ring nanostructure. The insets are the schematic illustrations of their cross sections. (c) Cross section of the QD-on-Ring model used in our calculation. The following parameters were assumed: QD radius $r_3 = 12.5$ nm, QD height $h_3 = 9$ nm, $h_1 = 1$ nm, $h_2 = 4$ nm, $r_1 = 20$ nm, $r_2 = 25$ nm. A barrier layer thickness of $t = 3$ nm was assumed to ensure the interaction between the QD and the ring [141].

the barrier layer between the QD and the ring. Static electric and magnetic fields were assumed to be applied along the growth direction ($z$-direction).

Because we were interested in the electronic states near the band edge, the effective mass approximation was used in this study. Due to the cylindrical symmetry, the $z$-projection of the single-particle angular momentum is a good quantum number. The energies and wave functions of the electron and hole, which were characterized by the angular quantum number $l_{e(h)}$ and the radial quantum number $n_{e(h)}$, were numerically calculated by solving the single-band Schrödinger equation by the finite element method. The exciton states were calculated with the configuration interaction method.

In the cylindrical coordinates $(r, z, \theta)$, the conventional single particle wave function can be assumed as $\varphi_{nl} = e^{il\theta} f_{n,l}(r,z)/\sqrt{2\pi}$ with the quantum number $l$ and $n$. $f(r,z)$ is the radial component of the single particle wave function.

The Coulomb matrix elements between the electron-hole pair state $|e1h1\rangle$ and $|e2h2\rangle$ is expressed as

$$\begin{aligned} &\langle e2h2\,|V_c|\,e1h1\rangle \\ = &\int\int\int\int\int\int \varphi^*_{e2}(\mathbf{r}_e)\varphi^*_{h2}(\mathbf{r}_h) V_c \varphi_{e1}(\mathbf{r}_e)\varphi_{h1}(\mathbf{r}_h) dz_e dz_h r_e dr_e r_h dr_h d\theta_e d\theta_h, \end{aligned} \tag{6.1}$$

in which $V_c$ is express in the cylindrical coordinates as

$$\begin{aligned} V_c &= \frac{e^2}{4\pi\varepsilon_0\varepsilon_r\,|\mathbf{r}_e - \mathbf{r}_h|} \\ &= \frac{e^2}{4\pi\varepsilon_0\varepsilon_r}\left[r_e^2 + r_h^2 + (z_e - z_h)^2 - 2r_e r_h cos(\theta_e - \theta_h)\right]^{-\frac{1}{2}}. \end{aligned} \tag{6.2}$$

Substituting the single particle wave function into Eq. (6.2)

$$\begin{aligned} &\langle e2h2\,|V_c|\,e1h1\rangle \\ = &\frac{1}{4\pi^2}\int\int\int\int\int\int f^*_{e2}(r_e,z_e) f^*_{h2}(r_h,z_h) V_c f_{e1}(r_e,z_e) f_{h1}(r_h,z_h) \\ &\exp\left[i\theta_e(l_{e1} - l_{e2}) + i\theta_h(l_{h1} - l_{h2})\right] dz_e dz_h r_e dr_e r_h dr_h d\theta_e d\theta_h. \end{aligned} \tag{6.3}$$

Considering the $\theta_e - \theta_h$ in $V_c$, let us introduce new variables $\theta_+ = \theta_e + \theta_h$ and $\theta_- = \theta_h - \theta_e$. We have $d\theta_e d\theta_h = \frac{1}{2} d\theta_+ d\theta_-$. Then the Coulomb matrix element with the new variables is

$$\begin{aligned} &\langle e2h2\,|V_c|\,e1h1\rangle \\ = &\frac{1}{8\pi^2}\int\int\int\int\int\int f^*_{e2}(r_e,z_e) f^*_{h2}(r_h,z_h)(V_c) f_{e1}(r_e,z_e) f_{h1}(r_h,z_h) \\ &\exp\left[\frac{i}{2}\theta_+(l_{e1} + l_{h1} - l_{e2} - l_{h2}) + \frac{i}{2}\theta_-(l_{e1} + l_{h2} - l_{e2} - l_{h1})\right] dz_e dz_h r_e dr_e r_h dr_h d\theta_+ d\theta_-. \end{aligned} \tag{6.4}$$

The integral on the $\theta_+$ requires $l_{e1} + l_{h1} = l_{e2} + l_{h2}$ to ensure a non-zero Coulomb

matrix element as

$$\begin{aligned} & \langle e2h2\,|V_c|\,e1h1\rangle \\ = & \frac{1}{2\pi}\int\int\int\int\int\int f^*_{e2}(r_e,z_e)f^*_{h2}(r_h,z_h)(V_c)f_{e1}(r_e,z_e)f_{h1}(r_h,z_h) \\ & \times\delta_{(l_{e1}+l_{h1}),(l_{e2},l_{h2})}\exp\left[i\theta_-(l_{e1}-l_{e2})\right]dz_e dz_h r_e dr_e r_h dr_h d\theta_+ d\theta_-. \end{aligned} \tag{6.5}$$

Because $\exp\left[i\theta_-(l_{e1}-l_{e2})\right] = \cos(l_{e1}-l_{e2})\theta_- + i\sin(l_{e1}-l_{e2})\theta_-$, and its imaginary part with sin function is odd in the integral region, only the real part will remain.

$$\begin{aligned} & \langle e2h2\,|V_c|\,e1h1\rangle \\ = & \frac{1}{2\pi}\int\int\int\int\int f^*_{e2}(r_e,z_e)f^*_{h2}(r_h,z_h)(V_c)f_{e1}(r_e,z_e)f_{h1}(r_h,z_h) \\ & \times\delta_{(l_{e1}+l_{h1}),(l_{e2},l_{h2})}\cos[(l_{e1}-l_{e2})\theta_-]dz_e dz_h r_e dr_e r_h dr_h d\theta_- \end{aligned} \tag{6.6}$$

The five-dimension integrations were calculated by the Monte Carlo method.

The size of our QD-on-R model is comparable with the GaAs exciton Bohr radius. The intermediate confinement leads to small contribution of the exchange interaction [98], so the exchange interaction was ignored in our calculation.

In the present study, the electron and hole effective masses were the same as the values in Table 5.1. The band gaps of 1.5194 eV and 1.9472 eV were taken for GaAs and $Al_{0.3}Ga_{0.7}As$ at low temperature [142]. The ratio of the band offset of the conduction band (CB) to the valence band (VB) was assumed to be 6:4, resulting in a CB offset of 0.2567 eV and a VB offset of 0.1711 eV. The dielectric constant of 12.53 was used for GaAs at low temperature [137]. For simplicity, the difference in the dielectric constant between GaAs and $Al_{0.3}Ga_{0.7}As$ was ignored.

## 6.3 Results and discussion

### 6.3.1 Exciton in 2D rings

We firstly discuss the excitonic A-B effect in a 2D GaAs ring, where the motion of the electron and hole is assumed to be confined in the $xy$ plane. With the assumption of a parabolic confinement potential, previous theoretical studies predicted a vanishing A-B effect for the exciton ground state of 2D rings due to the Coulomb interaction [143, 144]. But the parabolic confinement is not appropriate for the study of the A-B effect of quantum rings with a large width because of the loss of ring features due to the vanishing central hole. In our calculation, we applied a square potential-well confinement along the radial direction. In the following, the radius ($R$) and the width ($W$) of the ring are defined as the average value of the inner ($R_i$) and outer radius ($R_o$) of the ring and their difference.

The influence of the magnetic field on the single particle states was calculated by the first-order perturbation theory [145]. The Hamiltonian of the single particle was expressed in the polar coordinates as

$$H = \quad H_0 + H^{'}(B),$$

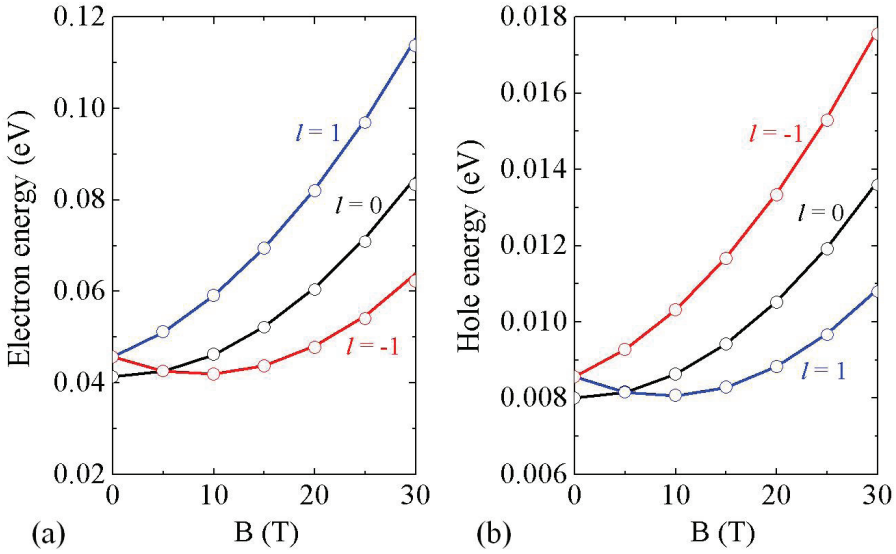


Figure 6.2: The perturbative calculation results (solid lines) and the numerical results (circles) of the energy of (a) electron and (b) hole states with the lowest radial quantum number as a function of the magnetic field for a 2D ring with $R = 12$ nm and $W = 8$ nm. (c) The average radii of the electron (solid lines) and hole (dashed lines) states with the angular quantum number of 0 (squares), 1 (triangles), and -1 (circles) as a function of the magnetic field [141].

$$
\begin{aligned}
H_0 = &\quad -\frac{\hbar^2}{2m^*}\left[\frac{1}{r}\frac{\partial}{\partial r}\left(\frac{1}{r}\frac{\partial}{\partial r}\right)+\frac{1}{r^2}\frac{\partial^2}{\partial\theta^2}\right]+V(r), \\
H^{'} = &\quad -\frac{\hbar^2}{2m^*}\left[-\frac{iqB}{\hbar}\frac{\partial}{\partial\theta}-\frac{(qBr)^2}{4\hbar^2}\right],
\end{aligned}
\tag{6.7}
$$

where $H_0$ is the Hamiltonian for $B = 0$ and $H^{'}(B)$ is the perturbative part. Symmetric gauge was applied for the vector potential. $V(r)$ is the confinement potential, which is equal to zero in the GaAs ring and equal to the band offset in the $Al_{0.3}Ga_{0.7}As$ barrier layer. $q = -e$ and $e$ for electron and hole, respectively. $m^*$ is the effective mass for electron and hole, which is different between the GaAs ring and the $Al_{0.3}Ga_{0.7}As$ barrier layer. The calculation of the single particle state in a 2D ring without the magnetic field is shown in the Appendix.

The second-order energy correction was much smaller than the first-order term, which was confirmed by our numerical calculation. In Fig. 6.2, the numerical results of the single particle energy calculated by the finite element method show a good agreement with the first-order perturbative results, which confirms the validity of our calculation. In the first-order perturbation, we evaluated $\langle\varphi_{nl}|r^2/m^*|\varphi_{nl}\rangle$ by numerical integration using unperturbed wave function $\varphi_{nl}$ given in the Appendix. The matrix element can be approximated by $\langle\varphi_{nl}|r^2|\varphi_{nl}\rangle/\overline{m^*}$, where $\overline{m^*}$ is $\langle\varphi_{nl}|m^*|\varphi_{nl}\rangle$, since the difference in $m^*$

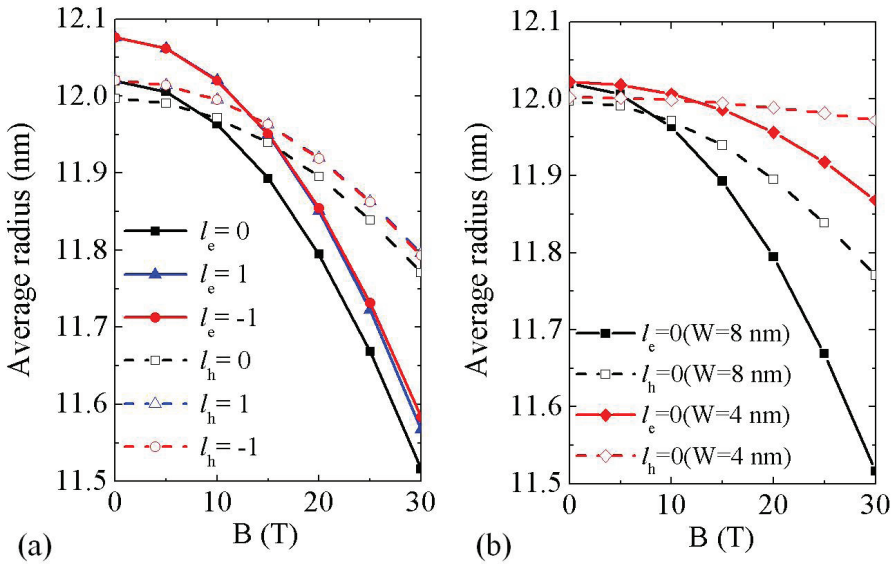


Figure 6.3: (a) The average radii of the electron (solid lines) and hole (dashed lines) states with the angular quantum number of 0 (squares), 1 (triangles), and -1 (circles) as a function of the magnetic field for the 2D ring in Fig. 6.2. (b) The average radius of the lowest electron (solid lines) and hole (dashed lines) states as a function of the magnetic field for a 2D ring with $R = 12$ nm and different ring width $W = 8nm$ (squares) , $W = 4$ nm (diamonds).

between GaAs and $Al_{0.3}Ga_{0.7}As$ is small (less than 30%). Then, the single particle energy with the first-order correction is

$$E_{nl}(B) \cong E_{nl}(0) - \frac{\hbar^2 l^2}{2\overline{m^*}\langle\varphi_{nl}|r^2|\varphi_{nl}\rangle} + \frac{\hbar^2}{2\overline{m^*}\langle\varphi_{nl}|r^2|\varphi_{nl}\rangle}\left(l - \frac{\phi'}{\phi_0'}\right)^2, \tag{6.8}$$

where $E_{nl}(0)$ is the energy of the single particle state for $B = 0$, $\phi' = B\pi\langle\varphi_{nl}|r^2|\varphi_{nl}\rangle$, and $\phi_0' = 2\pi\hbar/q$. The last term on the right-hand side of Eq. (6.8) is $B$-dependent and has a similar form as Eq. (1.1) of the 1D ring [67] in Chapter 1 except for three main differences: First, when $B = 0$, the energy of the lowest state is dependent on both the angular momentum and the confinement along the radial direction; Second, the fixed 1D ring radius is replaced with the average radius of the single particle that depends on the ring width and varies for different states; Third, because of the finite potential barrier height, the average value of the effective mass was used to take their $r$ dependence into consideration. When the width of the 2D ring is infinitesimally small, the $B$ dependence of Eq. (6.8) approaches Eq. (1.1).

The average radius of the electron and hole in the 2D ring varies for different angular quantum number and the magnetic field as shown in Fig. 6.3(a). Because the magnetic-field-induced potential pushes both the electron and hole towards the center of the structure, the average radius decreases with increasing magnetic field. The average

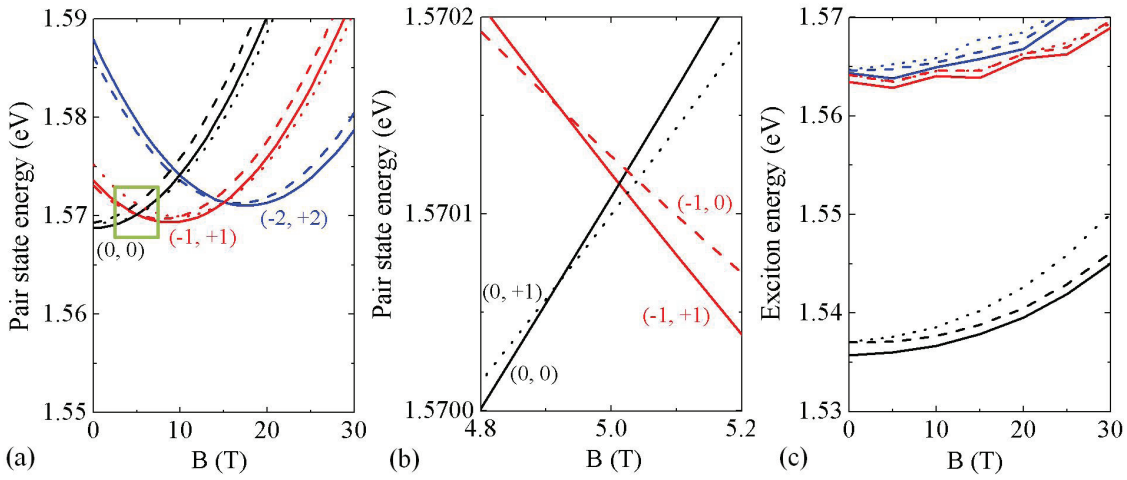


Figure 6.4: (a) Energy of the non-interacting pair states with total angular momentum $L = 0, -1$ and $+1$ as a function of the magnetic field for a 2D ring with $R$= 12 nm and $W$= 8 nm. The combination of the electron and hole angular quantum number $(l_e, l_h)$ is denoted for the low-energy pair states with $L = 0$. (b) The magnified figure of the region in the green square in (a). (c) Exciton energy as a function of the magnetic field for $L = 0, -1$ and $+1$ in the same 2D ring. For both the pair states and the excitons, the states with $L = 0, -1$ and $+1$ are plotted with the solid lines, dashed lines, and dotted lines, respectively. For each $L$, the first, second and third lowest states are plotted in black, red and blue colors, respectively [141].

radius reduction of the electron is faster than the hole due to the larger kinetic energy of the former. According to Eq. (6.8), the energy oscillation period of the lowest single particle state is determined by its average radius. Figure 6.2(c) shows that the low-energy electron and hole states have a very similar average radius when $B < 15$ T. Therefore, the energy oscillation periods of the lowest electron and hole states are close to each other, which is seen in Fig. 6.2(a) and (b).

The energy of the non-interacting pair state $E_{ps}(B)$ $(= E_g + E^{(e)}_{nl}(B) + E^{(h)}_{n'l'}(B)$, $E_g$: band gap of GaAs) is shown in Fig. 6.4(a). For the lowest pair state, the oscillating energy is observed with increasing $B$. By magnifying the region surrounded by the green square in Fig. 6.4(a), the total angular momentum transition from $L = 0$ to 1 for the lowest-energy pair state is found in a narrow magnetic field range as shown in Fig. 6.4(b), which is attributed to the similar energy oscillation period for the electron and hole states.

The exciton energy of the 2D ring was calculated by the configuration interaction method as shown in Fig. 6.4(c). The A-B oscillation was not observed for the exciton ground state, but was found in the excited states, which agrees with Ref. [143]. By the configuration interaction method, we can also analyze the contribution of each pair state to the exciton ground state. We found that the wave functions of the pair states with the same $L$ were mixed by the Coulomb interaction, and the crossing behavior between

their energies was replaced by an anti-crossing behavior. So, the oscillation feature of the magnetic field dependence of the lowest pair state energy was smoothed, and the narrow $B$ range for the non-zero $L$ vanished. These resulted in the disappearance of the excitonic A-B effect, and the lowest exciton was always a bright one with $L = 0$. Note that the electric-dipole transition between the excited state and the ground state is allowed only for excitons with $L = 0$ due to the conservation of angular momentum [20]. As an evidence of the Coulomb mixing, we found that as the magnetic field increased, the angular momentum of the largest contributing pair state for the exciton ground state changed from $(l_e = 0, l_h = 0)$ to $(l_e = -1, l_h = +1)$ and $(l_e = -2, l_h = +2)$ for $B = 10$ and 20 T, respectively. Our analysis showed that the Coulomb interaction was the reason for the vanishing A-B effect in the 2D ring.

### 6.3.2 QD-on-Ring nanostructures

To avoid the Coulomb mixing among pair states, we may increase their kinetic energy interval by decreasing the width of the ring. But this method may simultaneously decrease the difference between the electron and hole average radii, which is undesirable for the A-B effect. If a ring with a small radius is used alternatively, the energy oscillation and the $L$ transition of the exciton ground state may occur for a large magnetic field, which causes difficulty for experimental studies. Thus, in previous theoretical and experimental investigations, the visibility of the excitonic A-B effect was not clear for 3D rings [60, 70].

For a clear excitonic A-B effect in 3D nanostructures, we propose the use of the QD-on-Ring nanostructure with an applied electric field ($E$) along the growth direction. The advantages of the coupled nanostructure stated in the introduction section are also the conditions for the realization of a clear A-B effect. The recently reported QD-on-Rings fulfill these conditions [72], thus the effect of the magnetic field on the exciton states of the QD-on-Ring was numerically investigated to verify the appearance of the A-B effect. The model assumed in our calculation was shown in Fig 6.1. The geometric parameters were taken according to the AFM measurement. To show the coupling of the single particle states in the QD and ring part in a QD-on-Ring nanostructure, the calculated energy of the lowest electron and hole states was plotted as a function of the barrier layer thickness (t) as shown in Fig 6.6. With decreasing t, the energy of the single particle states decrease because of the extension of the wave function in the entire QD-on-Ring nanostructure and the wave functions in the QD and ring parts mixed with each other. According to the calculation result, the QD-on-Ring with t= 3 nm has coupled QD and ring parts.

Figure 6.5(a) shows the exciton energy of the QD-on-Ring as a function of the magnetic field for $E = 0$. Neither the energy oscillation nor the $L$ transition was observed for the exciton ground state because the electron and hole were strongly bound (binding energy of 27 meV) in the QD part as can be seen from their average radii in Fig. 6.7(a).

When an electric field is applied, the excitons have lower energy than those for $E = 0$ due to the Stark shift [20] as shown in Fig. 6.5. When $B = 0$, the largest contributing pair state for the lowest exciton state with $L = 0$ is $(l_e = 0, n_e = 1, l_h = 0, n_h = 1)$, in which the electron is redistributed from the QD to the ring with the increasing electric field and the hole remains in the QD.

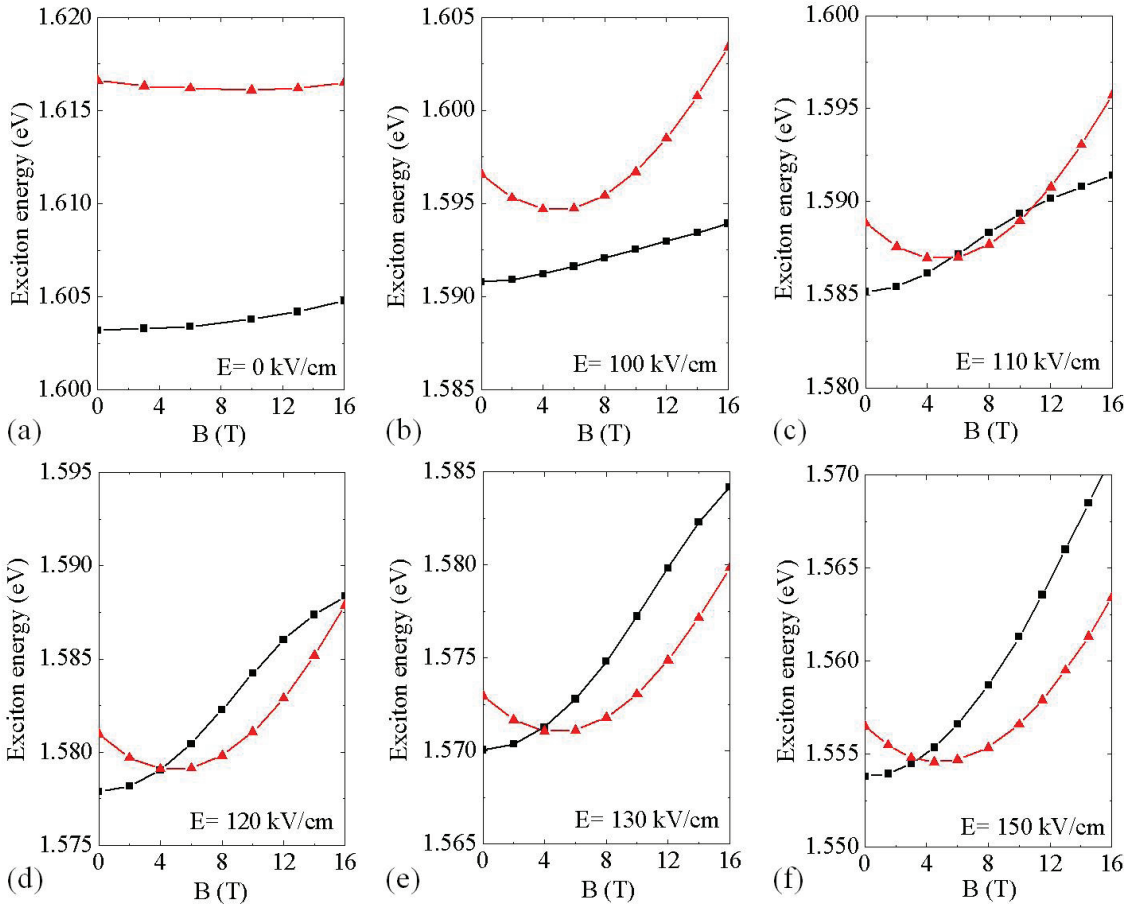


Figure 6.5: Energy of the lowest exciton states with the total angular momentum $L = 0$ and $-1$ in the QD-on-Ring nanostructure as a function of the magnetic field for different applied electric fields ($E$). The exciton states with the total angular momentum $L = 0$ and $-1$ are plotted with the solid squares and triangles, respectively [141].

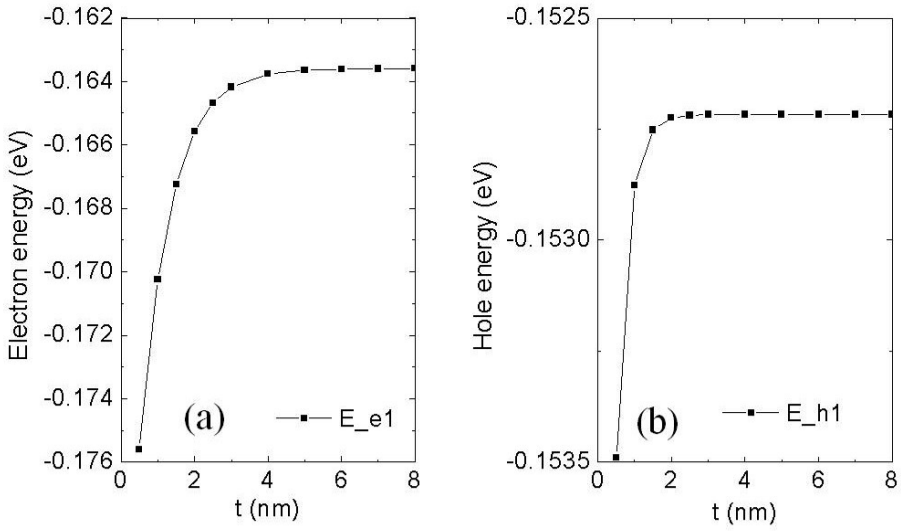


Figure 6.6: The energy of the (a) lowest electron state and (b) lowest hole state as a function of the barrier layer thickness (t) between the QD and the ring in a QD-on-Ring nanostructure.

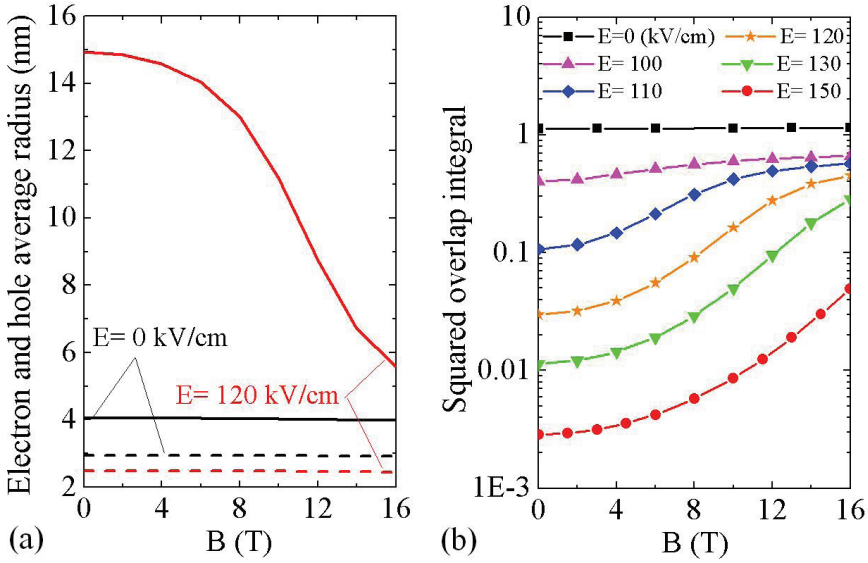


Figure 6.7: (a) The electron (solid lines) and hole (dashed lines) average radii of the lowest exciton state with $L = 0$ as a function of the magnetic field for $E = 0$ (in black color) and $E = 120$ kV/cm (in red color). (b) The squared overlap integral of the lowest exciton state with $L = 0$ as a function of the magnetic field for $E = 0$, 100, 110, 120, 130 and 150 kV/cm [141].

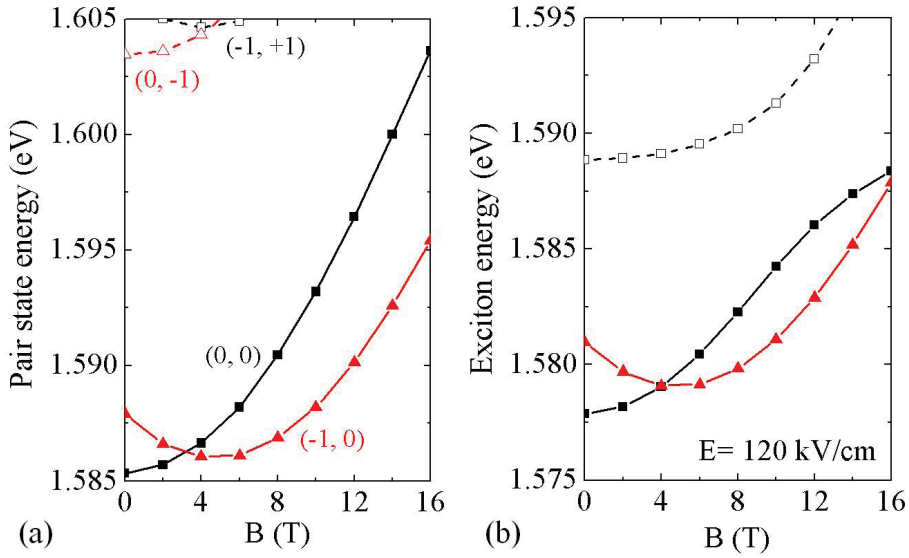


Figure 6.8: Energy of the (a) non-interacting pair states and (b) exciton states in the QD-on-Ring nanostructure as a function of the magnetic field for the electric field $E = 120$ kV/cm. The states with the total angular momentum $L = 0$ and $-1$ are plotted with the black squares and red triangles, respectively. For each $L$, the lowest state and the excited state are plotted with the solid lines and the dashed lines, respectively. The combination of the electron and hole angular quantum number $(l_e, l_h)$ is denoted for the pair states [141].

Figure 6.8(a) shows the pair state energy of the QD-on-Ring for $E = 120$ kV/cm as an example. When $B = 0$, the lowest electron and hole states are separated in the ring and QD, respectively. According to Eq. (1.1), the kinetic energy of single particles is inversely proportional to the square of its trajectory radius, thus the energy difference between the electron states (in the ring) with $l_e = 0$ and $l_e = \pm 1$ is smaller than that between the hole states (in the QD) with $l_h = 0$ and $l_h = \pm 1$ for $E = 120$ kV/cm. This leads to a large energy difference between the lowest pair states (with $L = 0, -1$) and the corresponding higher energy pair states with nonzero-$l_h$ hole involved as shown in Fig. 6.8(a). By the charge separation, the Coulomb binding energy (7 meV) of the lowest exciton is smaller than this energy difference, which avoids the Coulomb mixing. At the same time, the magnetic field response of the lowest pair states with $L = 0, -1$ is dominated by that of the electron which is localized in the ring and has a larger trajectory radius, so a clear $L$ transition is observed in Fig. 6.8(a). When Coulomb interaction is taken into consideration, the electron and hole remain spatially separated with a big difference in their average radii as shown in Fig. 6.7(a), which results in a large magnetic flux between their trajectories. So a clear A-B effect is observed for $E = 120$ kV/cm as shown in Fig. 6.8(b).

The magnetic-field-induced potential leads to the decreasing average radii of both the electron and hole as shown in Fig. 6.7(a). Furthermore, the squared overlap integral of the lowest exciton ($L = 0$) increases with the magnetic field as shown in Fig. 6.7(b). This leads to an increasing binding energy and the effect of the Coulomb mixing becomes obvious, shown as the anti-crossing behavior between the first and second lowest exciton ($L = 0$) for $B = 12$ T in Fig. 6.8(b). The influence of the magnetic field on the distribution of the low-energy single particles partly cancels for the electric-field-induced charge separation.

The lowest exciton for $E = 0$ is always a bright exciton. When the $L$ transition occurs for the exciton ground state at $B = 4$ T for $E = 120$ kV/cm, this bright exciton with a non-negligible squared overlap integral turns dark. Therefore, we propose an excitonic A-B effect with the moderate external fields, which may be verified by the experimental observation of the emission spectra by tuning the applied electric field.

### 6.3.3 QD-in-Ring nanostructures

Motivated by the synthesis of the QD-Ring nanostructure which was reported in 2011 for the first time [65], we searched for other methods to obtain clear excitonic A-B effect. We propose another QD-Ring coupled nanostructure for the electric field tunable A-B effect of the exciton in this section. As shown in Fig. 6.9(b), this nanostructure consists of a ring and a QD located in the center of the ring. To distinguish from the QD-on-Ring nanostructure mentioned before, we denoted this nanostructure as QD-in-Ring hereafter. Previous theoretical studies showed that the electronic structure of a QD-in-Ring is a combination of that of a QD and a ring [146]. The wave function distribution of the low-energy electron is in the QD or the ring, which is sensitive to the confinement of the QD and ring parts [147]. Till now, the influence of donor impurities and lateral electric field on the electron states were reported [148–150]. To the best of our knowledge,

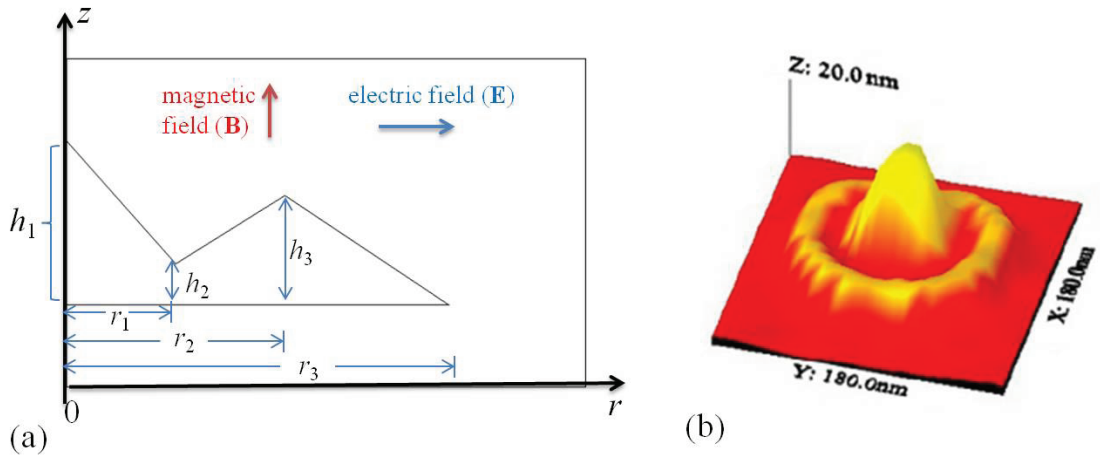


Figure 6.9: The cross section of the QD-in-Ring model used in our calculation. The material of QD-in-Ring is GaAs in the present calculation. The barrier material surrounding the QD-on-Ring is $Al_{0.3}Ga_{0.7}As$. (b) atomic force microscope (AFM) image of a GaAs QD-in-Ring nanostructure [65].

the study of exciton state in the QD-in-Ring nanostructure has not been reported. In the last section, we proposed the necessary conditions for the occurrence of the A-B effect in a coupled nanostructure. According to these conditions, if the electric field is applied along the radial direction of a QD-in-Ring nanostructure and leads to the charge separation, the A-B effect can be expected.

We assumed a 3D model for the QD-in-Ring with cylindrical symmetry, whose cross-section is shown in Fig. 6.9. In 1999, Zhitenev et al. realized the electric field along the radial direction for the measurement of the single-electron capacitance spectroscopy of a GaAs QD by a combination of a top gate and a surrounding side gate [151]. Thus our assumption of the applied electric field along the radial direction is reasonable. The uniform magnetic field was assumed to be applied along the growth direction ($z$-direction). The following parameters were assumed for the QD and ring in Fig. 6.9: $r_1 = 5.5$ nm, $r_2 = 8$ nm, $r_3 = 14$ nm, $h_1 = 4$ nm, $h_2 = 1.5$ nm, $h_3 = 4$ nm. In the present study, the electron and hole effective masses as well as the GaAs dielectric constant are the same as those used in our study of QD-on-Ring in the previous section. The band offset of the conduction band (CB) and the valence band (VB) are assumed to be 0.252 eV and 0.147 eV [152]. The calculation method is similar to that in the previous section. In the appendix, we found a good agreement for the comparison of the single particle state energy between the numerical calculation results and the semi-analytical solution in a QD-in-Ring for different angular momentum $l_e$, which verifies the accuracy of our present numerical calculation.

Figure 6.10 shows the exciton energy as a function of the magnetic field. When the external electric field is zero, the main part of the wave functions of the lowest electron and hole states are both in the QD part, consequently, the A-B effect of the exciton ground state was suppressed. We notice that a small part of the wave function of the low-energy

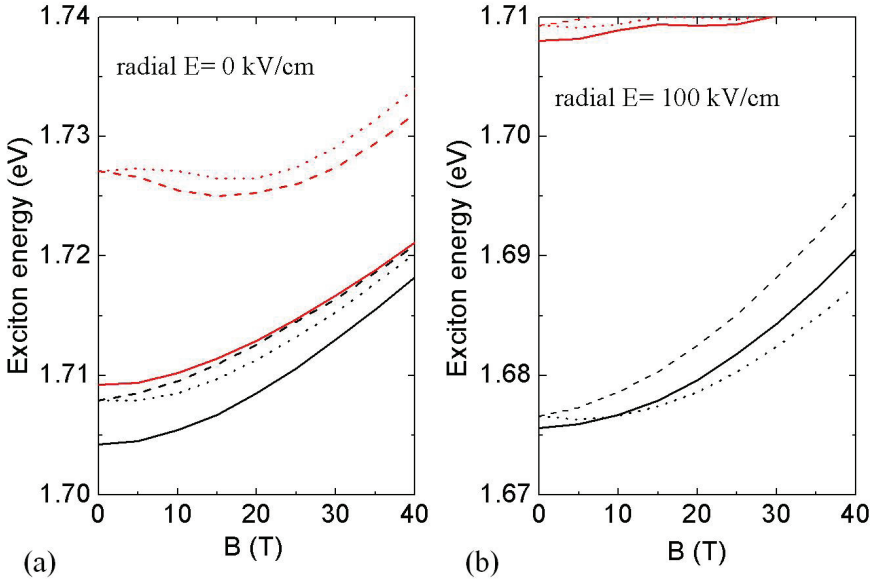


Figure 6.10: The exciton energy as a function of the magnetic field for different applied electric field along the radial direction in a QD-in-Ring nanostructure. The exciton states with the total angular momentum number $L = 0, 1, -1$ are distinguished with solid lines, dotted lines and dashed lines. For each $L$, the first and second lowest exciton states are plotted in black and red colors, respectively.

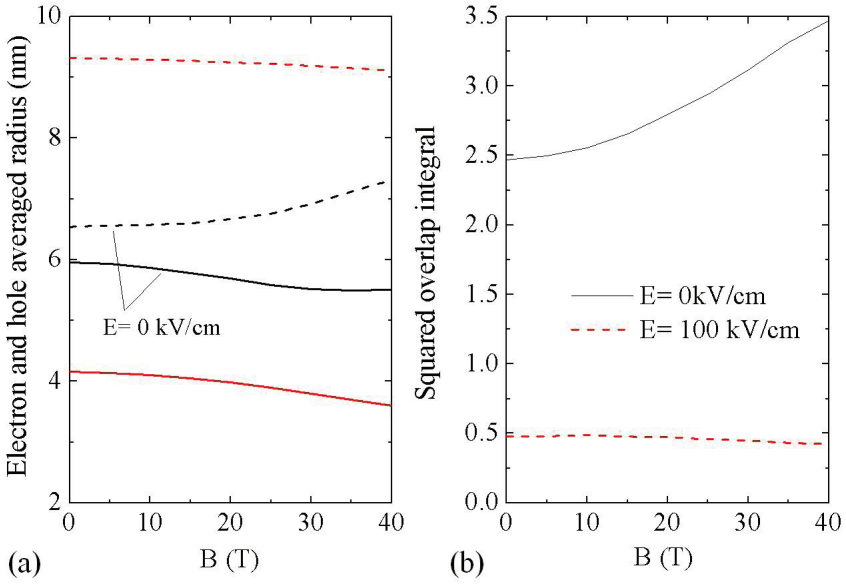


Figure 6.11: (a) The electron (solid line) and hole (dash line) average radius of the lowest exciton with the total angular momentum number $L = 0$ as a function of the magnetic field for radial electric field $E = 0$ (in black) and $E = 100$ kV/cm (in red). (b) The squared overlap integral of the lowest exciton with $L = 0$ as a function of the magnetic field for $E = 0$ (solid line) and $E = 100$ kV/cm (dashed line).

electron and hole can penetrate the barrier between QD and ring and reach the ring part. Therefore the weak confinement leads to the small energy spacing between the hole levels, for instance, the energy spacing between lowest hole states with $(l_h = 0, n_h = 1)$ and $(l_h = 0, n_h = 2)$ is 5.6 meV. Accordingly, the low-energy pair states $(l_e = 0, n_e = 1; l_h = 0, n_h = 1)$ and $(l_e = 0, n_e = 1; l_h = 0, n_h = 2)$ was mixed by the Coulomb interaction. Meanwhile, the lowest exciton with $L = 1$ has the main contribution from the charge-separated pair states, and consequently has a small binding energy. The difference between the binding energies of the lowest excitons with $L = 0$ and $L = 1$ led to large energy difference between these two exciton states and the occurrence of the $L$ transition was suppressed.

By increasing the applied electric field, the electrons and holes are separated along the radial direction into the QD and ring parts, which can be seen from their average radius as shown in Fig 6.11(a). The applied electric field pushes the hole towards the edge of the QD-in-Ring with strong confinement, thus the energy spacing between the pair states increases. On the other hand, the binding energy of the exciton ground state was decreased due to the charge separation. When $E = 100$ kV/cm the binding energy could be smaller than the pair state energy intervals, which avoids the Coulomb mixing. The movement of weakly-bound electrons and holes will lead to an area difference between their trajectories. The magnetic flux through this area difference leads to the A-B effect.

Figure 6.11(b) showed the squared overlap integral of the lowest exciton with $L = 0$, which is a bright exciton corresponding to the dipole allowed transition. The increasing magnetic field induces a potential proportional to $r^2$, which pushes both the electron and hole towards the center of the nanostructure. This effect of the magnetic field enhances the overlap between electron and hole wave functions for $E = 0$. With a non-zero electric field, the squared overlap integral is smaller than that for $E = 0$ due to the charge separation. The electric field prevents the holes from moving toward the electrons, which is opposite to the effect of the magnetic field. The wave function of single particle state is sensitive to the mutual influence of the electric field and magnetic field. With the increasing magnetic field, the wave function of the electron with large kinetic energy concentrate towards the center of the structure, but the hole with small kinetic energy can not tunnel from the ring to the QD due to the mutual influence of the electric field and the confinement. Accordingly, the squared overlap integral shows a very small decreasing behavior rather than the increasing tendency as a function of the magnetic field as shown in Fig 6.11(b). For $B = 10$ T where the $L$ transition takes place for the exciton ground state with $E = 100$ kV/cm, the transition from bright exciton to a dark one may be detected in the PL measurement.

Because the magnetic field has the influence on the electron and hole distribution along the radial direction in a QD-ring coupled nanostructure, the electric field along radial direction in QD-in-Ring cancels the effect of magnetic field more serious than the electric field in the QD-on-Ring along the growth direction. Therefore, the QD-on-Ring is supposed to be more desirable for the occurrence of a clear A-B effect.

## 6.4 Conclusion

By the first-order perturbation theory and the configuration interaction method, we derived the magnetic-field dependence of both the non-interacting electron-hole pair-state energy and the exciton energy in a two-dimensional quantum ring. We showed that the Coulomb interaction between the electron and hole mixes the wave functions of pair states with the same total angular momentum, which modifies the magnetic-field dependence of the exciton energy and results in the disappearance of the excitonic Aharonov-Bohm (A-B) effect.

To avoid this situation and observe a clear excitonic A-B effect, we proposed the use of the QD-Ring coupled nanostructures, composed of a quantum dot located on the top of a quantum ring (QD-on-Ring) or in the center of a quantum ring (QD-in-Ring), which were recently reported by the experimental studies. We showed that by applying a static electric voltage along the alignment direction of the quantum dot and the ring we can simultaneously achieve the partial separation of the electron and hole wave functions to reduce the Coulomb mixing and the control of the average radius of their trajectories to enhance the A-B effect. We showed that we can observe the excitonic A-B effect with moderate experimental conditions, and our proposal is supposed to be verified by the measurement of the change of the emission spectrum intensity.

# Chapter 7:

# Exciton complex in quantum dots and quantum rings

## 7.1 Introduction

As mentioned in Chapter 6, in order to reveal the influence of the Coulomb interaction on the A-B effect, many theoretical studies concentrate on the A-B effect of the exciton state in quantum rings. We also discuss the importance of the Coulomb interaction on the vanishing excitonic A-B effect in quantum rings. On the other hand, the number of theoretical investigations is limited for the A-B effect of the trion and the biexciton states that have more complicated Coulomb interaction among particles. In 2003, the influence of the magnetic field on the exciton and the trion in a quantum ring was reported for the first time by the observation of PL spectra [60]. Oscillation feature of A-B effect was found for the lowest emission peak energy of trion, but did not occur for the exciton, which was attributed to its neutral charge. L. Porras et al. studied the exciton and the positive trion in a quantum ring confined with infinitely high barrier potential, and the radius of the ring is assumed to be much larger than the exciton Bohr radius [153]. With the assumption of a small ring cross section (in the growth and radial directions), their model could be reduced to a simple 1D ring with the adiabatic approximation [154]. Ground state energy oscillation was not observed for the exciton and the trion due to the strong electrostatic attraction.

The assumption of the 1D ring model and the infinite barrier height overestimate the Coulomb energy that is important for the A-B effect. On the other hand, these assumptions decrease the difference between the trajectory radius of electron and hole, which leads to the difficulty for the observation of A-B effect as we mentioned in Chapter 6. In this chapter, we assumed a three-dimensional (3D) quantum ring with the radius comparable to the exciton Bohr radius and took a finite barrier height into consideration. We calculated the magnetic response of the exciton and the trion state by the CI method and clarified the influence of Coulomb interaction on the occurrence of the A-B effect.

## 7.2 Theory and model

We focused our study on the electron and the hole states near the band edge, thus the effective mass approximation was applied for the calculation of the single particle states. The trion states in a spherical QD were calculated and compared with the published data to confirm the correctness and the accuracy of our calculation. The exciton and the trion states in both the spherical QD and the quantum ring were calculated in the cylindrical

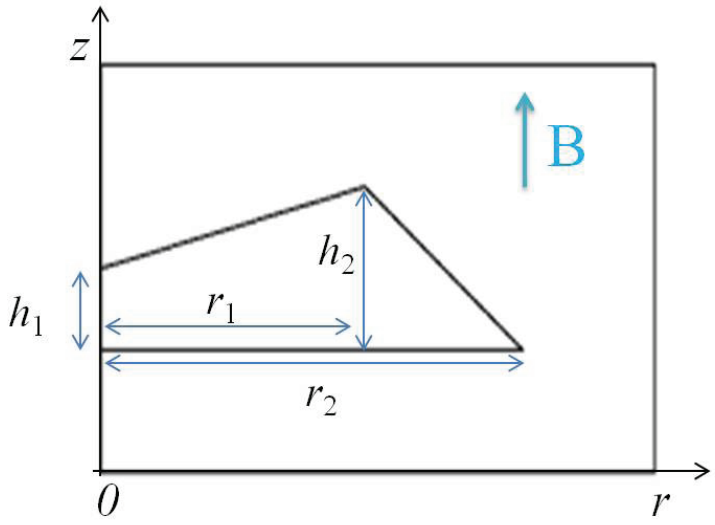


Figure 7.1: Cross section of the model used for the calculation of the electronic structure of a GaAs ring of the cylindrical symmetry. The GaAs quantum ring was assumed to be embedded in the barrier layer of $Al_{0.3}Ga_{0.7}As$. The following parameters were assumed for the ring: $r_1 = 10$ nm, $r_2 = 16$ nm, $h_1 = 2$ nm, $h_2 = 4$ nm.

coordinates.

A 3D model of the quantum ring was assumed with the cylindrical symmetry, whose cross-section is shown in Fig. 7.1. The uniform magnetic field was assumed to be applied along the growth direction ($z$-direction). The symmetric gauge was applied to the magnetic vector potential. The corresponding components of the vector potential are $A_\theta = Br/2$, $A_r = 0$ and $A_z = 0$ in the cylindrical coordinates.

The radius of the ring is chosen to be comparable to the bulk GaAs exciton Bohr radius of 15.5 nm [95]. The quantum ring is not in the strong confinement regime. Therefore, the Coulomb energy is important for its exciton and trion state. In our model, the central hole does not penetrate the ring according to the atomic force microscope measurements of the GaAs ring prepared by droplet epitaxy technique [63].

In the present study, the band offset of the conduction band (CB) and the valence band (VB) are assumed to be 0.252 eV and 0.147 eV [152]. The parameters of effective masses and dielectric constant are the same as those in Chapter 6.

The single particle states were characterized by the angular momentum quantum number $l$ and radial quantum number $n$. To obtain the energies and the wave functions of the single particle states, the single band Schrödinger equation was numerically solved by using the finite element method.

We take the negatively charged exciton (negative trion) as an example and express the equations for our calculation of the trion state energy by the CI method. The Schrödinger equation for the negative trion is

$$H\Psi = (H_1 + H_2)\Psi = E\Psi \tag{7.1}$$

where $H_1$ is the summation of the single particles Hamiltonians of their kinetic energy, and $H_2$ is the two-body interaction part given by

$$H_2 = -V_{e1h}(\mathbf{r}_{e1}, \mathbf{r}_h) - V_{e2h}(\mathbf{r}_{e2}, \mathbf{r}_h) + V_{e1e2}(\mathbf{r}_{e1}, \mathbf{r}_{e2}) \tag{7.2}$$

where the $\mathbf{r}_{e1}, \mathbf{r}_{e2}, \mathbf{r}_h$ are the coordinates of two electrons and one hole, respectively. The wave function of trion is expressed as a linear combination of the 3-body basis states composed of the wave functions of two electrons and one heavy hole

$$\Psi = \sum_i a_i [\psi_{e1}(\mathbf{r}_{e1})\psi_{e2}(\mathbf{r}_{e2})\psi_{h1}(\mathbf{r}_h)]_i \tag{7.3}$$

where $i$ denotes the set of quantum numbers $(l_{e1}, n_{e1}, l_{e2}, n_{e2}, l_h, n_h)$ for the 3-body basis state. By multiplying $\psi^*_{e3}(\mathbf{r}_{e1})\psi^*_{e4}(\mathbf{r}_{e2})\psi^*_{h2}(\mathbf{r}_h)$ to the Schrödinger equation and taking the integral, the matrix elements of the two-body interaction Hamiltonian can be expressed as

$$\begin{aligned} & \langle e3\ e4\ h2\,|H_2|\,e1\ e2\ h1\rangle \\ = \ - \ & \delta_{e2,e4}\langle e3\ h2\,|V_{e1,h}|\,e1\ h1\rangle \\ - \ & \delta_{e1,e3}\langle e4\ h2\,|V_{e2,h}|\,e2\ h1\rangle \\ + \ & \delta_{h1,h2}\langle e3\ e4\,|V_{e1,e2}|\,e1\ e2\rangle \end{aligned} \tag{7.4}$$

In the cylindrical coordinates, the wave function of a single particle state was assumed as

$$\psi(\mathbf{r}) = \psi_{nl}(\mathbf{r}) = \exp(il\theta) f_{nl}(r, z)/\sqrt{2\pi} \tag{7.5}$$

where $f_{nl}$ is the radial component of the single particle wave function. The matrix elements for one electron and one hole, e.g. $\langle e3, h2|V_c|e1, h1\rangle$ is

$$\begin{aligned} & \langle e3h2|V_c|e1h1\rangle = \frac{1}{2\pi}\delta_{(l_{e3}+l_{h2}),(l_{e1}+l_{h1})} \\ \times \ & \int\int\int\int\int f^*_{e3}(r_e, z_e) f^*_{h2}(r_h, z_h) f_{e1}(r_e, z_e) f_{h1}(r_h, z_h) \\ \times \ & \cos[(l_{e1} - l_{e3})\theta_-] V_c dz_e dz_h r_e dr_e r_h dr_h \end{aligned} \tag{7.6}$$

where $\theta_- = \theta_e - \theta_h$, and $V_c$ is express in Eq. 6.2. The matrix elements for two electrons have the similar expression. The average distance between an electron and a hole of a trion was calculated by $\left\langle e1h1|\sqrt{(\mathbf{r}_e - \mathbf{r}_h)^2}|e1h1\right\rangle$. Because the two-body interaction term is invariable by the rotation around the $z$-axis, total angular momentum $L = l_{e1} + l_{e2} + l_{h1}$ is a good quantum number for a negative trion.

The equation of Coulomb matrix element is a multi-dimension integral that can be numerically calculated by the Monte Carlo method. The advantage of the Monte Carlo method was introduced in Chapter 2. As we mentioned before, one of the strategies to improve the slow convergence of the Monte Carlo method is the application of the importance sampling method. For the study of the spherical QD in this section, the wave functions of single particles barely penetrate into the barrier layer for deeply confined

electronic states. For this case, the calculation of the Coulomb matrix element can be accelerated with importance sampling method that increases the number of sampling points in the QD region with a Gaussian distribution function.

When the spin configuration is considered for the trion (3-body system), the combination of the spin of each particle leads to eight states. Classified by the eigen value $s$ of the total spin operator $\mathbf{S} = \mathbf{S_1} + \mathbf{S_2} + \mathbf{S_3}$, these eight states can be divided into three groups: two groups of doublet states with $s = 1/2$ and one group of quadruplet states with $s = 3/2$. For the quadruplet states or doublet states, we need to calculate six or ten Coulomb terms, respectively. As we mentioned in Chapter 2, the exchange interaction was not considered in our calculation of GaAs nanostructures due to its small contribution.

## 7.3 Binding energy of exciton complex in spherical quantum dots

The single particle state energy of a spherical QD can be easily solved by a semi-analytical method according to many textbooks. In the present study, the energy and the wave functions of single particle states were numerically calculated with finite element method. The numerical results of cylindrical coordinates showed a good agreement with the semi-analytical calculation.

To verify the validity of our calculation of the trion states by the CI method, we repeated the calculation of trion binding energy in a spherical QD conducted by the quantum Monte Carlo method in Ref. [155]. Figure 7.2(a) shows the exciton energy and the ground state binding energy of a spherical QD as a function of the QD radius. The definition of the binding energy is $E_b^X = E_e + E_h - E_X$ for the exciton and $E_b^{T_n(T_p)} = E_{e(h)} + E_X - E_{T_n(T_p)}$ for the negative trion ($T_n$) and the positive trion ($T_p$), where $E_e, E_h, E_X, E_{T_n(T_p)}$ correspond to the energy of the electron, the hole, the exciton and the trion state, respectively. Our numerical results of the exciton ground state energy showed a good agreement with the published data. Our calculation reproduced the increasing binding energy as a function of the decreasing QD radius due to the enhanced overlap between the electron and the hole wave functions. More importantly, a small binding energy for the QD with a radius of 2 nm was also found in our calculation that is attributed to the decreasing wave function overlap between the electron and the hole due to the delocalization of the electron wave functions out of the small QD.

It is worth noting that, the difference in the dielectric constant of QD and outside space was not taken into consideration in our calculation. Considering the outside space with smaller dielectric constant, our calculation may underestimate the Coulomb interaction, as shown in Fig. 7.2(a). With decreasing QD radius, larger part of electron wave function penetrates out of the QD, which leads to more serious underestimation of Coulomb binding energy. Meanwhile, in smaller QD, more high-energy electron states have kinetic energy larger than the confinement potential energy and their wave function totally delocalized. Because these delocalized states are involved in our CI calculation, they also contribute to the deviation of binding energy estimation. For our calculation of quantum ring in the next section, all the involved states are strongly confined due to the

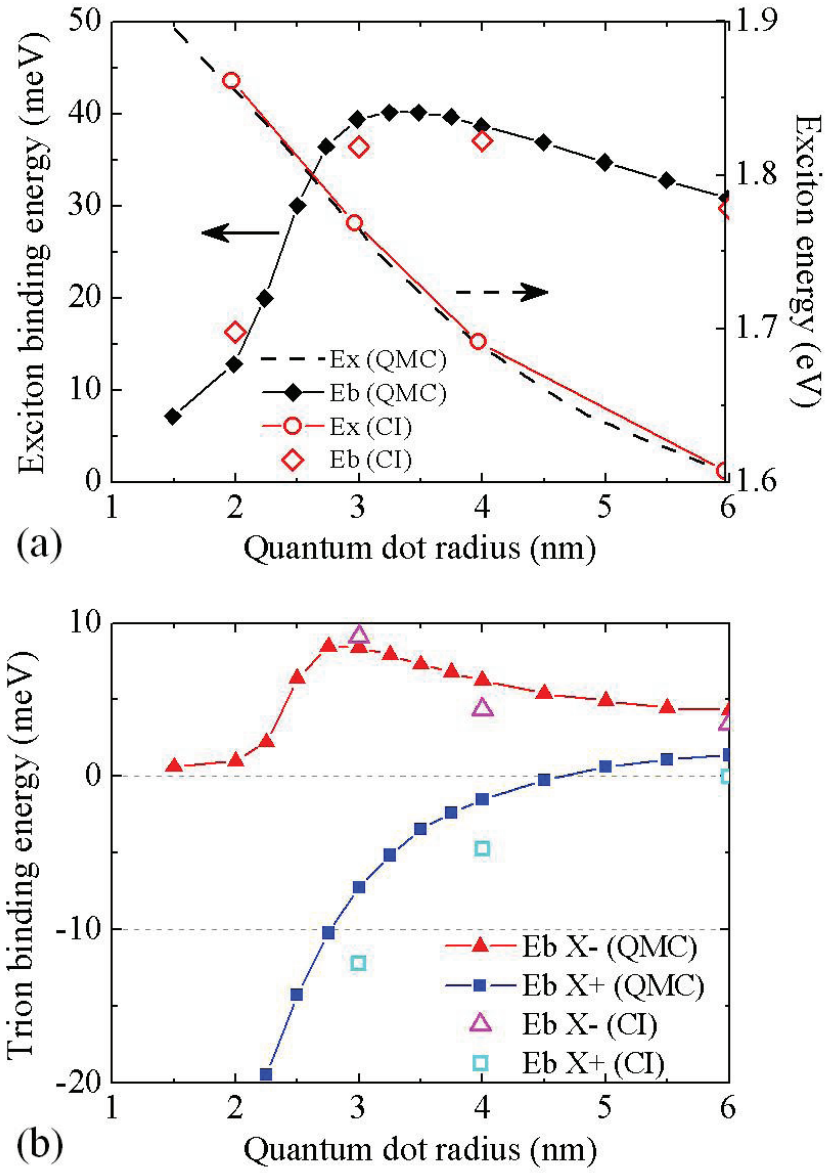


Figure 7.2: Comparison of our configuration interaction (CI) calculation to the published results in Ref. [155] for (a) the energy of the exciton ground state (open circles)and its binding energy (open diamonds) as well as (b) the binding energy of trion states (denoted with the open triangles and the squares for the negative and the positive trion, respectively.) as a function of the radius of a spherical GaAs quantum dot.

large size of quantum ring. Therefore, the underestimation of Coulomb binding energy is small similar to the results of QD with radius of 6 nm in Fig. 7.2.

Figure 7.2(b) shows the comparison of our calculation of the trion binding energy with the published data as a function of the QD radius. Our results correctly reproduced the size dependence of the negative trion binding energy as a function of the decreasing QD radius and showed an agreement with the quantum Monte Carlo calculation results. In a positive trion, the wave functions of the holes concentrate closer to the center of the QD than the electrons due to their small kinetic energy. On the other hand, by decreasing the QD radius, the electron wave functions partially delocalize out of the QD into the barrier layer. With the decreasing QD radius, when the repulsion between holes becomes the dominant interaction in a small QD, the negative binding energy can be found for the positive trion. This feature was correctly reproduced by our calculation, and the size dependence of its binding energy also showed a qualitative agreement with the quantum Monte Carlo calculation. These agreements in the above comparison showed that our CI calculation for the trion state is valid.

Because the CI calculation can take the full correlation interaction into consideration, our present calculation can be extended to include the spin configuration for the study of the exchange interaction.

## 7.4 Aharonov-Bohm effect of exciton complex in quantum rings

By using the same numerical method, the exciton and the negative trion states were calculated for the GaAs quantum ring. Figure 7.3(a) shows the energy of the non-interacting electron-hole pair states with a different combination of angular momentum ($l_e$, $l_h$) in a quantum ring. The energy oscillation and the transition of the total angular momentum from $L = 0$ to $L = 1$ ($L = l_e + l_h$ for two-body system) are found for the lowest pair state. When $B = 20$ T, the lowest pair state ($L = 1$) crosses with the second lowest pair states with $L = 0$ ($l_e = -1$, $l_h = 1$). The different kinetic energies between the electron and the hole lead to the different radius of trajectories when they are both confined in a quantum ring. The magnetic flux piercing through the area between their trajectories introduces the A-B effect that showed a phenomenon of energy oscillation for the ground state.

Figure 7.3(b) shows the energy of the exciton states as a function of the magnetic field. Within the range of magnetic field up to 40 T in the present study, neither the energy oscillation nor the $L$ transition is found for the exciton ground state. Similar to our previous discussion on the vanishing A-B effect in a 2D ring, the reason for the disappearance of the excitonic A-B effect is the strong Coulomb interaction that mixes the low-energy pair states with the same $L$. Consequently, the $B$ dependence of the lowest pair state energy varied, and the A-B effect observed for the non-interacting pair states did not occur for the exciton ground state.

Figure 7.4(a) shows the energy of the non-interacting 3-body basis states as a function of the magnetic field. The total angular momentum of this 3-body basis state is

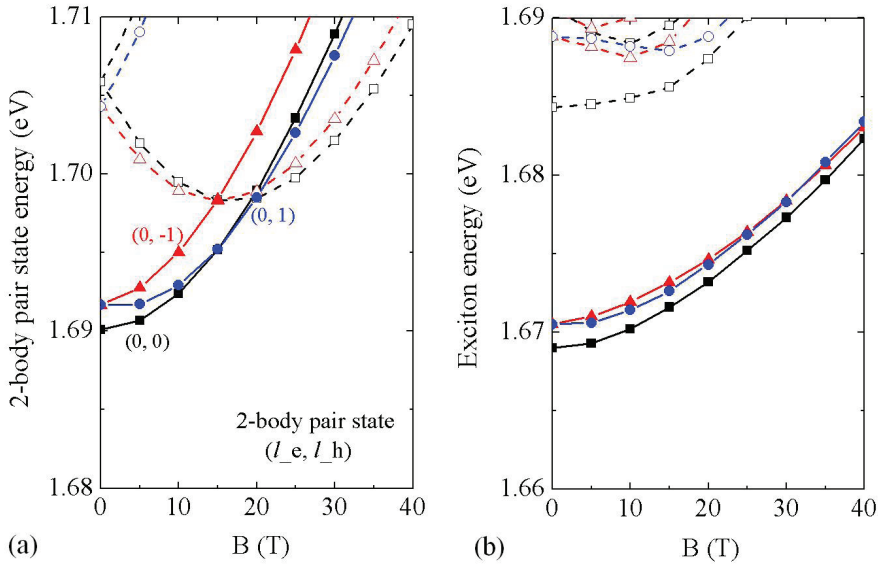


Figure 7.3: The energy of (a) the non-interacting electron-hole pair states and (b) the exciton states in a quantum ring as a function of the magnetic field. The results with total angular momentum $L = l_e + l_h = 0, 1, -1$ are denoted with black squares, blue dots, and red triangles, respectively. For each $L$, the lowest-energy state is plotted with a solid line, and the excited states are plotted with dashed lines. The combination of the electron and the hole angular momentum quantum number ($l_e$ and $l_h$) is denoted for low-energy pair states.

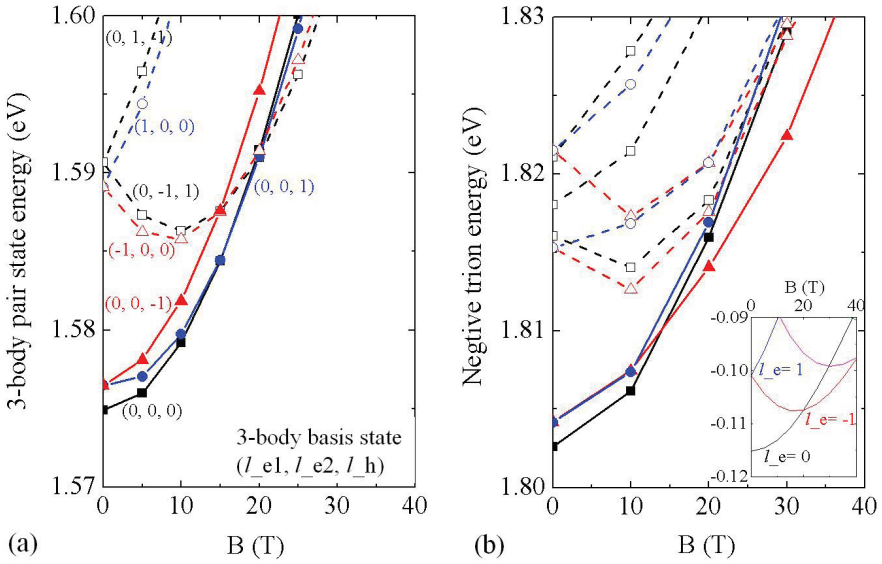


Figure 7.4: The energy of (a) the non-interacting 3-body basis states and (b) the negative trion states in a quantum ring as a function of the magnetic field. The results with total angular momentum $L = l_{e1} + l_{e2} + l_h = 0, 1, -1$ are denoted with black squares, blue dots and red triangles, respectively. For each $L$, the lowest-energy state is plotted with a solid line, and the excited states are plotted with dashed lines. The combination of the electron and the hole angular momentum quantum number ($l_{e1}$, $l_{e2}$ and $l_h$) is denoted for low-energy 3-body basis states. The inset shows the energy of a single electron as a function of the magnetic field in a quantum ring.

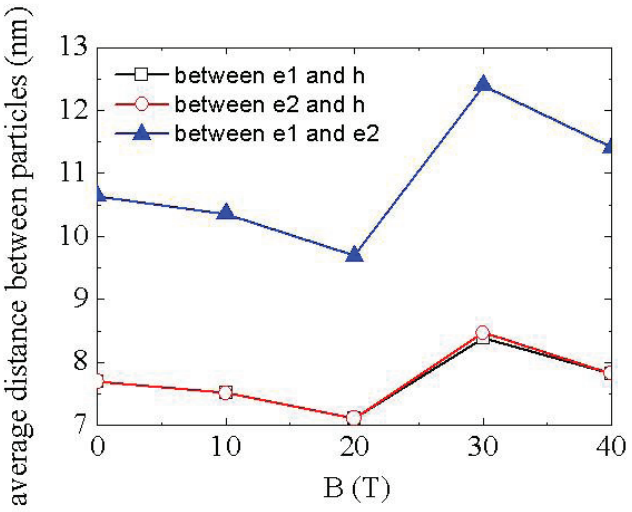


Figure 7.5: The average distances for the electron-electron and the electron-hole in a negative trion with $L = 0$ as a function of the magnetic field.

defined as $L = l_{e1} + l_{e2} + l_h$. The energy oscillation and the $L$ transition are found for the lowest state.

Figure 7.4(b) shows the energy of the negative trion states as a function of the magnetic field. By analyzing the main contributing 3-body basis states for low-energy trions, Coulomb mixing was found. Although the Coulomb mixing between the 3-body basis states is found, a clear energy oscillation can be observed for the trion ground state. When $B \geq 30$ T, the main contribution to the lowest trion state with $L = 0$ varies from the basis with $(l_{e1} = 0, l_{e2} = 0, l_h = 0)$ to that with $(l_{e1} = -1, l_{e2} = 0, l_h = +1)$ and $(l_{e1} = 0, l_{e2} = -1, l_h = +1)$. Similarly when $B \geq 20$ T, the main contribution to the lowest trion state with $L = -1$ varies from the basis with $(l_{e1} = 0, l_{e2} = 0, l_h = -1)$ to that with $(l_{e1} = -1, l_{e2} = -1, l_h = +1)$. The $L$ transition of the trion state takes place at $B = 15$ T, but the $l_e$ transition of the lowest electron state occurs at $B = 20$ T as shown in the inset of Fig. 7.4(b). Considering a dipole-allowed transition between the electron and the hole states with angular momentum $l_e + l_h = 0$, the oscillation behavior can be expected for the emission photon energy. So the disappearance of excitonic A-B effect and the occurrence of the A-B effect for the trion ground state can be verified by the measurement of emission spectra.

Figure 7.5 shows the average distances among the three particles of a negative trion in the quantum ring as a function of the magnetic field. The two electrons and one hole are denoted as e1, e2 and h in this figure, respectively. As we expected, the results for e1-h and e2-h are nearly the same that showed the accuracy of our calculation. Also, the distance between e1-e2 (repulsion) is larger than that for electron-hole attraction as we expected. By increasing the magnetic field from 0 to 20 T, the distances for both the electron-electron and the electron-hole decrease because the magnetic field introduced potential pushes the electrons and the hole towards the center of the system that leads to the increasing wave function overlap between the particles. Between $B = 20$ T and 30 T, the average distances

increase because of the Coulomb mixing between the 3-body basis. The main contributing 3-body basis state of the lowest exciton with $L = 0$ varies from $(l_{e1} = 0, l_{e2} = 0, l_h = 0)$ to $(l_{e1} = -1, l_{e2} = 0, l_h = +1)$ and $(l_{e1} = 0, l_{e2} = -1, l_h = +1)$. The wave functions of the electron and the hole with nonzero $l_e$ and $l_h$ distribute further from the center than that for $l_e = 0$ and $l_h = 0$. Therefore, the change of the main contributing 3-body basis state leads to larger inter-particle distance. The increasing behavior of the average distance as a function of the magnetic field is an evidence of the existence of the Coulomb mixing in the negative trion state.

## 7.5 Conclusion

With the configuration interaction method, we calculated the size-dependent binding energy of the exciton states and the trion states of a spherical quantum dot in the cylindrical coordinates. Our calculation results showed a good agreement with the reported results calculated by the quantum Monte Carlo method that verified the validity of our calculation method.

Using the same method, we calculated the influence of the magnetic field on the exciton states and the negative trion (composed of two CB electrons and one VB hole) states in a quantum ring. The A-B effect was not found for the exciton ground state because the Coulomb interaction mixed the pair states with the same total angular momentum and changed the magnetic field dependence of their energy. On the other hand, even with the Coulomb mixing, the A-B effect was found for the negative trion ground state. This observation indicates the fact that the magnetic field response of a negative trion is similar to the negatively charged particle (electron) in a quantum ring. The emitted photon energy of the negative trion ground state can show an oscillation behavior as a function of the magnetic field, which can be verified by the measurement of emission spectra. To the best of our knowledge, our study is the first theoretical investigation of the influence of the magnetic field on the trion states in a 3D quantum ring model. The present study can be extended to the trion and the biexciton systems in the nanostructures with complicated geometries.

# Chapter 8:

# Dirac cones in the Brillouin-zone center of periodically modulated quantum wells

## 8.1 Background: Dirac cones in photonic crystals

The formation of Dirac-cone in the photonic crystal was revealed on the Γ point (Brillouin-zone center) [85–89]. The essence of the photonic Dirac-cone formation by accidental degeneracy of two modes is the particular combination of the spatial symmetry of their wave functions [87–89]. Its general proof for arbitrary periodic optical media was given by the $\mathbf{k} \cdot \mathbf{p}$ perturbation theory combined with the group theory [87, 88]. We can expect novel phenomena that are peculiar to photonic Dirac cones like the continuous control of the propagation direction of Dirac-cone modes in photonic crystal slabs by the polarization of the incident wave [89].

Because the presence of the photonic Dirac cone on the Γ point is purely a consequence of particular combinations of mode symmetries, Dirac cones are expected to be materialized not only in photonic structures but also in any wave systems including electron, phonon, and exciton systems. In this chapter, we demonstrated that by introducing periodic external potentials into a quantum well system, the Dirac cone formation can be realized on the Γ point of the electron band structure. For the Schrödinger equation with a scalar electron wave function, the formulations are similar to those of photonic Dirac cones. Our numerical calculation confirm the prediction of the Dirac cones and double Dirac cones in the modulated quantum well with square and triangular lattices, respectively.

## 8.2 $\mathbf{k} \cdot \mathbf{p}$ perturbation theory for Dirac cones in modulated quantum wells

We apply the $\mathbf{k}\cdot\mathbf{p}$ perturbation theory and the group theory to the problem of the formation of Dirac cones in the Brillouin-zone center of the electronic bands of quantum wells by accidental degeneracy of two subbands. To clearly demonstrate the principle of Dirac-cone formation, we deal with the simplest case in this paper, that is, we assume that the electronic system can be described by the time-independent one-component Schrödinger equation:

$$\hat{\mathcal{H}}\psi_{\mathbf{k}n} \equiv \left( -\frac{\hbar^2}{2m} \bigtriangledown^2 + U \right) \psi_{\mathbf{k}n} = E_{\mathbf{k}n}\psi_{\mathbf{k}n}, \tag{8.1}$$

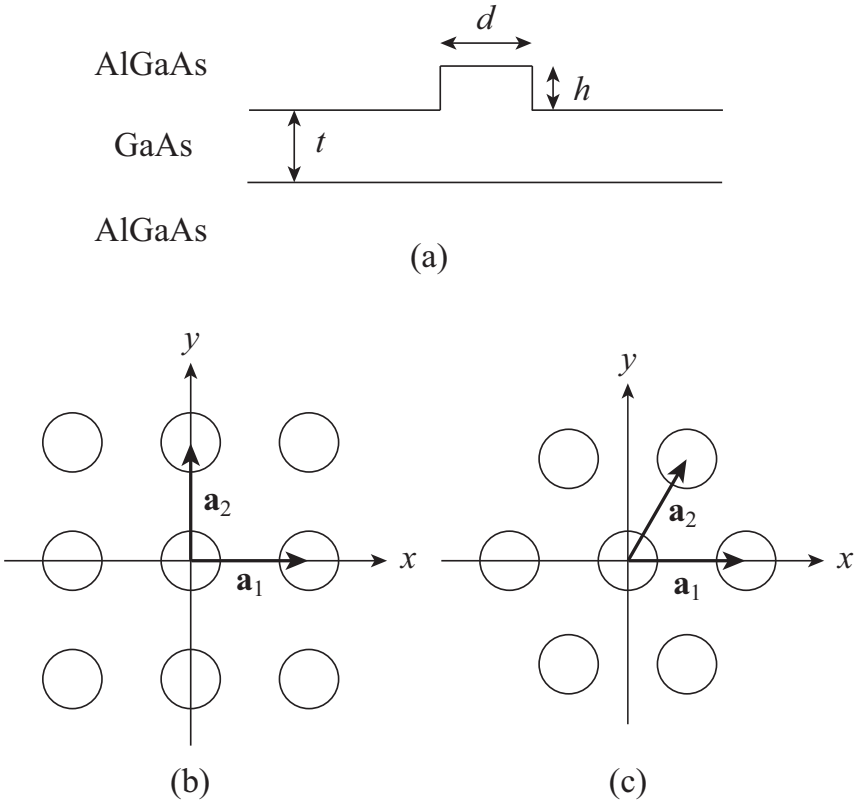


Figure 8.1: (a) Side view of a periodically modulated quantum well composed of GaAs and AlGaAs layers with a cylindrical bump in each unit structure. Top view of the quantum wells with the (b) square and (c) triangular structural modulations [156].

where $m$ is the electron effective mass, $\mathbf{k}$ is the wave vector in the two-dimensional Brillouin zone, $n$ is the band index, and $U$ is the confinement potential in the periodically modulated quantum well. So, we assume

$$U(\mathbf{r}+\mathbf{a}_i) = U(\mathbf{r}) \qquad (i=1,\ 2), \tag{8.2}$$

where $\mathbf{a}_i$ is the two-dimensional elementary lattice vector of the periodical modulation (See Fig. 8.1). From the Bloch theorem, $\psi_{\mathbf{k}n}$ is

$$\psi_{\mathbf{k}n}(\mathbf{r}) = e^{i\mathbf{k}\cdot\mathbf{r}} u_{\mathbf{k}n}(\mathbf{r}), \tag{8.3}$$

where $u_{\mathbf{k}n}(\mathbf{r})$ is a periodic function:

$$u_{\mathbf{k}n}(\mathbf{r}+\mathbf{a}_i) = u_{\mathbf{k}n}(\mathbf{r}). \tag{8.4}$$

We normalize the eigen functions as

$$\langle \psi_{\mathbf{k}n} | \psi_{\mathbf{k}'n'} \rangle \equiv \frac{1}{V}\int_V d\mathbf{r}\psi_{\mathbf{k}n}(\mathbf{r})^* \psi_{\mathbf{k}'n'}(\mathbf{r}) = \delta_{\mathbf{k}\mathbf{k}'}\delta_{nn'}, \tag{8.5}$$

where $V$ is the volume on which we impose the periodic boundary condition and $\delta$ is Kronecker's delta. Then $u_{\mathbf{k}n}$ is an eigen function of operator $\hat{\mathcal{H}}_{\mathbf{k}}$ defined by

$$\hat{\mathcal{H}}_{\mathbf{k}} \equiv e^{-i\mathbf{k}\cdot\mathbf{r}} \hat{\mathcal{H}} e^{i\mathbf{k}\cdot\mathbf{r}}, \tag{8.6}$$

which is a Hermitian operator in the Hilbert space of complex functions with the lattice-translation symmetry. So, $\{u_{\mathbf{k}n}|\ n=1,2,\cdots\}$ is a complete set for each $\mathbf{k}$. We normalize them as

$$\langle u_{\mathbf{k}n} | u_{\mathbf{k}n'} \rangle_0 \equiv \frac{1}{V_0}\int_{V_0} d\mathbf{r} u^*_{\mathbf{k}n}(\mathbf{r})\cdot u_{\mathbf{k}n'}(\mathbf{r}) = \delta_{nn'}, \tag{8.7}$$

where $V_0$ denotes the volume of the unit cell defined by $\mathbf{a_1}$ and $\mathbf{a_2}$. Thus, in particular, for $\mathbf{k}=0$,

$$\{u_{0n}|\ n=1,2,\cdots\} \tag{8.8}$$

is an orthonormal complete set. Therefore, we can express any eigen function $u_{\mathbf{k}l}$ of operator $\hat{\mathcal{H}}_{\mathbf{k}}$ by a linear combination of eigen functions $\{u_{0n}\}$ of operator $\hat{\mathcal{H}}_0$. Thus, for small $\mathbf{k}$ in the vicinity of the $\Gamma$ point, we can calculate $E_{\mathbf{k}l}$ perturbatively using $\{u_{0n}\}$ as a basis set. Because we are interested only in the presence or absence of terms linear in $\mathbf{k}$, we neglect the quadratic term of the perturbation operator:

$$\Delta\hat{\mathcal{H}}_{\mathbf{k}} \equiv \hat{\mathcal{H}}_{\mathbf{k}} - \hat{\mathcal{H}}_0 \approx \frac{\hbar}{m}\mathbf{k}\cdot\hat{\mathbf{p}}, \tag{8.9}$$

where $\hat{\mathbf{p}}$ is the momentum operator. We assume according to the situation of our problem that $\{u_{0l}|\ l=1,2,\cdots,M\}$ are degenerate and denote their eigenvalue by $E_0$. By the degenerate perturbation theory, the first-order solution for $u_{\mathbf{k}l}$ $(l=1,2,\cdots,M)$ is obtained

by diagonalizing the matrix whose $ij(1 \le i, j \le M)$ element is given by

$$C_{ij}^{(\mathbf{k})} \equiv \langle u_{0i}|\Delta\hat{\mathcal{H}}_{\mathbf{k}}|u_{0j}\rangle_0 = \frac{\hbar}{m}\mathbf{k}\cdot\mathbf{p}_{ij}, \tag{8.10}$$

which can bring about eigenvalue corrections linear in $\mathbf{k}$. Thus, our problem on the creation of Dirac cones is reduced to examining whether the eigenvalues of matrix $\mathrm{C}^{(\mathbf{k})} = (C_{ij}^{(\mathbf{k})})$ are non-zero. If all of its eigenvalues are equal to zero, the energy correction starts with terms of the second order of $\mathbf{k}$, so the Dirac cone does not exist.

For this purpose, we examine $\mathrm{C}^{(\mathbf{k})}$ using the spatial symmetry of $\{u_{0l}\}$. We assume that the periodic structure that we deal with is invariant by symmetry operations of point group $\mathcal{G}$. We denote the symmetry operation and its matrix representation by $\mathcal{R}$ and R, respectively. First, we should note that

$$\mathrm{R}^t = \mathrm{R}^{-1} \quad \text{and} \quad \det \mathrm{R} = \pm 1 \tag{8.11}$$

since R is an orthogonal matrix. Second, we can easily prove that the momentum operator commutes with $\mathcal{R}$:

$$\mathcal{R}\hat{\mathbf{p}}\mathcal{R}^{-1} = \hat{\mathbf{p}}. \tag{8.12}$$

Next, by introducing three pairs of $\mathcal{R}^{-1}\mathcal{R}$ (= identity operator) to the definition of $C_{ij}^{(\mathbf{k})}$, we obtain

$$\begin{aligned}
C_{ij}^{(\mathbf{k})} &= \frac{\hbar\mathbf{k}}{mV_0}\cdot\int_{V_0} d\mathbf{r}\mathcal{R}^{-1}\mathcal{R}u_{0i}^*(\mathbf{r})\mathcal{R}^{-1}\mathcal{R}\hat{\mathbf{p}}\mathcal{R}^{-1}\mathcal{R}u_{0j}(\mathbf{r}) \\
&= \frac{\hbar\mathbf{k}}{mV_0}\cdot\int_{V_0} d\mathbf{r}\mathcal{R}^{-1}[\mathcal{R}u_{0i}^*](\mathbf{r})\hat{\mathbf{p}}[\mathcal{R}u_{0j}](\mathbf{r}) \\
&= \frac{\hbar\mathbf{k}}{mV_0}\cdot\mathrm{R}^{-1}\int_{V_0} d(\mathrm{R}\mathbf{r})[\mathcal{R}u_{0i}^*](\mathrm{R}\mathbf{r})\hat{\mathbf{p}}'[\mathcal{R}u_{0j}](\mathrm{R}\mathbf{r}) \\
&= \frac{\hbar(\mathrm{R}\mathbf{k})}{mV_0}\cdot\int_{V_0} d\mathbf{r}'[\mathcal{R}u_{0i}^*](\mathbf{r}')\hat{\mathbf{p}}'[\mathcal{R}u_{0j}](\mathbf{r}') \\
&= \frac{\hbar}{m}(\mathrm{R}\mathbf{k})\cdot\langle\mathcal{R}u_{0i}|\hat{\mathbf{p}}|\mathcal{R}u_{0j}\rangle_0,
\end{aligned} \tag{8.13}$$

where the prime denotes $\mathbf{r}' = \mathrm{R}\mathbf{r}$ and by definition,

$$[\mathcal{R}u_{0i}](\mathbf{r}) \equiv u_{0i}(\mathrm{R}^{-1}\mathbf{r}). \tag{8.14}$$

In Eq. (8.13), we used the fact that R does not change the size of the volume element, since it is an orthogonal matrix.

So, unless the product of $\mathbf{k}$, $u_{0i}$, and $u_{0j}$ contains a term invariant for all $\mathcal{R} \in \mathcal{G}$, $C_{ij}^{(\mathbf{k})}$ vanishes. In this case, the linear term is absent in the dispersion curve around the $\Gamma$ point, so Dirac cones do not exist. Therefore, the presence of an invariant term, or the totally symmetric representation, in the above-mentioned product is a distinct necessary condition for the Dirac cone. In addition, we can derive many relations among different matrix elements by using Eq. (8.13). These relations determine the structure of matrix $\mathrm{C}^{(\mathbf{k})}$ nearly uniquely, from which we can obtain the shapes of the dispersion curves

Table 8.1: Types of dispersion curves generated by accidental degeneracy of two modes (Mode 1 and Mode 2). Only those symmetry combinations which generate Dirac cones are listed. Shapes of the dispersion curves are given in the right column, where D, DD, and Q denote Dirac cone, double Dirac cones, and quadratic dispersion surface, respectively [156].

| Lattice symmetry | Mode 1 | Mode 2 | Dispersion |
|---|---|---|---|
| $C_{4v}$ | $E$ | $A_1$, $A_2$, $B_1$, $B_2$ | D + Q |
| $C_{6v}$ | $E_1$ | $E_2$ | DD |
| | $E_1$ | $A_1$, $A_2$ | D + Q |
| | $E_2$ | $B_1$, $B_2$ | D + Q |

analytically. We examine two examples in the following.

First, we examine the case of the square array of the cylindrical bumps (Fig. 8.1(b)). The system has the $\mathcal{C}_{4v}$ symmetry, so $u_{0l}$ are irreducible representations of the $\mathcal{C}_{4v}$ point group. We can easily verify that wave vector $\mathbf{k}$, which is a linear combination of unit vectors in the $x$ and $y$ directions, is transformed as an $E$ representation of the $\mathcal{C}_{4v}$ group by symmetry operations. From the standard reduction procedure [117], we can conclude that only a limited number of the combinations of the mode symmetries contains a totally symmetric representation and lead to non-zero $\mathrm{C}^{(\mathbf{k})}$. Those combinations are listed in Table I.

According to Ref. [88], for the combination of an $E$ mode and an $A_1$ mode, matrix $\mathrm{C}^{(\mathbf{k})}$ has the following structure:

$$\mathrm{C}^{(\mathbf{k})} = \begin{pmatrix} 0 & 0 & bk_x \\ 0 & 0 & bk_y \\ b^*k_x & b^*k_y & 0 \end{pmatrix}, \tag{8.15}$$

where the first and the second rows/columns are relevant to the $E$ mode and the third row/column are relevant to the $A_1$ mode. Without loss of generality, we assumed that the two wave functions ($u_E^{(1)}$ and $u_E^{(2)}$) of the $E$ mode were transformed like the $x$ and $y$ coordinates by symmetry operations, respectively [117]. In Eq. (8.15),

$$b = \frac{\hbar}{m}\langle u_E^{(1)}|\hat{p}_x|u_{A_1}\rangle. \tag{8.16}$$

Similar to Eq. (8.13), we have the following relation,

$$\begin{aligned} \frac{\hbar}{m}\langle u_E^{(1)}|\hat{\mathbf{p}}|u_{A_1}\rangle &= \frac{\hbar}{m}\int_{V_0} d\mathbf{r}\mathcal{R}_{C_4}^{-1}\mathcal{R}_{C_4}u_E^{(1)}(\mathbf{r})\mathcal{R}_{C_4}^{-1}\mathcal{R}_{C_4}\hat{\mathbf{p}}\mathcal{R}_{C_4}^{-1}\mathcal{R}_{C_4}u_{A1}(\mathbf{r}) \\ &= \frac{\hbar}{m}\mathrm{R}_{C_4}^{-1}\int_{V_0} d\mathbf{r}'[u_E^{(2)}](\mathbf{r}')\hat{\mathbf{p}}'[u_{A1}](\mathbf{r}') \end{aligned}$$

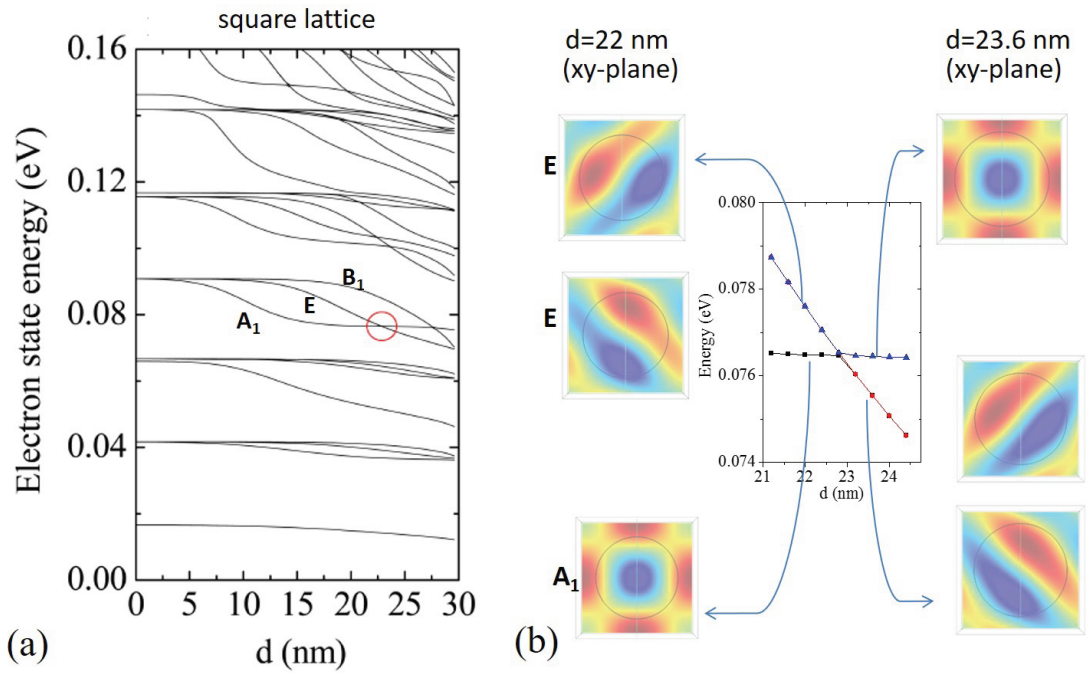


Figure 8.2: (a) Energy bands on the Γ point of the periodically modulated GaAs/AlGaAs quantum well (square lattice, $a = 30$ nm, $t = 15$ nm, $h = 6$ nm) as a function of the diameter of the cylindrical bump. The accidental degeneracy is marked with a red circle. (b) Magnified energy band structure around the degeneracy point in the left figure with a red circle. The electron wave functions (in xy-plane) of the involved bands are also plotted before and after the accidental degeneracy.

$$= \frac{\hbar}{m} \mathrm{R}_{C_4}^{-1} \langle u_E^{(2)} | \hat{\mathbf{p}} | u_{A_1} \rangle. \tag{8.17}$$

Furthermore, we have,

$$\frac{\hbar}{m} \langle u_E^{(1)} | \hat{p}_x | u_{A_1} \rangle = \frac{\hbar}{m} \langle u_E^{(2)} | \hat{p}_y | u_{A_1} \rangle. \tag{8.18}$$

By solving the secular equation, we can obtain the energy correction, $\Delta E$:

$$\Delta E = \pm |b| k, \quad 0. \tag{8.19}$$

where $k = \sqrt{{k_x}^2 + {k_y}^2}$. Therefore, two of the three dispersion curves compose an isotropic Dirac cone. For the third mode, the linear term is absent, so the dispersion curve starts with a quadratic term. For other mode combinations listed in Table 8.1, we can also prove that the dispersion relation consists of an isotropic Dirac cone and an auxiliary quadratic dispersion surface.

To check the analytical result, we calculated the band structure by the finite element method. A 3D model was built according to one unit cell of the present periodic structure. As shown in Fig. 8.2(a), the energy bands on the Γ point of the periodically modulated quantum well of the square lattice were plotted as a function of the diameter of the

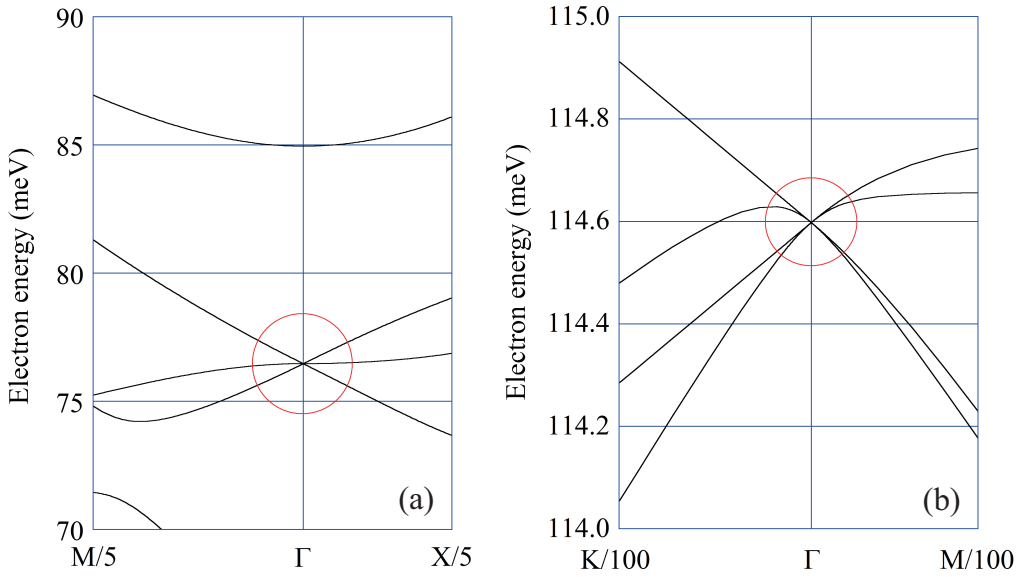


Figure 8.3: Energy bands of the periodically modulated GaAs/AlGaAs quantum well. (a) Square lattice with $|\mathbf{a}_i| \equiv a = 30$ nm, $t = 15$ nm, $h = 6$ nm, and $d = 22.8$ nm. (b) Triangular lattice with $a = 30$ nm, $t = 15$ nm, $h = 6$ nm, and $d = 20.55$ nm. The vertical axis is the electron energy measured from the bottom of the GaAs conduction band. The horizontal axis is the wave vector in the two-dimensional Brillouin zone, where $\mathrm{X} = (\pi/a, 0)$ and $\mathrm{M} = (\pi/a, \pi/a)$ for the square lattice and $\mathrm{K} = (4\pi/(3a), 0)$ and $\mathrm{M} = (\pi/a, -\pi/(\sqrt{3}a))$ for the triangular lattice. X/5, for example, means that the horizontal axis is magnified by five times [156].

cylindrical bump ($d$). By tuning $d$, an accidental degeneracy of bands was found as marked with a red circle. By examining the electron wave function of the involved bands before and after the accidental degeneracy, we can assign the involved three bands to an $A_1$ mode and a doubly degenerated $E$ mode. For the case of the accidental degeneracy of an $E$ mode and an $A_1$ mode, which was materialized with structural parameters listed in the caption of Fig. 8.3(a), we confirmed the formation of a Dirac cone with a quadratic dispersion surface.

Next, we examine the two-dimensional triangular lattice of the $C_{6v}$ symmetry (Fig. 8.1(c)). The symmetry combinations that generate non-zero $\mathrm{C}^{(\mathbf{k})}$ for this case are also listed in Table I. One particular feature of the $C_{6v}$ point group is that it has two different doubly degenerate eigenmodes, $E_1$ and $E_2$. By the accidental degeneracy, they materialize double Dirac cones. For the $C_{6v}$ symmetry, the wave vector $\mathbf{k}$ is transformed as an $E_1$ representation.

Without loss of generality, we can assume that the two eigen functions of the $E_1$ mode ($\mathbf{u}_{E_1}^{(1)}$, $\mathbf{u}_{E_1}^{(2)}$) are transformed like the $x$ and $y$ coordinates, whereas those of the $E_2$ mode ($\mathbf{u}_{E_2}^{(1)}$, $\mathbf{u}_{E_2}^{(2)}$) are transformed like $2xy$ and $x^2 - y^2$ [117]. According to Ref. [88], we can prove that the $\mathrm{C}^{(\mathbf{k})}$ has the following form.

$$\mathrm{C}^{(\mathbf{k})} = \begin{pmatrix} 0 & 0 & -bk_y & -bk_x \\ 0 & 0 & -bk_x & bk_y \\ -b^*k_y & -b^*k_x & 0 & 0 \\ -b^*k_x & b^*k_y & 0 & 0 \end{pmatrix}, \tag{8.20}$$

where

$$b = \frac{\hbar}{m}\langle \mathbf{u}_{E_1}^{(2)} | \hat{p}_y | \mathbf{u}_{E_2}^{(2)} \rangle \tag{8.21}$$

The secular equation can be solved easily and its solutions are given by

$$\Delta E = \pm |b| k \quad (\textit{double roots}). \tag{8.22}$$

So, we have isotropic double Dirac cones with the same slope. This analytical result can also be confirmed by numerical calculation. In Fig. 8.4(a), the energy bands on the $\Gamma$ point of the periodically modulated quantum well of the triangular lattice were plotted as a function of the diameter of the cylindrical bump ($d$). By tuning $d$, an accidental degeneracy of bands was found as marked with a red circle. By examine the electron wave function of the four involved bands in this area before and after the accidental degeneracy, we can assign these bands to the doubly degenerated $E_1$ and $E_2$ modes. As shown in Fig. 8.3(b), the ranges of the electron energy and the wave vector where the linear $k$ dependence is observed are much limited compared with Fig. 8.3(a), since there is a dense distribution of other electronic bands above and below the double Dirac cones, which bring about complicated mutual repulsion among the electronic bands to yield deformation from the linear $k$ dependence easily.

When we compare Eq. (8.13) with Eq. (22) of Ref. [88], we notice that the transfor-

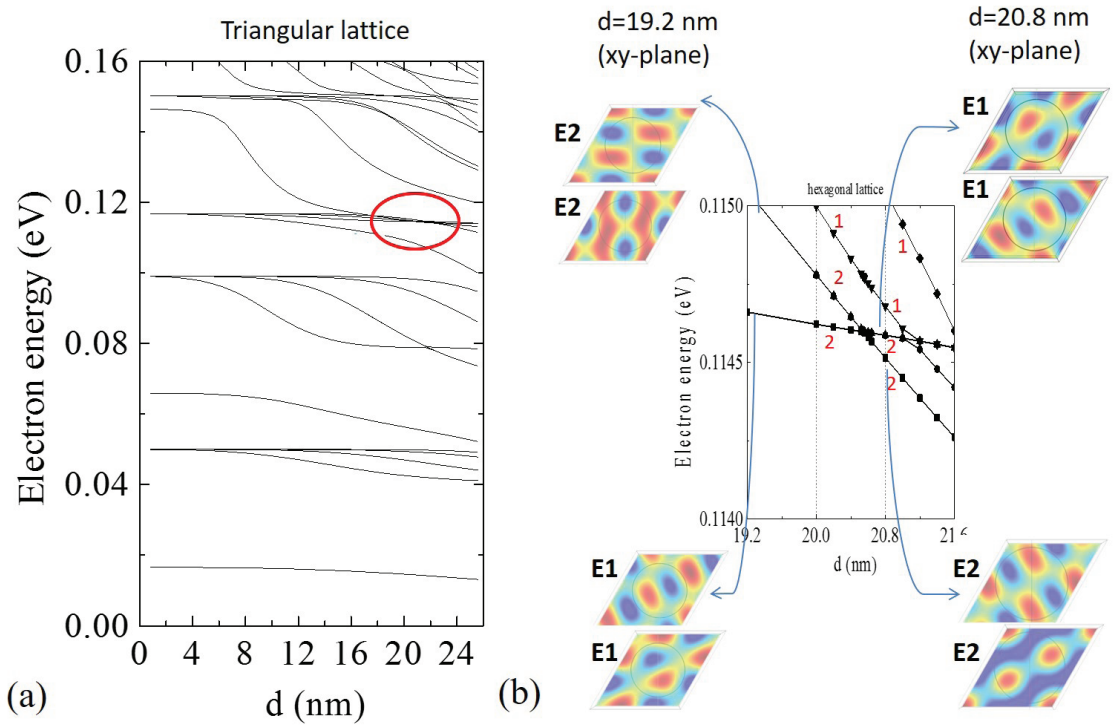


Figure 8.4: (a) Energy bands at Γ point of the periodically modulated GaAs/AlGaAs quantum well (triangular lattice, $a = 30$ nm, $t = 15$ nm, $h = 6$ nm) as a function of the diameter of the cylindrical bump. The accidental degeneracy was marked with a red circle. (b) Magnified energy band structure around the degeneracy point in the left figure with a red circle. The electron wave functions (in xy-plane) of the involved bands are also plotted before and after the accidental degeneracy. The degeneracy of the bands is denoted by numbers in red color.

mation property of the first-order perturbation matrix is the same for the present problem of the electronic bands and the electromagnetic dispersion curves. Thus the combination of mode symmetries that materialize the Dirac cones are also the same, which was confirmed by analytical and numerical calculations in this chapter. We can extend this observation to all other harmonic waves. So we can materialize Dirac cones on the Γ point for any harmonic wave systems by accidental degeneracy.

In the actual specimen fabrication, however, the probability of exact degeneracy by adjusting the specimen parameters is negligibly small, so there is always an energy mismatch between the two states, although it may be small. When we denote the energy mismatch by $\alpha$ and place it in the (3, 3) element of $\mathrm{C}^{(\mathbf{k})}$ in Eq. (8.15), we obtain the following energy correction.

$$\Delta E = \frac{\alpha \pm \sqrt{a^2 + 4|b|^2 k^2}}{2}. \tag{8.23}$$

This more realistic energy dispersion brings about a small effective mass $m^*$, which is obtained by the second derivative of $\Delta E$ with respect to $k$:

$$m^* = \frac{|\alpha|\hbar^2}{2|b|^2}. \tag{8.24}$$

So, the effective mass vanishes when the energy mismatch becomes infinitesimally small. This phenomenon further brings about a large electron mobility, which is inversely proportional to the effective mass, if the introduction of the periodic modulation does not affect the electron relaxation time.

## 8.3 Conclusion

We applied the $\mathbf{k}\cdot\mathbf{p}$ perturbation and group theory to the problem of the formation of Dirac cones by accidental degeneracy on the Γ point of periodically modulated quantum wells. The structure of the perturbation matrix that gave the first-order energy correction was determined by the symmetry of the relevant electronic states, which enabled us to obtain the energy dispersion by analytical calculation. We found the formation of Dirac cones for the square lattice and Dirac cones and double Dirac cones for the triangular lattice, which was also confirmed by numerical calculation by the finite element method.

# Chapter 9:

# Conclusion and outlook

With the developing synthesis technologies, new nanostructures with complex geometries have been successfully fabricated. Their electronic and optical properties are critically influenced by the geometries and may become new platforms for the fundamental studies and application fields. To explain the experimental observation and predict the electronic properties of these nanostructures, we calculated the electronic and excitonic structures by combining the analytical and numerical calculation methods. The finite element method was used for an efficient approach to the complex geometries. The exciton states of the nanostructure and corresponding heterostructure were systematically investigated by the configuration interaction method. The influence of the external electric and magnetic fields on the exciton states and the trion states was investigated as well. The main findings were summarized as follows:

(1) In the present thesis, the tetrapod-shaped nanostructures consist of a central core and four branches at tetrahedral angles. By using the group theory, we found that the low-energy single particle states and the exciton states of the tetrapod-shaped nanostructures have $A_1$ and $T_2$ symmetry. Because the lowest spin-singlet excitons have $A_1$ symmetry, they are optically active and luminescent. Even when it is of $T_2$ symmetry, because the energy difference between the lowest $T_2$ exciton and $A_1$ exciton is much smaller than the room-temperature thermal energy, we suppose that the tetrapod-shaped nanostructures can be luminescent. We investigated the influence of geometrical parameters, materials and the crystal structure of the branches on the low-energy exciton states and the absorption spectra. We predicted the size effect on the energy of the absorption peaks, which showed a good agreement with the available experimental data. For the tetrapods with large branch width, the lowest absorption peaks with small intensity were revealed, which is difficult to be observed in the experimental study.

(2) The core-shell tetrapod-shaped heterostructures have shells covering the lateral surface of the branches (arms) of a tetrapod. Those heterostructures composed of a CdTe tetrapod and CdS shells possess type-II band structure. We analyzed the symmetry of their electronic states and investigated the influence of strain on the exciton states. Our results showed a good agreement with the energy of the photoluminescence peaks observed in the experiment. We found that the strain promotes the type-II band structure of the CdTe/CdS tetrapod-shaped heterostructures. With increasing shell thickness, electrons and holes were confined in the non-adjacent regions of the core-shell tetrapod-shaped heterostructure. Accordingly, a more efficient charge separation is realized compared with the type-II spherical core-shell QD. The core-shell tetrapod-shaped heterostructures with broken symmetry were also investigated. We revealed that electrons and holes were confined in the same or different branches by manipulating the randomness. Consequently,

we found the charge separation induced by the randomness, which is unique to branched core-shell heterostructures. Since the low-energy electron and hole are mainly localized in the "arm+shell" regions, the lowest absorption peak of the broken-symmetry structure can be represented by the sum of spectra of individual "arm+shell" regions.

(3) Ring-shaped nanostructures offer a new platform to investigate the Aharonov-Bohm effect (A-B effect) using spectroscopic techniques. But the oscillation signature of the excitonic A-B effect in the single quantum rings is not significant in both the experimental and theoretical results. To clarify the reason for this weak A-B effect, we initially investigated the excitonic A-B effect of a single GaAs quantum ring. With the perturbation theory, the analytical solution of the single particle state was obtained, which showed a good agreement with the numerical calculation with the finite element method and confirmed the validity of our numerical model with cylindrical symmetry. The influence of the magnetic field on the exciton state and negatively charged exciton state (trion) was calculated with the configuration interaction method. The vanishing excitonic A-B effect in the single quantum rings was ascribed to the Coulomb interaction that mixes the wave functions of the low-energy pair states with the same total angular momentum and modifies the magnetic-field dependence of the exciton energy. With the strong Coulomb interaction, the excitonic A-B effect is not significant for the exciton ground state, but it can be found obviously for the trion ground state because of the non-zero total charge of the trion. To the best of our knowledge, our study is the first investigation of the trion A-B effect in a 3D quantum ring. To observe a clear A-B effect, we proposed to use the QD-ring coupled nanostructures with applied electric field along the alignment direction of the components. With the applied electric field, we can simultaneously achieve the partial separation of the electron and hole wave functions to reduce the Coulomb mixing and the control of the average radius of their trajectories to enhance the A-B effect. According to our calculation results, an obvious excitonic A-B effect can be observed with moderate experimental conditions and supposed to be verified by the experimental measurement of the change of the emission spectrum intensity.

(4) The Dirac cones in the photonic crystal were characterized by their isotropic linear dispersion. Recent theoretical investigations revealed the nature of photonic Dirac cone formation. In addition to the photonic crystal, the Dirac cones can be expected for other wave systems according to the same rule of wave function symmetry. By using the $k \cdot p$ perturbation theory and the group theory, we judged the formation of Dirac cones in the vicinity of the $\Gamma$ point for periodically modulated quantum wells. The necessary combinations of wave function symmetry were revealed for quantum wells with the square-lattice and triangular-lattice modulation. The prediction of Dirac cone formation in these two kinds of quantum wells was confirmed by numerical calculation by the finite element method.

By combining the group theory and configuration interaction method, we revealed the influence of shape symmetry of II-VI and III-V nanostructures on their electronic and optical properties. The quantum size effect of our calculation results showed a good agreement with the published experimental data, thus they can be used to explain the experimental observation. Moreover, our calculation predicted the electronic and opti-

cal properties of new nanostructures such as the excitonic A-B effect in the ring-shaped coupled nanostructure and the Dirac cones in the periodically modulated quantum wells. These results offer guidelines and reference information for the future experimental investigations.

Since we are mainly interested in the lowest transition energy in the present studies, we concentrate on the single-band calculation of the conduction band electrons and valence band heavy holes. When the influence of the light hole is non-negligible, multi-band calculation is necessary. We are accumulating the experience of multi-band calculation from simple 2D nanostructures (published recently as: N.N. Schlenskaya, Y. Yao et al. Chem. Mater. vol.29, pp.579-586, 2017) and valence band hole states mixing of a GaAs quantum ring in a magnetic field. Because the multi-band calculation is basically a group of partial differential equations, our present study can be extended to the multi-band calculation for the nanostructures with complicated geometries.

Appendix A: calculation of the single particle state in a ring-shaped structure

## A.1 Single particle state in a 2D ring

In the polar coordinates $(r, \theta)$, the conventional single particle wave function can be assumed as $\varphi_{nl} = e^{il\theta} f_{nl}(r)/\sqrt{2\pi}$ for $B = 0$ with the angular momentum quantum number $l$ and the radial quantum number $n$. $f(r)$ is the radial component of the single particle wave function. The radial-direction Schrödinger equation of a single particle state confined to a 2D ring with the inner radius $(R_1)$ and outer radius $(R_2)$ is:

$$\left\{ -\frac{\hbar^2}{2m^*} \left[ \frac{1}{r}\frac{\partial}{\partial r}\left(\frac{1}{r}\frac{\partial}{\partial r}\right) - \left(\frac{l}{r}\right)^2 \right] + V(r) - E_{nl} \right\} f_{nl}(r) = 0, \tag{A.1}$$

where $E_{nl}$ is the energy of the single particle state, $m^*$ is the effective mass, which is different for the ring $(m_1^*)$ and the barrier layer $(m_2^*)$. The solution of the differential equation in Eq.(A.1) is given by [157]:

$$f_{nl}(r) = \begin{cases} C_3 I_{|l|}(\lambda_2 r) & r < R_1 \\ C_1 J_{|l|}(\lambda_1 r) + C_2 Y_{|l|}(\lambda_1 r) & R_1 \le r \le R_2 \\ C_4 K_{|l|}(\lambda_2 r) & R_2 \le r \end{cases} \tag{A.2}$$

where $C_1, C_2, C_3, C_4$ are the normalization coefficients. $\lambda_1 = \sqrt{2m^* E_{nl}}/\hbar$, $\lambda_2 = \sqrt{2m^*(V(r) - E_{nl})}/\hbar$. $J_{|l|}$ and $Y_{|l|}$ are the Bessel function of the first and second kind. $I_{|l|}$ and $K_{|l|}$ are the modified Bessel function of the first and second kind.

By using the boundary condition of the continuity of the wave function and its first-order derivative at $R_1$ and $R_2$, the eigen energy and the wave function can be obtained by solving a secular equation $|G| = 0$. $G$ is given by

$$G = \begin{bmatrix} J_{|l|}(\lambda_1 R_1) & Y_{|l|}(\lambda_1 R_1) & -I_{|l|}(\lambda_2 R_1) & 0 \\ (\lambda_1/m_1^*) J'_{|l|}(\lambda_1 R_1) & (\lambda_1/m_1^*) Y'_{|l|}(\lambda_1 R_1) & -(\lambda_2/m_2^*) I'_{|l|}(\lambda_2 R_1) & 0 \\ J_{|l|}(\lambda_1 R_2) & Y_{|l|}(\lambda_1 R_2) & 0 & -K_{|l|}(\lambda_2 R_2) \\ (\lambda_1/m_1^*) J'_{|l|}(\lambda_1 R_2) & (\lambda_1/m_1^*) Y'_{|l|}(\lambda_1 R_2) & 0 & -(\lambda_2/m_2^*) K'_{|l|}(\lambda_2 R_2) \end{bmatrix} \tag{A.3}$$

## A.2 2D QD-in-Ring in the magnetic field

As shown in Fig. 6.9 in Chapter 6, the dimensions of a QD-in-Ring have large difference in the growth direction and the plane perpendicular to it. The adiabatic approximation can be applied to separate the motion in the strong confinement direction from other directions [153]. In the present section, we focus on the motion of the electron and hole in the plane perpendicular to the $z$ direction and apply a 2D QD-in-Ring model in the polar coordinates $(r, \theta)$ for this study. As shown in Fig. A.1, in the radial direction,

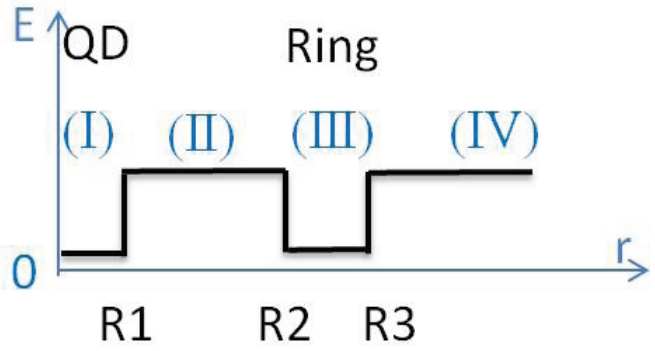


Figure A.1: Illustration of the confinement potential in a QD-in-Ring nanostructure with cylindrical symmetry in the radial direction.

the radius of QD, the inner and outer boundary of ring were denoted as $R_1$, $R_2$ and $R_3$, respectively.

Because we are interested in the electronic states near the band edge, effective mass approximation was applied in the present study. In the polar coordinate, the Hamiltonian of single particle state with the magnetic field ($B$) is:

$$H = -\frac{\hbar^2}{2m^*}\left[\frac{1}{r}\frac{\partial}{\partial r}(\frac{1}{r}\frac{\partial}{\partial r}) + \frac{1}{r^2}\frac{\partial^2}{\partial\theta^2} - \frac{iqB}{\hbar}\frac{\partial}{\partial\theta} - \frac{(qBr)^2}{4\hbar^2}\right] + V(r) \tag{A.4}$$

where $q = -e$ and $q = e$ for the charge of electrons and holes, respectively, and $e$ is the elementary charge. $B$ is the magnetic field. The symmetric gauge was applied to the vector potential in the present calculation, which leads to the components of $A_\theta = Br/2$ and $A_r = 0$ in the polar coordinate. $V(r)$ is the confinement potential energy which is equal to zero and the band offset for the regions in and out of QD-in-Ring, respectively. The mismatch of the effective mass between the QD-in-Ring ($m_1^*$) and the barrier layer ($m_2^*$) was considered. Due to the cylindrical symmetry, the $z$-projection of the single particle angular momentum is a good quantum number. With the angular quantum number $l_{e(h)}$ and radial quantum number $n_{e(h)}$, the single particle wave function was assumed as $\phi_{nl} = e^{il\theta} f_{nl}(r)/\sqrt{2\pi}$, where $f_{nl}(r)$ is the wave function component in the radial direction.

By replacing $r$ with $x = kr^2 = \frac{qBr^2}{2\hbar}$ and substitute the single particle wave function into Eq.(A.4), the Schrödinger equation can be expressed as [145]

$$\left\{x\frac{\partial^2}{\partial x^2} + \frac{\partial}{\partial x} - \frac{l^2}{4x} - \frac{x}{4} + \beta\right\} f_{nl}(x) = 0, \tag{A.5}$$

where

$$\beta = -\frac{qBl}{4k\hbar} - \frac{m^*(V-E)}{2k\hbar^2} \tag{A.6}$$

Following the method in Landau's book [145], as $x \to \infty$ the required function behaves as $e^{-\frac{x}{2}}$, and for $x \to 0$ as $x^{\frac{|l|}{2}}$. The radial component of the wave function can be

express as

$$f_{nl}(x) = x^{\frac{|l|}{2}} e^{-\frac{x}{2}} u(x) \tag{A.7}$$

Substitue Eq.(A.7) into Eq.(A.5), the Schrödinger equation became a confluent hypergeometric differential equation with the solution [157]

$$f_{nl}(x) = \begin{cases} x^{\frac{|l|}{2}} e^{-\frac{x}{2}} C_1 M(a_1, b, x) & r \leq R_1 \\ x^{\frac{|l|}{2}} e^{-\frac{x}{2}} [C_2 M(a_2, b, x) + C_3 U(a_2, b, x) & R_1 < r < R_2 \\ x^{\frac{|l|}{2}} e^{-\frac{x}{2}} [C_4 M(a_1, b, x) + C_5 U(a_1, b, x) & R_2 \leq r \leq R_3 \\ x^{\frac{|l|}{2}} e^{-\frac{x}{2}} C_6 U(a_2, b, x) & R_3 < r \end{cases}$$

where $C_n (n = 1 \sim 6)$ are the normalization coefficients. $M(a, b, x)$ and $U(a, b, x)$ are the confluent hypergeometric function of the first and second kind. $a_{1,2} = -\beta + \frac{|l|}{2} + \frac{1}{2}$ for different effective mass $m_1^*$ and $m_2^*$ of QD-in-Ring and barrier layer, respectively. $b = |l|+1$, $x = \frac{qBr^2}{2\hbar}$.

By using the continuous boundary condition of the wave function at $R_1$, $R_2$ and $R_3$ as well as the normalization condition, the eigen energy and wave function of single particle states can be solved.

$$\begin{array}{ll} f_{nl}^{I}(R_1) = f_{nl}^{II}(R_1), & f_{nl}^{'I}(R_1)/m_1^* = f_{nl}^{'II}(R_1)/m_2^*, \\ f_{nl}^{II}(R_2) = f_{nl}^{III}(R_2), & f_{nl}^{'II}(R_2)/m_2^* = f_{nl}^{'III}(R_2)/m_1^*, \\ f_{nl}^{III}(R_3) = f_{nl}^{IV}(R_3), & f_{nl}^{'III}(R_3)/m_1^* = f_{nl}^{'IV}(R_3)/m_2^* \end{array}$$

In the following equations, if the confluent hypergeometric functions are denoted as

$$\begin{array}{c} M(a_{1(2)}, b, x) = M_{a_{1(2)}}(r^2) \\ U(a_{1(2)}, b, x) = U_{a_{1(2)}}(r^2) \end{array} \tag{A.8}$$

and

$$\begin{array}{c} P_1(a_{1(2)}, r) = (\frac{|l|}{2kr^2} - \frac{1}{2}) M_{a_{1(2)}}(r^2) + 2kr M'_{a_{1(2)}}(r^2) \\ P_2(a_{1(2)}, r) = (\frac{|l|}{2kr^2} - \frac{1}{2}) U_{a_{1(2)}}(r^2) + 2kr U'_{a_{1(2)}}(r^2) \end{array} \tag{A.9}$$

are defined for the first derivative of radial wave functions, the eigen energy and wave function of the single particle states can be numerically derived by solving a secular equation $|G| = 0$. The definition of $G$ is in the following equation:

$$G = \begin{bmatrix} M_{a_1}(R_1^2) & -M_{a_2}(R_1^2) & -U_{a_2}(R_1^2) & 0 & 0 & 0 \\ \frac{m_2^*}{m_1^*} P_1(a_1, R_1) & -P_1(a_2, R_1) & -P_2(a_2, R_1) & 0 & 0 & 0 \\ 0 & M_{a_2}(R_2^2) & U_{a_2}(R_2^2) & -M_{a_1}(R_2^2) & -U_{a_1}(R_1^2) & 0 \\ 0 & \frac{m_1^*}{m_2^*} P_1(a_2, R_2) & \frac{m_1^*}{m_2^*} P_2(a_2, R_2) & -P_1(a_1, R_2) & -P_2(a_1, R_2) & 0 \\ 0 & 0 & 0 & M_{a_1}(R_3^2) & U_{a_1}(R_3^2) & -U_{a_2}(R_3^2) \\ 0 & 0 & 0 & \frac{m_2^*}{m_1^*} P_1(a_1, R_3) & \frac{m_2^*}{m_1^*} P_2(a_1, R_3) & -P_2(a_2, R_3) \end{bmatrix} \tag{A.10}$$

In Fig. A.2, the electron energy as a function of the magnetic field is shown, which

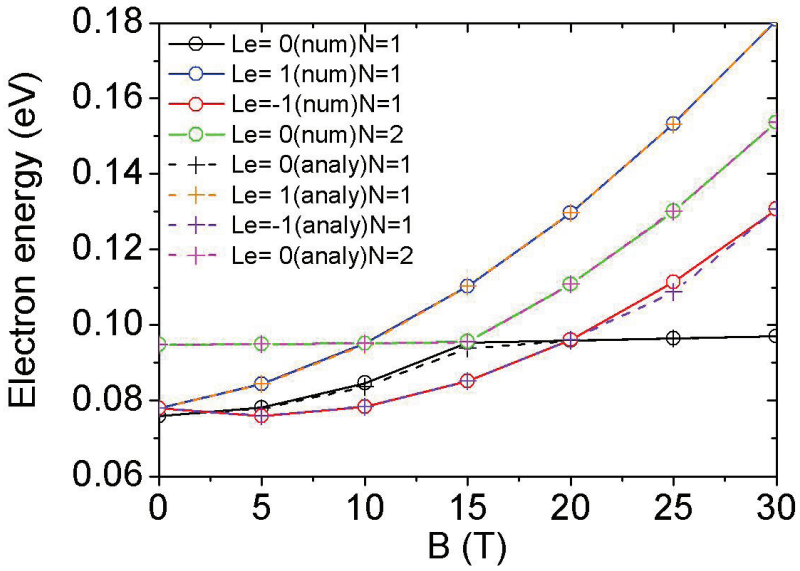


Figure A.2: Comparison of the numerical calculation results of electron energy in a QD-in-Ring nanostructure for different angular momentum $l_e$ and radial quantum number $n$.

is calculated with the above semi-analytical method for a QD-in-Ring with the QD radius $R_1$= 4 nm, ring width $W = R_3 - R_2 = 5$ nm and ring radius $R_r = (R_2 + R_3)/2 = 16.5$ nm (the barrier width between QD and ring and out of the ring are assumed to be 10 nm and 15 nm, respectively). The comparison between the semi-analytical results and the numerical results of a finite element method calculation showed a good agreement. When $B = 15$ T, the lowest electron state with $l_e = 0$ has anti-crossing behavior with the second lowest electron state due to their same angular symmetry ($l_e = 0$). When $B = 0$, the lowest and the second lowest electron states are localized in the ring and QD part, respectively, which leads to the different response to the magnetic field. After the anti-crossing, the main feature of their wave function was exchanged and the lowest electron is in the QD part.

It is worthy to point out that the above equations can be easily modified for other nanostructures with cylindrical symmetry, for instance, quantum disk, concentric double quantum rings. The difference in their calculation is the number of the boundary conditions.

# Bibliography


[1] Schmid, G. *Nanoparticles–From Theory to Application*. WILEY-VCH Verlag GmbH & Co., (2004).

[2] Sattler, K. D. *Handbook of Nanophysics–Nanoparticles and Quantum Dots*. Taylor and Francis Group, LLC, (2011).

[3] Choi, C. L. and Alivisatos, A. P. *Annu. Rev. Phys. Chem.* **61**, 369–389 (2010).

[4] Kumar, S. and Nann, T. *Small* **2**, 316–329 (2006).

[5] Reiss, P., Protiere, M., and Li, L. *Small* **5**, 154–168 (2009).

[6] Lo, S. S., Mirkovic, T., Chuang, C., Burda, C., and Scholes, G. D. *Adv. Mater.* **23**, 180–197 (2011).

[7] Vasiliev, R. B., Dirin, D. N., and Gaskov, A. M. *Russian Chemical Review* **80**, 1139–1158 (2011).

[8] Masumoto, Y. and Takagahara, T. *Semiconductor quantum dots*. Springer-Verlag Berlin Heidelberg, (2002).

[9] Barnham, K. and Vvedensky, D. *Low-dimensional semiconductor structures: Fundamentals and Device applications*. Cambridge University Press, (2001).

[10] Sanguinetti, S., Mano, T., and Kuroda, T. *NanoScience and Technology* **87**, 161–196 (2014).

[11] Sun, B., Marx, E., and Greenham, N. C. *Nano Lett.* **3**, 961–963 (2003).

[12] Zhou, Y., Li, Y., Zhong, H., Hou, J., Ding, Y., Yang, C., and Li, Y. *Nanotechnology* **17**, 4041–4047 (2006).

[13] Wang, L., Liu, Y., Jiang, X., Qin, D., and Cao, Y. *J. Phys. Chem. C* **111**, 9538–9542 (2007).

[14] Tan, Z., Zhang, F., Zhu, T., Xu, J., Wang, A. Y., Dixon, J. D., Li, L., Zhang, Q., Mohney, S. E., and Ruzyllo, J. *Nano Lett.* **7**, 3803–3807 (2007).

[15] Anikeeva, P. O., Halpert, J. E., Bawendi, M. G., and Bulovic, V. *Nano Lett.* **9**, 2532–2536 (2009).

[16] Parak, W. J., Pellegrino, T., and Plank, C. *Nanotechnology* **16**, R9–R25 (2005).

[17] Pellegrino, T., Kudera, S., Liedl, T., Javier, A. M., Manna, L., and Parak, W. J. *small* **1**, 48–63 (2005).

[18] Suresh, S. *Nanoscience and Nanotechnology* **3**, 62–74 (2013).

[19] Peyghambarian, N., Koch, S. W., and Mysyrowicz, A. *Introduction to semiconductor optics*. Prentice-Hall, Inc., (1993).

[20] Haug, H. and Koch, S. W. *Quantum theory of the optical and electronic properties of semiconductors*. World Scientific Publishing Co. Pte. Ltd, (2005).

[21] Peng, X., Manna, L., Yang, W., Wickham, J., Scher, E., Kadavanich, A., and Alivisatos, A. P. *Nature* **404**, 59–61 (2000).

[22] Schlenskaya, N. N., Yao, Y., Mano, T., Kuroda, T., Garshev, A. V., Kozlovskii, V. F., Gaskov, A. M., Vasiliev, R. B., and Sakoda, K. *Chem. Mater.* **29**, 579 (2017).

[23] Vasiliev, R. B., Lebedev, A. I., Lazareva, E. P., Shlenskaya, N. N., Zaytsev, V. B., Vitukhnovsky, A. G., Yao, Y., and Sakoda, K. *Phys. Rev. B* **95**, 165414 (2017).

[24] Manna, L., Scher, E. C., and Alivisatos, A. P. *J. Am. Chem. Soc.* **122**, 12700–12706 (2000).

[25] Manna, L., Milliron, D. J., Meisel, A., Scher, E. C., and Alivisatos, A. P. *Nature Mat.* **2**, 382–385 (2003).

[26] Cheong, S., Watt, J., Ingham, B., Toney, M. F., and Tilley, R. D. *J. Am. Chem. Soc.* **131**, 14590–14595 (2009).

[27] Conca, E., Aresti, M., Saba, M., Casula, M. F., Quochi, F., Mula, G., Loche, D., Kim, M. R., Manna, L., Corrias, A., Murab, A., and Bongiovannib, G. *Nanoscale* **6**, 2238–2243 (2014).

[28] Fiore, A., Mastria, R., Lupo, M. G., Lanzani, G., Giannini, C., Carlino, E., Morello, G., Giorgi, M. D., Li, Y., Cingolani, R., , and Manna, L. *J. Am. Chem. Soc.* **131**, 2274–2282 (2009).

[29] Pang, Q., Zhao, L., Cai, Y., Nguyen, D. P., Regnault, N., Wang, N., Yang, S., Ge, W., Ferreira, R., Bastard, G., and Wang, J. *Chem. Mater.* **17**, 5263–5267 (2005).

[30] Asokan, S., Krueger, K. M., Colvin, V. L., and Wong, M. S. *Small* **3**, 1164–1169 (2007).

[31] Ko, W. Y., Bagaria, H. G., Asokan, S., Lin, K., and Wong, M. S. *J. Mater. Chem.* **20**, 2474–2478 (2010).

[32] Yong, K., Sahoo, Y., Swihart, M. T., and Prasad, P. N. *J. Phys. Chem. C* **111**, 2447–2458 (2007).

[33] Giorgi, M. D., Tari, D., Manna, L., Krahne, R., and Cingolani, R. *Microelectronics Journal* **36**, 552–554 (2005).

[34] Tari, D., Giorgi, M. D., Sala, F. D., Carbone, L., Krahne, R., Manna, L., Cingolani, R., Kudera, S., and Parak, W. J. *Appl. Phys. Lett.* **87**, 224101 (2005).

[35] Malkmus, S., Kudera, S., Manna, L., Parak, W. J., and Braun, M. *J. Phys. Chem. B* **110**, 17334–17338 (2006).

[36] Tari, D., Giorgi, M. D., Pompa, P. P., Carbone, L., Manna, L., Kudera, S., and Cingolani, R. *Appl. Phys. Lett.* **89**, 094104 (2006).

[37] Morello, G., Tari, D., Carbone, L., Manna, L., Cingolani, R., and Giorgi, M. D. *Appl. Phys. Lett.* **92**, 191905 (2008).

[38] Goodman, M. D., Zhao, L., DeRocher, K. A., Wang, J., Mallapragada, S. K., and Lin, Z. *ACS Nano* **4**, 2043–2050 (2010).

[39] Vasiliev, R. B., Dirin, D. N., and Gaskov, A. M. *Mendeleev Commun.* **19**, 126–127 (2009).

[40] Cho, J. W., Kim, H. S., Kim, Y. J., Jang, S. Y., Park, J., Kim, J., Kim, Y., and Cha, E. H. *Chem. Mater.* **20**, 5600–5609 (2008).

[41] Jiang, F., Li, Y., Ye, M., Fan, L., Ding, Y., and Li, Y. *Chem. Mater.* **22**, 4632–4641 (2010).

[42] Shen, H., Niu, J., Wang, H., Li, X., Li, L., and Chen, X. *Dalton Trans.* **39**, 11432–11438 (2010).

[43] Cui, Y., Banin, U., Bjork, M. T., and Alivisatos, A. P. *Nano Lett.* **5**, 1519–1523 (2005).

[44] Gur, I., Fromer, N. A., and Alivisatos, A. P. *J. Phys. Chem. B* **110**, 25543–25546 (2006).

[45] Li, Y., Mastria, R., Li, K., Fiore, A., Wang, Y., Cingolani, R., Manna, L., and Gigli, G. *Appl. Phys. Lett.* **95**, 043101 (2009).

[46] Li, Y., Mastria, R., Fiore, A., Nobile, C., Yin, L., Biasiucci, M., Cheng, G., Cucolo, A. M., Cingolani, R., Manna, L., and Gigli, G. *Adv. Mater.* **21**, 4461–4466 (2009).

[47] Li, J. and Wang, L.-W. *Nano Lett.* **3**, 1357–1363 (2003).

[48] Milliron, D. J., Hughes, S. M., Cui, Y., Manna, L., Li, J., Wang, L.-W., and Alivisatos, A. P. *Nature* **430**, 190–195 (2004).

[49] Lutich, A. A., Mauser, C., Como, E. D., Huang, J., Vaneski, A., Talapin, D. V., Rogach, A. L., and Feldmann, J. *Nano Lett.* **10**, 4646–4650 (2010).

[50] Mauser, C., Limmer, T., Como, E. D., Becker, K., Rogach, A. L., Feldmann, J., and Talapin, D. V. *Phys. Rev. B* **77**, 153303 (2008).

[51] Mauser, C., Como, E. D., Baldauf, J., Rogach, A. L., Huang, J., Talapin, D. V., and Feldmann, J. *Phys. Rev. B* **82**, 081306 (2010).

[52] Wang, L.-W. *J. Phys. Chem. B* **109**, 23330–23335 (2005).

[53] Sakoda, K., Yao, Y., Kuroda, T., Dirin, D. N., and Vasiliev, R. B. *Opt. Mater. Express* **1**, 379–390 (2011).

[54] Yao, Y., Kuroda, T., Dirin, D., Irkhina, A., Vasiliev, R., and Sakoda, K. *Opt. Mater. Express* **3**, 977 (2013).

[55] Ivanov, S. A., Piryatinski, A., Nanda, J., Tretiak, S., Zavadil, K. R., Wallance, W. O., Werder, D., and Klimov, V. I. *J. Am. Chem. Soc.* **129**, 11708 (2007).

[56] Boxberg, F., Sondergaard, N., and Xu, H. Q. *Nano Lett.* **10**, 1108–1112 (2010).

[57] Vasiliev, R. B., Dirin, D. N., Sokolikova, M. S., Dorofeev, S. G., Vitukhnovsky, A. G., and Gaskov, A. M. *Mendeleev Commun.* **19**, 128–130 (2009).

[58] Smith, A. M., Mohs, A. M., and Nie, S. *Nature Nanotechnology* **4**, 56–63 (2009).

[59] Fomin, V. M. *Physics of Quantum Rings*. Springer-Verlag Berlin Heidelberg, (2014).

[60] Bayer, M., Korkusinski, M., Hawrylak, P., Gutbrod, T., Michel, M., and Forchel, A. *Phys. Rev. Lett.* **90**, 186801 (2003).

[61] Koguchi, N., Takahashi, S., and Chikyow, T. *J. Cryst. Growth* **111**, 688–692 (1991).

[62] Mano, T., Kuroda, T., Kuroda, K., and Sakoda, K. *J. Nanophoto.* **3**, 031605 (2009).

[63] Mano, T., Kuroda, T., Sanguinetti, S., Ochiai, T., Tateno, T., Kim, J., Noda, T., Kawabe, M., Sakoda, K., Kido, G., and Koguchi, N. *Nano Lett.* **5**, 425–428 (2005).

[64] Kuroda, T., Mano, T., Ochiai, T., Sanguinetti, S., Sakoda, K., Kido, G., and Koguchi, N. *Phys. Rev. B* **72**, 205301 (2005).

[65] Somaschini, C., Bietti, S., Koguchi, N., and Sanguinetti, S. *Nanotechnology* **22**, 185602 (2011).

[66] Viefers, S., Koskinen, P., Deo, P. S., and Manninen, M. *Physica E* **21**, 1–35 (2004).

[67] Lorke, A., Luyken, R. J., Govorov, A. O., Kotthaus, J. P., Garcia, J. M., and Petroff, P. M. *Phys. Rev. Lett.* **84**, 2223–2226 (2000).

[68] Romer, R. A. and Raikh, M. *Phys. Rev. B* **62**, 7045–7049 (2000).

[69] Govorov, A. O., Ulloa, S. E., Karrai, K., and Warburton, R. J. *Phys. Rev. B* **66**, 801309 (2002).

[70] Li, B. and Peeters, F. M. *Phys. Rev. B* **83**, 115448 (2011).

[71] Ding, F., Akopian, N., Li, B., Perinetti, U., Govorov, A., Peeters, F. M., Bufon, C. C. B., Deneke, C., Chen, Y. H., Rastelli, A., Schmidt, O., and Zwiller, V. *Phys. Rev. B* **82**, 075309 (2010).

[72] Elborg, M., Noda, T., Kuroda, T., Yao, Y., and Sakuma, Y. *19th International Conference on Molecular Beam Epitaxy (MBE2016), 4th-9th September 2016, Montpellier, France* (2016).

[73] Climente, J. I., Planelles, J., Barranco, M., Malet, F., and Pi, M. *Phys. Rev. B* **73**, 235327 (2006).

[74] Planelles, J. and Climente, J. I. *Eur. Phys. J. B* **48**, 65–70 (2005).

[75] Culchac, F. J., Porras-Montenegro, N., and Latge, A. *J. Phys.: Condens. Matter* **20**, 285215 (2008).

[76] Szafran, B. and Peeters, F. M. *Phys. Rev. B* **72**, 155316 (2005).

[77] Aharonov, Y. and Bohm, D. *Phys. Rev.* **115**, 485–491 (1959).

[78] Kuroda, T., Belhadj, T., Mano, T., Urbaszek, B., Amand, T., Marie, X., Sanguinetti, S., Sakoda, K., and Koguchi, N. *Phys. Status Solidi B* **246**, 861–863 (2009).

[79] Akahane, Y., Asano, T., Song, B.-S., , and Noda, S. *Nature* **425**, 944–947 (2003).

[80] Akahane, Y., Asano, T., Song, B.-S., and Noda, S. *Opt. Express* **13**, 1202–1214 (2005).

[81] Purcell, E. M. *Phys. Rev.* **69**, 681–681 (1946).

[82] Hennessy, K., Badolato, A., Winger, M., Gerace, D., Atature, M., Gulde, S., Falt, S., Hu, E. L., and Imamoglu, A. *Nature* **445**, 896–899 (2007).

[83] Yamagiwa, M., Kuroda, T., Mano, T., Sakoda, K., and Koguchi, N. *in Extended Abstracts of the 68th Autumn Meeting of the Japan Society of Applied Physics (in Japanese)* **3**, 1415 (2007).

[84] Sakoda, K. *Optical properties of photonic crystals.* Springer-Verlag, Berlin, (2001).

[85] Huang, X., Lai, Y., Hang, Z. H., Zheng, H., and Chan, C. T. *Nature Mater.* **10**, 582 (2011).

[86] Caloz, C. and Itoh, T. *Electromagnetic Metamaterials: Transmission Line Theory and Microwave Applications.* Wiley, (2005).

[87] Mei, J., Wu, Y., Chan, C. T., and Zhang, Z.-Q. *Phys. Rev. B* **86**, 035141 (2012).

[88] Sakoda, K. *Opt. Express* **20**, 25181 (2012).

[89] Sakoda, K. *Phys. Rev. A* **90**, 013835 (2014).

[90] Silveirinha, M. and Engheta, N. *Phys. Rev. Lett.* **97**, 157403 (2006).

[91] Alu, A., Silveirinha, M. G., Salandrino, A., and Engheta, N. *Phys. Rev. B* **75**, 155410 (2007).

[92] Cardona, M. and Pollak, F. H. *Phys. Rev.* **142**, 530–543 (1966).

[93] Chuang, S. L. *Physics of optoelectronic devices.* John Wiley & Sons.Inc, (1995).

[94] Banyai, L. and Koch, S. W. *Semiconductor quantum dots.* World Scientific, (1993).

[95] Adachi, S. *Properties of group-IV, III-V and II-VI semiconductors.* Wiley, Chichester, (2005).

[96] Adachi, S. *Properties of semiconductor alloys-Group-IV, III-V and II-VI semiconductors.* John Wiley & sons Ltd., (2009).

[97] Sakurai, J. J. *Modern quantum mechanics.* Addison-Weslev Publishing Company, Inc., (1994).

[98] Scholes, G. D. and Rumbles, G. *Nature Mater.* **5**, 683–696 (2006).

[99] Bastard, G. *Wave mechanics applied to semiconductor heterostructures.* EDP Sciences, (1992).

[100] Bryant, G. W. *Phys. Rev. B* **37**, 8763–8772 (1988).

[101] Tyrrell, E. J. and Smith, J. M. *Phys. Rev. B* **84**, 165328 (2011).

[102] Wei, S.-H. and Zhang, S. B. *Phys. Rev. B* **62**, 6944–6947 (2000).

[103] Swank, R. K. *Phys. Rev.* **153**, 844–849 (1967).

[104] Ninomiya, S. and Adachi, S. *J. Appl. Phys.* **78**, 4681–4689 (1995).

[105] Dalven, R. *Phys. Status Solidi B* **48**, K23–K26 (1971).

[106] Wheeler, R. G. and Dimmock, J. O. *Phys. Rev.* **125**, 1805–1815 (1962).

[107] Cardona, M., Weinstein, M., and Wolff, G. A. *Phys. Rev.* **140**, A633–A637 (1965).

[108] Hopfield, J. J. and Thomas, D. G. *Phys. Rev.* **122**, 35–52 (1961).

[109] Long, F., Hagston, W. E., Harrison, P., and Stirner, T. *J. Appl. Phys.* **82**, 3414–3421 (1997).

[110] Bechstedt, F. and Enderlein, R. *Semiconductor Surface and Interfaces: Their Atomic and Electronic Structures.* Akademie-Verlag, Berlin, (1988).

[111] Cardona, M. *J. Appl. Phys.* **32**, 2151–2155 (1961).

[112] Marple, D. *J. Appl. Phys.* **35**, 1879–1882 (1964).

[113] Sondergeld, M. *Phys. Status Solidi B* **81**, 253–262 (1977).

[114] Passler, R., Griebl, E., Riepl, H., Lautner, G., Bauer, S., Preis, H., Gebhardt, W., Buda, B., As, D. J., Schikora, D., Lischka, K., Papagelis, K., and Ves, S. *J. Appl. Phys.* **86**, 4403–4411 (1999).

[115] Clerjaud, B., Gelineau, A., Galland, D., and Saminadayar, K. *Phys. Rev. B* **19**, 2056–2058 (1979).

[116] Aven, M. and Segall, B. *Phys. Rev.* **130**, 81–91 (1963).

[117] Inui, T., Tanabe, Y., and Onodera, Y. *Group theory and Its Applications in Physics.* Springer-Verlag, Berlin, (1990).

[118] Brus, L. E. *J. Chem. Phys.* **80**, 4403–4409 (1984).

[119] Peng, P., Milliron, D. J., Hughes, S. M., Johnson, J. C., Alivisatos, A. P., and Saykally, R. J. *Nano Lett.* **5**, 1809–1813 (2005).

[120] Talapin, D. V., Nelson, J. H., Shevchenko, E. V., Aloni, S., Sadtler, B., and Alivisatos, A. P. *Nano Lett.* **7**, 2951–2959 (2007).

[121] Choi, C. L., Koski, K. J., Sivasankar, S., and Alivisatos, A. P. *Nano Lett.* **9**, 3544–3549 (2009).

[122] Vitukhnovsky, A. G., Shul'ga, A. S., Ambrozevich, S. A., Khokhlov, E. M., Vasiliev, R. B., Dirin, D. N., and Yudson, V. I. *Phys. Lett. A* **373**, 2287–2290 (2009).

[123] Dirin, D. N., Vasiliev, R. B., Sokolikova, M. S., and Gaskov, A. M. *Inorg. Mater.* **47**, 23–28 (2011).

[124] Yao, Y., Kuroda, T., Dirin, D. N., Sokolikova, M. S., and Vasiliev, R. B. *Superlattices and Microstructures* **76**, 244 (2014).

[125] Povolotskyi, M. and Carlo, A. D. *J. Appl. Phys.* **100**, 063514 (2006).

[126] Stuckes, A. D. and Farrell, G. *J. Phys. Chem. Solids* **25**, 477–482 (1964).

[127] Madelung, O., Schulz, M., and Weiss, H. *Physics of II-VI and I-VII compounds, semimagnetic semiconductors, Landolt-Börnstein, Group III, vol.17b.* Springer-Verlag Berlin, Heidelberg, New York, (1982).

[128] Kuo, M. K., Lin, T. R., and Hong, K. B. *J. Appl. Phys.* **103**, 073705 (2008).

[129] de Walle, C. G. V. *Phys. Rev. B* **39**, 1871–1883 (1989).

[130] Park, S.-H. and Cho, Y.-H. *J. Appl. Phys.* **109**, 113103 (2011).

[131] Cai, X., Mirafzal, H., Nguyen, K., Leppert, V., and Kelley, D. F. *J. Phys. Chem. C* **116**, 8118–8127 (2012).

[132] Fairclough, S. M., Tyrrell, E. J., Graham, D. M., Lunt, P. J. B., Hardman, S. J. O., Pietzsch, A., Hennies, F., Moghal, J., Flavell, W. R., Watt, A. A. R., and Smith, J. M. *J. Phys. Chem. C* **116**, 26898–26907 (2012).

[133] Rivest, J. B., Swisher, S. L., Fong, L.-K., Zheng, H., and Alivisatos, A. P. *ACS Nano* **5**, 3811–3816 (2011).

[134] Yao, Y., Ochiai, T., Mano, T., Kuroda, T., Noda, T., Koguchi, N., and Sakoda, K. *Chin. Opt. Lett.* **7**, 882 (2009).

[135] Pavesi, L. and Guzzi, M. *J. Appl.Phys.* **75**, 4779–4842 (1994).

[136] Yamagiwa, M., Sumita, N., Minami, F., and Koguchi, N. *J. Lumin.* **108**, 379 (2004).

[137] Madelung, O., Schulz, M., and Weiss, H. *Physics of Group IV Elements and III-V Compounds, Landolt-Börnstein, Group III, vol.17a.* Springer-Verlag Berlin, Heidelberg, New York, (2002).

[138] Llorens, J. M., Trallero-Giner, C., Garcia-Cristobal, A., and Cantarero, A. *Phys. Rev. B* **64**, 035309 (2001).

[139] Garcia, J. M., Medeiros-Ribeiro, G., Schmidt, K., Ngo, T., and Petroff, P. M. *Appl. Phys. Lett.* **71**, 2014–2016 (1997).

[140] Elborg, M., Noda, T., Mano, T., Kuroda, T., Yao, Y., Sakuma, Y., and Sakoda, K. *J. Cryst. Growth* **477**, 239 (2017).

[141] Yao, Y., Elborg, M., Kuroda, T., and Sakoda, K. *J. Phys.: Condens Matter* **29**, 385301 (2017).

[142] Bosio, C., Staehli, J. L., Guzzi, M., Burri, G., and Logan, R. A. *Phys. Rev. B* **38**, 3263–3268 (1988).

[143] Hu, H., Zhu, J.-L., Li, D.-J., and Xiong, J.-J. *Phys. Rev. B* **63**, 195307 (2001).

[144] Song, J. and Ulloa, S. E. *Phys. Rev. B* **63**, 125302 (2001).

[145] Landau, L. D. and Lifshitz, E. M. *Quantum Mechanics (3rd Edition)*. Pergamon Press Ltd, (1977).

[146] Szafran, B., Peeters, F. M., and Bednarek, S. *Phys. Rev. B* **70**, 125310 (2004).

[147] Zipper, E., Kurpas, M., and Maska, M. M. *New Journal of Physics* **14**, 093029 (2012).

[148] Zeng, Z., Garoufalis, C. S., and Baskoutas, S. *Phys. Lett. A* **378**, 2713–2718 (2014).

[149] Correa, J. D., Mora-Ramos, M. E., and Duque, C. A. *Physica B* **472**, 25–33 (2015).

[150] Barseghyan, M. G. *Physica E* **69**, 219–223 (2015).

[151] Zhitenev, N. B., Brodsky, M., Ashoori, R. C., Pfeiffer, L. N., and West, K. W. *Science* **285**, 715–718 (1999).

[152] Yi, W., Narayanamurti, V., Lu, H., Scarpulla, M. A., and Gossard, A. C. *Phys. Rev. B* **81**, 235325 (2010).

[153] Porras, L. C. and Mikhailov, I. D. *Physica E* **53**, 41–47 (2013).

[154] Yu, P. Y. and Cardona, M. *Fundamentals of Semiconductors*. Springer-Verlag Berlin Heidelberg, (1999).

[155] Abbarchi, M., Kuroda, T., Mano, T., Sakoda, K., Mastrandrea, C. A., Vinattieri, A., Gurioli, M., and Tsuchiya, T. *Phys. Rev. B* **82**, 201301(R) (2010).

[156] Yao, Y. and Sakoda, K. *Journal of the Physical Society of Japan* **85**, 065002 (2016).

[157] Abramowitz, M. and Stegun, I. A. *Handbook of Mathematical Functions, Natl.Bur.Stand.Appl.Math.Ser.No.55*. U.S. GPO, Washington, D.C., (1970).

# Publications

**Papers published in journals (first author)**

(1) Y. Yao, T. Ochiai, T. Mano, T. Kuroda, T. Noda, N. Koguchi, K. Sakoda
Electronic structure of GaAs/AlGaAs quantum double rings in lateral electric field
Chinese Optics Letters **7**, 1-4 (2009).

(2) Y. Yao, T. Kuroda, D.N. Dirin, A. A. Irkhina, R.B. Vasiliev, K. Sakoda
Exciton states of II-VI tetrapod-shaped nanocrystals
Optical Materials Express **3**, 977-988 (2013).

(3) Y. Yao, T. Kuroda, D.N. Dirin, M.S. Sokolikova, R.B.Vasiliev
Strain effects on optical properties of tetrapod-shaped CdTe/CdS core-shell nanocrystals
Superlattices and Microstructures **76**, 244-252 (2014).

(4) Y. Yao, K. Sakoda
Dirac cones in periodically modulated quantum wells
Journal of the Physical Society of Japan **85**, 065002 (2016).

(5) Y. Yao, M. Elborg, T. Kuroda, K. Sakoda
Excitonic Aharonov-Bohm effect in QD-on-Ring nanostructures
Journal of Physics.: Condensed Matter **29**, 385301, (2017).

**Papers published in journals (co-author)**

(1) K. Sakoda, Y. Yao, T. Kuroda, D.N. Dirin, R.B. Vasiliev
Exciton states of CdTe tetrapod-shaped nanocrystals
Optical Materials Express **1**, 379-390 (2011).

(2) K. Kumagai, Y. Yao, J. Chen, T. Sekiguchi
Image instability during the electrical measurement in SEM
Phys. Status Solidi C **8**, 1407-1411 (2011).

(3) B. Chen, J. Chen, Y. Yao, T. Sekiguchi, H. Matsuhata, H. Okumura

In situ monitoring of stacking fault formation and its carrier lifetime mediation in p-type 4H-SiC

Applied Physics Letter **105**, 042104 (2014).

(4) N. N. Schlenskaya, Y. Yao, T. Mano, T. Kuroda, A.V. Garshev, V.F. Kozlovskii, A.M. Gaskov, R.B. Vasiliev, K. Sakoda,

Scroll-like alloyed CdSxSe(1-x) Nanoplatelets: Facile synthesis and detailed analysis of tunable optical properties.

Chemistry of Materials **29**, 579-586 (2017).

(5) R. B. Vasiliev, A. I. Lebedev, E. P. Lazareva, N. N. Shlenskaya, V. B. Zaytsev, A. G. Vitukhnovsky, Y. Yao, K. Sakoda

High-energy exciton transitions in quasi-2D cadmium chalcogenide nanoplatelets.

Physical Review B **95**, 165414 (2017).

(6) M. Elborg, T. Noda, T. Mano, T. Kuroda, Y. Yao, Y. Sakuma, K. Sakoda

Self-assembly of vertically aligned quantum ring-dot structure by multiple droplet epitaxy

Journal of Crystal Growth, **477**, 239-242 (2017).

(7) M. Elborg, Y. Yao, T. Noda, T. Mano, Y. Sakuma, R. Bekarevich, K. Mitsuishi

Carrier transfer in closely stacked GaAs/AlGaAs quantum dots grown by using droplet epitaxy

Journal of the Korean Physical Society, accepted to be published (2018).

(8) R. B. Vasiliev, E. P. Lazareva, D. A. Karlova, A. V. Garshev, Y. Yao, T. Kuroda, A. M. Gaskov, K. Sakoda

Spontaneous folding of CdTe nanosheets induced by ligand exchange

Chemistry of Materials, accepted to be published (2018).

# Acknowledgements

First of all, I would like to express my deepest gratitude to my supervisor, Prof. Kazuaki Sakoda, who guide me through the interesting areas of nanoscale physics. His advices and knowledge, which he unselfishly shared, have been invaluable. I also thank him for having faith and patience in me. Above all, I appreciate his personality charm, and feel lucky for having the opportunity to work with him.

I would like to acknowledge thesis committee members: Prof. Takashi Sekiguchi, Prof. Xiao Hu from NIMS, and Prof. Shintaro Nomura, Prof. Michio Ikezawa from University of Tsukuba. Thank you for making time in your tight schedule and providing valuable comments to my study.

I am also grateful to Dr. T. Kuroda, Dr. T. Ochiai, Dr. T. Mano, Dr. T. Kawazu, Dr. J. Inoue and all the members of Nanophotonics Group and Epitaxial Nanostructures Group for their continuing support and encouragement during my study in NIMS.

I am also thankful to Dr. H. Zhou, Dr. M. Elborg, and Dr. M. Lozac'h for the fruitful discussion helped me to find new view and ideas for the research.

I take this opportunity to thank Ms. K. Hirosawa, Ms. M. Kamisaka, Ms. K. Higuchi, Ms. H. Koyama, and Ms. K. Tomura for their countless help in both my Ph.D. study and my life in Japan.

My special thanks to Prof. R. Vasiliev in the Moscow State University and the excellent students in his group for valuable discussions of our cooperative research and their hospitality during my visits to Moscow.

I owe my deepest gratitude to my parents and my cousin Dr. Y. Yao for their constant support and encouragement during my studies. Finally, I thank my wife Wei and my daughter Molin who are always standing by me and supporting me throughout my life. The thesis is dedicated to my family.

Yuanzhao Yao

March 2018